Chapter 7
Advanced Electron Microscopy Techniques Toward the Understanding of Metal Nanoparticles and Clusters

Francis Leonard Deepak, E. A. Anumol, and Junjie Li

7.1 Introduction

Nanoparticles (NPs) or clusters of the transition metals containing from a few tens to several thousand metal atoms have their sizes between the order of one nanometer to several tens or hundreds of nanometers [1]. They are usually stabilized by ligands, surfactants, polymers, or dendrimers protecting their surfaces. One of the earliest applications of metal nanoparticles was in catalysis, pioneered by Turkevich, wherein transition metal NPs were used in a variety of catalytic reactions including hydrogenation, hydrosilylation, and hydration of unsaturated organic substrates and redox reactions including water photosplitting and photocatalytic hydrogenation [2]. Haruta's studies on oxide-supported AuNP-catalyzed CO oxidation by O_2 at low temperatures were a real breakthrough, showing that it was the oxide-supported AuNPs that were active and that the nm size was crucial [3–8]. Apart from catalysis, metal nanoparticles have found important applications, mainly for their plasmon enhancement effects [9]. Gold nanoparticles with varied morphologies including spheres, cubes, and stars, for example, show promising optical properties for many applications, including those in the biomedical field (Fig. 7.1) [10, 11]. Apart from monometallic nanoparticles, it is also possible to fabricate bimetallic systems by a combination of two metals [12–14]. When two metals combine to form a nanoparticle, either the particle forms strictly what can be thought of as an alloy (ordered or random) or it could form a core-shell structure or Janus particle (Fig. 7.2) [15]. In the former case, the two atomic species are distributed homogeneously

F.L. Deepak (✉)
INL International Iberian Nanotechnology Laboratory, Braga 4715–330, Portugal
e-mail: leonard.francis@inl.int

E.A. Anumol • J. Li
Department of Advanced Electron Microscopy, Imaging and Spectroscopy, International Iberian Nanotechnology Laboratory, Avenida Mestre Jose Veiga, Braga 4715–330, Portugal

F.L. Deepak (ed.), *Metal Nanoparticles and Clusters*,
https://doi.org/10.1007/978-3-319-68053-8_7

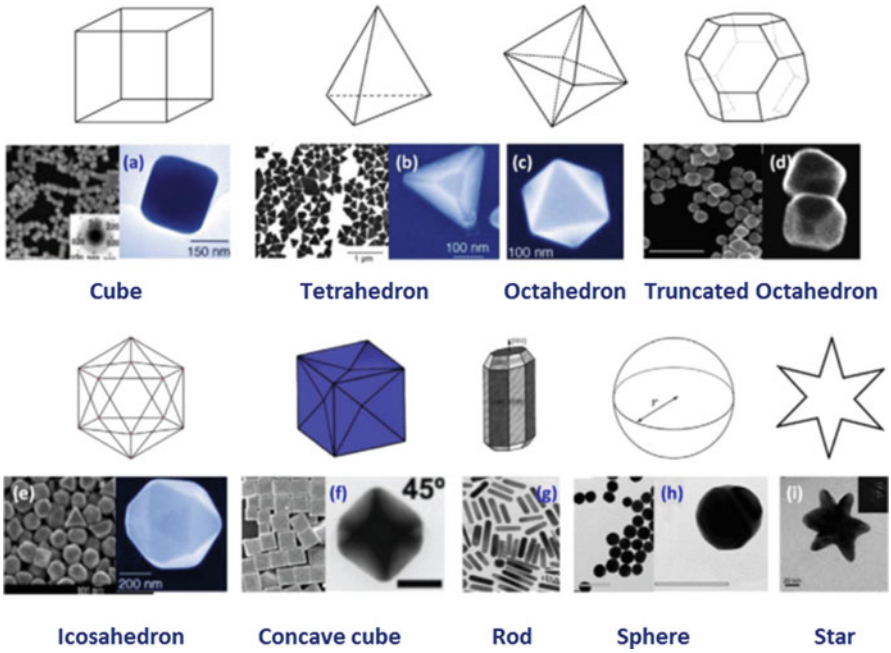

Fig. 7.1 Metal nanoparticles with different shapes, for example, Au: (**a**) cube, (**b**) tetrahedron, (**c**) octahedron, (**d**) truncated octahedron, (**e**) icosahedron, (**f**) concave cube, (**g**) rod, (**h**) sphere, and (**i**) star (Reprinted with permission from Zaleska-Medynska et al. [11]. Copyright 2016 Elsevier)

in the particle; in the latter, a heterogeneous particle is formed. In the case of a core-shell particle, a core of one of the metals is surrounded by a thin shell of the other metal forming a complex shape. Usually, the metal with larger size and lower surface energy will be on the outside layer, but the opposite may happen depending on the synthesis conditions. The core-shell structure is believed to be a very important factor affecting the electronic properties of the cluster/NP. A bimetallic particle could be more complex, for example, a nanoparticle might have an incomplete core or it may have a eutectic type of structure, where the two metals form separated particles joined in an interface as in the case of a Janus particle (Fig. 7.2c). Understanding how the spatial distribution of metals influences the fundamental properties of bimetallic colloids is critical. For bimetallic nanoparticles, the composition-controlled synthesis is especially significant due to their composition-dependent physical and chemical properties [13, 15]. More recently, multimetallic nanoparticles have been designed and explored for a variety of applications. The concept of multimetallic nanoparticle catalysts may not only help to reduce loadings of the precious metal like Pt but also allow the individual functional components to work synergistically to improve the catalytic performance (e.g., activity, durability, etc.), thus promising a much more flexible design of the electrocatalysts.

Rational design of metal nanoparticles based on atomic-scale understanding and their atomic-scale characterization is essential to tailor their applications. Advances

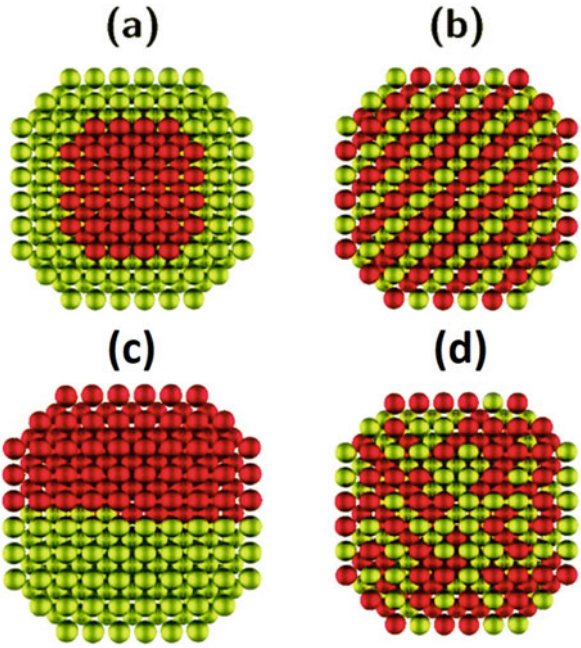

Fig. 7.2 Examples of different types of bimetallic nanoalloys: (**a**) core-shell, (**b**) ordered alloy, (**c**) Janus-like, and (**d**) random alloy (Reprinted with permission from F. Calvo [15]. Copyright 2015 Royal Society of Chemistry)

in synthesis and nanomaterial characterization enable providing better insights into the relationship between metal species in bimetallic/multimetallic nanoparticle systems and their varied properties.

A fundamental understanding of the structure of the nanoparticles and/or nanoparticles on support (of different compositions) and the way they influence properties and applications is essential. Electron microscopy techniques, especially transmission electron microscopy (TEM) can provide a complete understanding of the shape, morphology, atomic structure, chemical composition, etc. Along with improved theoretical models and simulations, it is possible to obtain the complete picture of the nanoparticle/alloy in order to establish structure-property relationships, which guide specific tailor-made applications. One important aspect of reduced dimensionality is the following: as particle dimensions reduce toward the nanoscale, the surface-to-volume ratio proportionally increases, and surface effects associated with nanoparticles become more pronounced. Understanding the nanoscale topography of surface sites, such as terraces, steps, kinks, adatoms, and vacancies, and their effects on catalytic and other physicochemical properties is the key factor, information which can be readily obtained employing TEM-based techniques [16]. More recently with advances in TEM-based techniques, including aberration-corrected S/TEM in combination with high-resolution spectroscopy, it is now possible to provide the complete characterization of complex metal nanoparticles paving the way for smart design [17]. The use of electron microscopy techniques in solving problems and addressing solutions lies at the heart of many

current and future technologies including those for sustainable energy in areas such as clean fuel production, CO_2 capture, solar cells and solar fuels, energy conversion and storage materials, hydrogen storage materials, and fuel cells [18].

In this chapter, an introduction to transmission electron microscopy imaging, diffraction, and spectroscopy is provided. The use of aberration-corrected TEM/STEM techniques in the systematic and atomic structure characterization of nanoalloys and nanoclusters is highlighted with several recent examples. Special techniques including 3D tomography, spectroscopic tomography, in situ techniques, etc. which are now readily possible due to advances in hardware, detectors, and special holders are addressed. Several recent examples of elucidation of the structure of metal nanoparticles and clusters by these advances in electron microscopy techniques are also specifically illustrated.

7.2 Characterization Techniques

Transmission electron microscopy has been widely used as a powerful tool to directly observe the structure of nanoparticles with atomic resolution. It can provide highly localized real-space imaging of objects with potential atomic resolution. Especially for the new generation of aberration-corrected (AC) electron microscopes, the spatial resolution has been attained at the sub-angstrom scale [19–21]. The development of AC technology enables new opportunities for atomic-scale imaging of nanostructures, such as alloy nanoparticles [22–25], ultra-small clusters [26, 27], segregated atoms at grain boundary [28, 29], and doped atoms in materials [30–33], as well as to monitor single atom behavior on supports [34]. In most of modern transmission electron microscopes, two high-resolution imaging modes are usually used: high-resolution transmission electron microscopy and high-resolution scanning transmission electron microscopy. In addition, spectroscopic techniques are present, such as energy-dispersive X-ray analysis and electron energy loss spectroscopy, which transforms the transmission electron microscope into an analytical electron microscope, a powerful tool to identify the atomic, chemical, and electronic structures [35].

7.2.1 Transmission Electron Microscopy (TEM)

Since the first TEM that was built by Max Knoll and Ernst Ruska in 1931, TEM has been widely used in a wide variety of fields ranging from materials science to biology [36]. The historical development of electron microscopy has experienced three stages: transmission electron microscopy, high-resolution electron microscopy (HREM), and high-spatial-resolution analytical electron microscopy. Throughout this process, resolution has been an important technical index which has led to the development of high-resolution electron microscopy. Accompanied with the development of the aberration corrector, it is possible to tune the aberrations

of electron lens [37]. In 1998, a hexapole corrector system was constructed for compensation of the spherical aberration of the objective lens of a transmission electron microscope by Max Haider et al. [38]. Subsequent to implementing this, the spherical aberration corrector system in a commercial 200 kV TEM with a field emission gun demonstrated an improvement of the point resolution from 2.4 Å to better than 1.4 Å [38]. To date, the resolution of aberration-corrected TEM has been enhanced up to ~0.6 Å at 300 kV [39].

Figure 7.3 shows a sectional schematic diagram of a typical TEM. It can be divided into three parts: the illumination system, the objective lens/stage, and the imaging system. The illumination system comprises the gun and the condenser

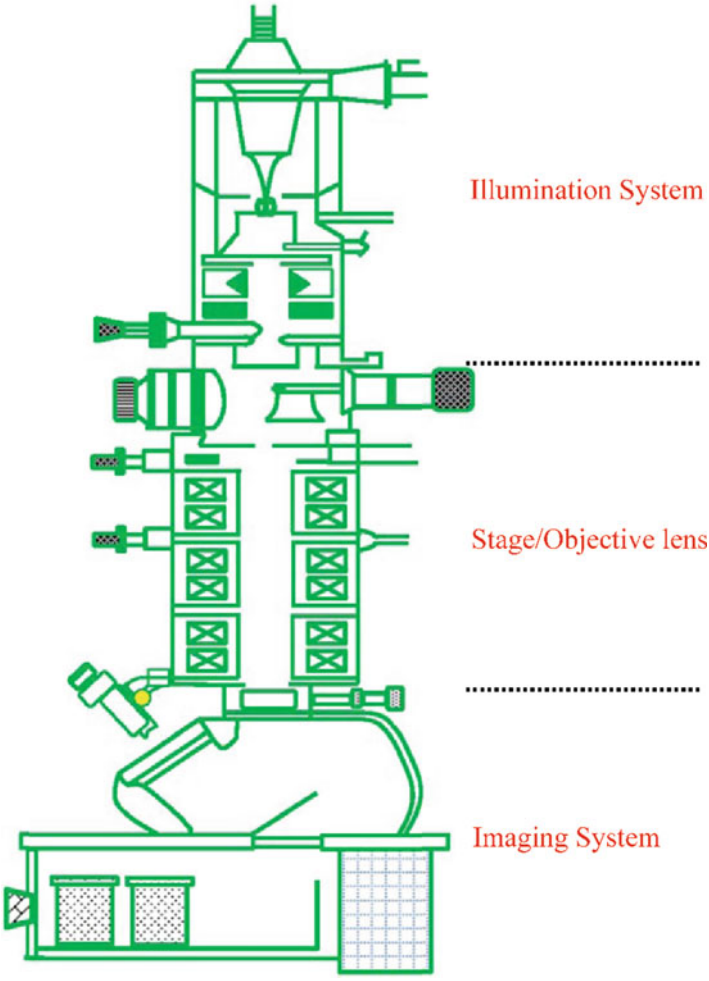

Fig. 7.3 A sectional schematic diagram of a typical TEM. It can be divided into three parts: the illumination system, the objective lens/stage, and the imaging system

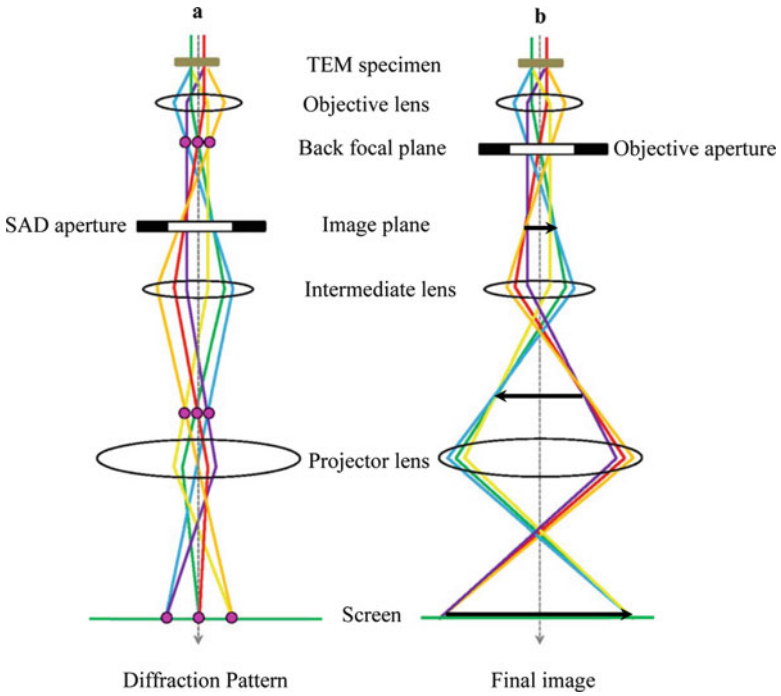

Fig. 7.4 Simplified schematic diagram showing the two basic operations of the TEM: (**a**) diffraction mode (the intermediate lens select the back focal plane of the objective lens as its object) and (**b**) imaging mode (the intermediate lens select the image plane of the objective lens as its object)

lenses, and its role is to take the electrons from the source and transfer them onto the thin TEM sample. The illumination system can be operated in two principal modes: parallel beam and convergent beam. The parallel beam is used mainly for selected area diffraction and TEM imaging, while the convergent beam is used primarily for convergent beam electron diffraction (CBED) and scanning TEM (STEM) imaging [40, 41]. The objective lens and the specimen stage system are the heart of the TEM, wherein all the electron-specimen interactions take place and the two fundamental TEM operations occur to form diffraction patterns and images that are subsequently magnified for viewing and recording, as shown in Fig. 7.4. In each case the intermediate lens selects either the back focal plane (diffraction mode) or the image plane (image mode) of the objective lens as its object, and the diffraction patterns or images are obtained, respectively. The imaging system uses several lenses to magnify the diffraction patterns and images produced by the objective lens and to focus it on a fluorescent screen, photographic film, or a CCD camera detector [35].

7.2.1.1 Diffraction

Diffraction is an interaction between a wave of any kind and an object of any kind. In the TEM, the electrons are utilized to go through a thin specimen and scattered mainly in the forward direction to form diffraction patterns on the fluorescent screen or CCD camera. In this way different diffraction modes can be realized in TEM, such as selected area electron diffraction (SAED), convergent beam electron diffraction (CBED), and nanobeam electron diffraction (NBED) [42].

Selected Area Electron Diffraction

Most of the forward-scattering signals can be used to form a selected area diffraction pattern in screen or CCD by using a selected area aperture in the TEM. SAED is the classic way to identify the crystallographic information of the specimen. Based on the selected area diffraction pattern (SADP) obtained in the TEM, we can identify the crystalline nature (single crystal, polycrystalline, amorphous) of the specimen (Fig. 7.5) [43].

However, it is worthy to note that there are two severe limitations when we try to use the SAED. One is that we have to be very cautious in interpreting SADPs from areas which are $< \sim$500 nm in diameter because the information in the pattern may not be limited to that region. For an intermediate-voltage high-resolution TEM with a very low spherical aberration, the region analyzed by SAED may be limited to $< \sim$100 nm in diameter, which is still too large for examining many nanosystems (smaller than 100 nm), such as nanoscale particles, defects in crystal, thin films, as well as second-phase precipitates which have an important influence on the properties of materials. Another limitation is that the SADPs contain only rather imprecise 2D crystallographic information because the Bragg conditions are relaxed for thin specimens and small grains within the specimen.

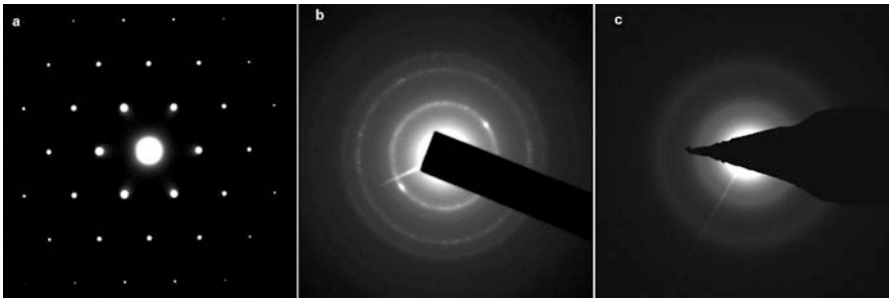

Fig. 7.5 (**a**) An experimentally observed SADP showing the direct beam and an array of diffraction spots from different atomic planes in the case of a single crystalline specimen, (**b**) a polycrystalline specimen, and (**c**) an amorphous region (Reprinted with permission from Li et al. [43]. Copyright 2013 Elsevier)

Convergent Beam Electron Diffraction (CBED)

Historically, CBED is the oldest electron diffraction technique used in the TEM. It was originally developed by Kossel and Möllenstedt, well before LePoole developed SAED [35]. However, because much of diffraction theory, indexing methods, etc. were historically developed for parallel beam SADPs and standard bright field/centered dark field and other imaging techniques build on such patterns, CBED is usually used as an "enriched" variant of SAED. Convergent electron beam is used in CBED, which overcomes the aforementioned both limitations in SAED and also generates much new diffraction information. The region sampled by the convergent beam is a function of its size and the beam-specimen interaction volume, which increases with specimen thickness, but it is generally a lot smaller than the spatial limitations of SAED [44]. CBED patterns contain a wealth of quantitative data on the thickness of the specimen, valence electron distribution, structure factors, chemical bonding, characterization of defects, enantiomorphism, polarity, and even precise lattice strain measurements. The potential drawback of CBED is that the focused probe could generate contamination which can cause localized stresses. In addition, the convergent beam may damage or heat the beam-specimen interaction region of the specimen. Hence these two potential drawbacks should be taken into account when using CBED.

Nanobeam Electron Diffraction (NBED)

Nanobeam electron diffraction has been pioneered by Cowley [35]. As the term implies, it involves diffraction with a nanometer-scale electron beam. NBED can be used to determine local variations of crystallography within large individual unit cells, grain boundary segregation, individual nanoparticles, and dislocation cores. In addition, it is also possible to study crystallographic effects associated with medium-range ordering by correlating atom positions over a distance of a few nanometers. Nanobeam diffraction methods are essential for diffractive imaging with nanometer-scale resolution and have also been used to develop the new field of fluctuation microscopy [35].

7.2.1.2 Image

TEM image contrast arises because of the scattering of the incident electron beam by the specimen. The electron wave can change both its amplitude and its phase as it passes through the specimen, and both types of change can give rise to image contrast. Generally, two kinds of images can be obtained from electron microscopy: one is amplitude contrast dominated image, and the other is phase contrast dominated image. The amplitude contrast includes mass-thickness contrast, Z-contrast, and diffraction contrast, and usually it is used for the imaging of secondary phase in matrix, defects in materials, and low-magnification morphology.

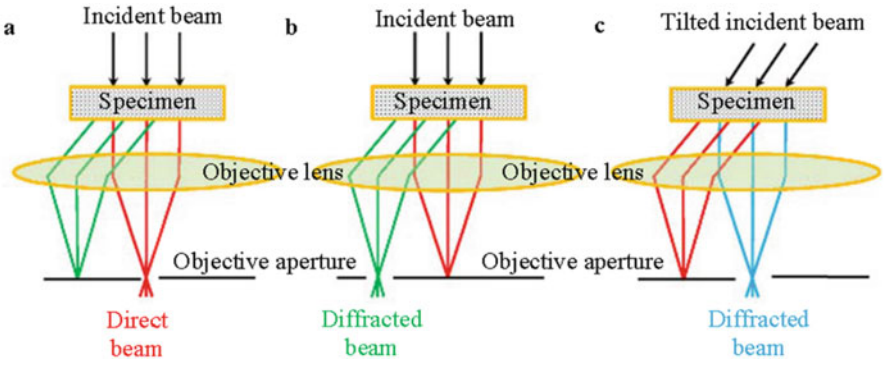

Fig. 7.6 Schematic diagrams showing how the objective lens and objective aperture are used in combination to produce (**a**) BF image, (**b**) DF image, and (**c**) CDF image

The phase contrast is used mainly for atomic-resolution imaging. When the SADP is projected onto the viewing screen or CCD, it will contain a bright central spot that contains the direct beam electrons and some scattered electrons (as shown in Fig. 7.6). The most basic imaging operations, bright field and dark field imaging, can be performed by selecting various spots (direct beam or diffracted beam) in these patterns to form the image.

Bright Field and Dark Field Imaging

In order to view an image, an aperture called the objective aperture is inserted into the back focal plane (BFP) of the objective lens. The bright field (BF) image is formed from the direct electron beam. The dark field (DF) image is formed with a specific off-axis scattered beam. The more off-axis the electrons are, the greater the aberrations and astigmatism they suffer. In order to reduce the aberrations and astigmatism as much as possible, a special DF image called centered dark field (CDF) is employed, where the incident beam is tilted and the scattered beam emerges on the optic axis. Figure 7.6a–c is the schematic showing how the objective lens and objective aperture are used in combination to produce BF image, DF image, and CDF image. The images can be magnified by adjusting intermediate lenses of the microscope, and typical magnification ranges will be ~25,000× to 100,000× for a wide field of view but up to 10^6 × for high-resolution images.

High-Resolution Transmission Electron Microscopy (HRTEM)

HRTEM is one of the most important aspects of TEM. It is to maximize the crystallographic detail of the specimen in the image at atomic scale. From the atomic-scale HRTEM image, clear atomic arrangement, crystal orientation, and

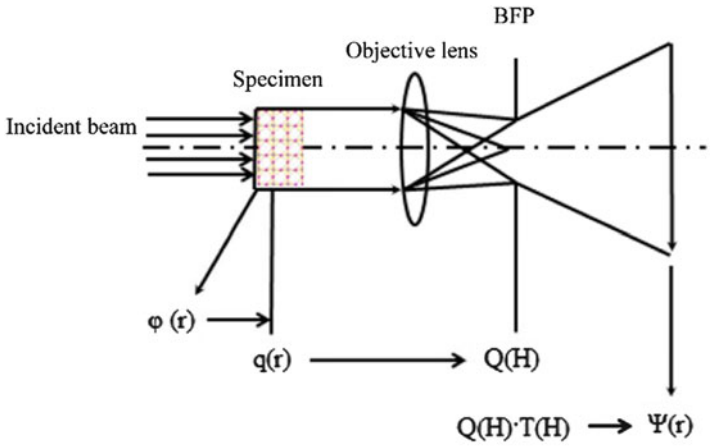

Fig. 7.7 Schematic diagram of optical path for taking an HRTEM image

defects can be obtained [45]. While the difference in the mass-thickness contrast and diffraction contrast can be seen in BF and DF images, the image contrast of HRTEM can be attributed to the phase contrast. Figure 7.7 shows the schematic diagram revealing the optical path that enables taking an HRTEM image. From the schematic, we can see that the electron beam has an interaction with the electrostatic potential of the crystal at first. Subsequently an exit wave q(r) is produced from the bottom surface of the specimen. The exit wave q(r) contains the information of crystal projection potential φ(r) when the electron beam has an interaction with the specimen and it is used as an object wave for the following objective lens. After the exit wave q(r) passes through the objective lens, it experiences a Fourier transformation, and a diffracted wave Q(H) is formed on the back focal plane of the objective lens. Now, we enter the reciprocal space. After that, the diffracted wave Q(H) experiences the Fourier transformation once again through multiplying by the contrast transfer function T(H), and the object wave ψ (r) is obtained for imaging. It is worthy to note that the contrast transfer function T(H) is related to chromatic aberration, spherical aberration, focal shift, and the divergence of electron beam. It is an oscillating function and varies between $+1$ and -1. Therefore, the biggest challenge for HRTEM is the interpretation of image, especially for the image of nanomaterials. In order to identify the atoms in most of the HRTEM image, image simulation based on atomic model, thickness, focus, stigmation, and coma is necessary. From the matched results between the experimental and simulated images, the atom species in HRTEM image can be finally confirmed. Accompanied with the developments of aberration-corrected TEM, especially for the negative spherical aberration-corrected TEM, the direct identification of atomic contrast from HRTEM images is now readily possible [46–48]. However, if we want to analyze the crystal structure or defects atom by atom, spherical aberration-corrected scanning transmission electron microscopy (AC-STEM) would be a better choice.

7.2.2 *Scanning Transmission Electron Microscopy (STEM)*

Figure 7.8 shows a simplified schematic of the STEM optical configuration. A series of lenses focus a beam to form a fine probe, and then the scan coils are used to scan the probe over a thin, electron-transparent specimen in a raster, and a variety of scattered signals can be detected and plotted as a function of probe position to form magnified image in STEM. The STEM image quality depends on the probe. The probe must scan parallel to the optic axis at all times.

One potentially very big advantage for STEM is that the influence of chromatic aberration observed in TEM is absent in STEM images. This advantage makes STEM ideal to deal with thicker samples in comparison to TEM. The reason is the fact that STEM does not use lenses to form the image. The resolution in STEM is limited by the beam dimensions, which is affected by the aberrations. After aberration correction, the probe can be used to scan the sample atom by atom, and the resolution that can be attained is up to ∼0.08 nm at 200 kV and ∼0.06 nm at 300 kV. Another potential advantage is that there is a wide range of possible signals available in the STEM, especially the annular bright field (ABF) [49–51] and high annular angle dark field (HAADF) [52–54] techniques. Figure 7.9 shows the schematic diagram of HAADF-STEM and ABF-STEM techniques.

The HAADF-STEM imaging technique utilizes the scattered electrons that are collected from the sample at relatively high angles (>50 mrad). It can help in

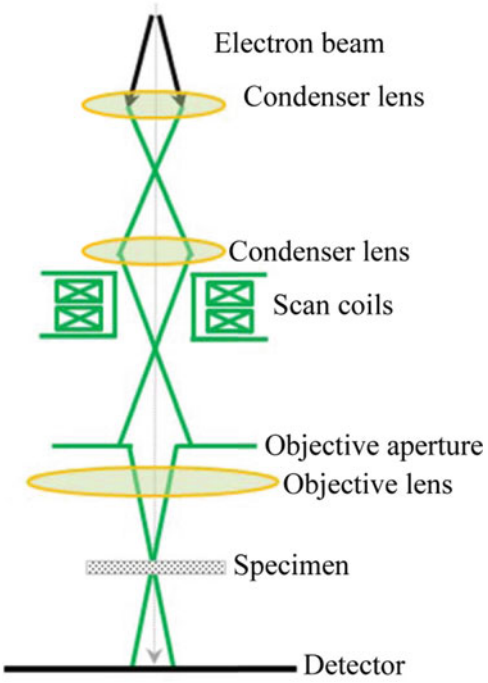

Fig. 7.8 A schematic diagram of the optical path for STEM

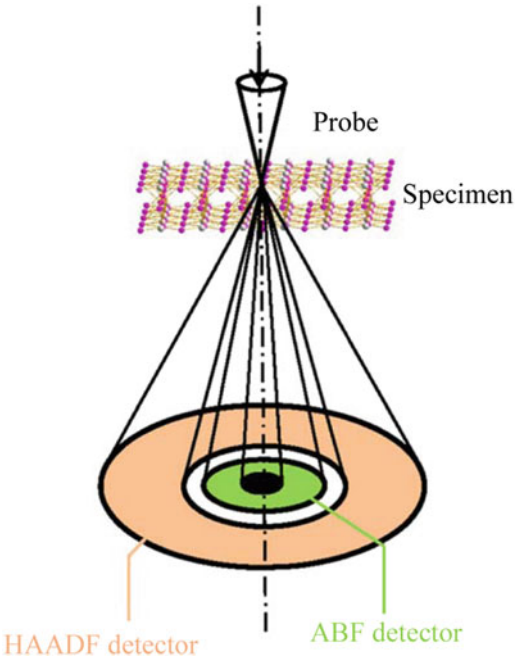

Fig. 7.9 Schematic diagram of HAADF-STEM and ABF-STEM techniques

distinguishing the chemistry of an atomic column because the intensity of contrast in HAADF-STEM images is directly proportional to $\sim Z^{1.4}$ (Z, atomic number) [55]. On the other hand, the ABF-STEM imaging technique utilizes the scattered electrons collected from the sample at relatively low collection angles, and it is very sensitive to light elements, even to the lightest element, hydrogen. The combination of the atomic number sensitivity, light element sensitivity, and high resolution makes advanced STEM an extremely useful tool to the comprehensive study of clusters, alloy nanoparticles, interfaces, and grain boundaries/defects in all kinds of materials.

As mentioned previously HAADF-STEM imaging works remarkably well in the case of nanoalloys; the differences among different metals that make up the nanoalloy are evident due to the intensity dependence on atomic number, with minimum dependence on microscope defocus [56]. This is definitely different from what is expected of bright field imaging, where the signal varies weakly and non-monotonically with Z. Figure 7.10a shows a Z-contrast STEM image simulation of single atoms of different elements, arranged in a 4×4 matrix [57]. The line scan through the center of the atomic positions is shown at the right of the simulated image (Fig. 7.10b). The trend follows approximately a $Z^{1.4}$ relation, very close to the dependence expected by Pennycook et al. [55, 58].

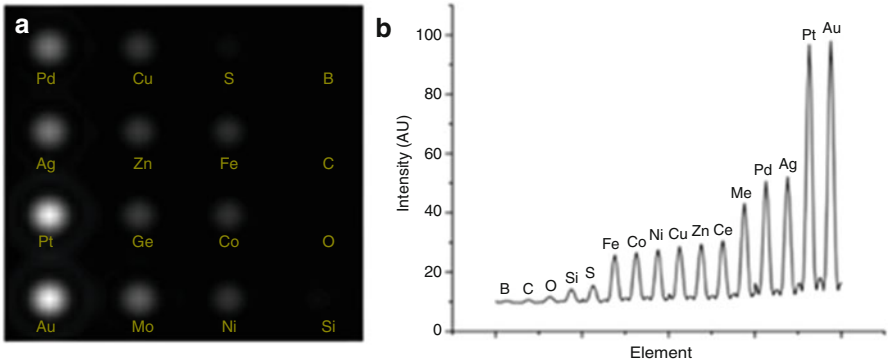

Fig. 7.10 Profiles of intensity obtained from a series of HRSTEM-simulated images (at a defocus of −41 nm). Note the intensity variation with the different elements. In each case the columns of elements have the same number of atoms (Reprinted with permission from Francis et al. [57])

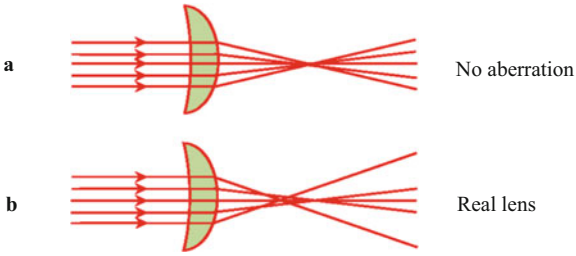

Fig. 7.11 Spherical aberration caused by the lens field acting inhomogeneously on the off-axis rays

7.2.3 Aberration-Corrected TEM/STEM

One major goal of electron microscopy is to be able to acquire images that are directly interpretable and provide new important information about the materials under study. However, because of unavoidable imperfections in the manufacture of electromagnetic lenses, most conventional TEMs suffer from a variety of aberrations that diminish the obtainable resolution. A few of the major ones are spherical aberration, chromatic aberration, and astigmatism. The most severe is spherical aberration (C_s), which causes image delocalization or an inability to define the specific location of a feature, where the image of a point is represented as a blurred disk. This is due to the inhomogeneous forces that the lens (objective for conventional TEM and condenser for STEM) transfers to off-axis electron beams, and the extent of blurring depends on both the magnitude of the spherical aberration coefficient (C_s) and the objective lens strength (Fig. 7.11). The smearing/delocalization limits the resolution of the TEM and the ability to interpret an image properly. To minimize the effects of delocalization, it is critical to image as close to the Scherzer defocus as possible. The Scherzer defocus defined in Eq. (7.1) is the optimal objective lens condition for a given microscope and limits the effect of delocalization:

$$\Delta f_{\mathrm{Sch}} = -1.2(C_s\lambda)^{1/2} \tag{7.1}$$

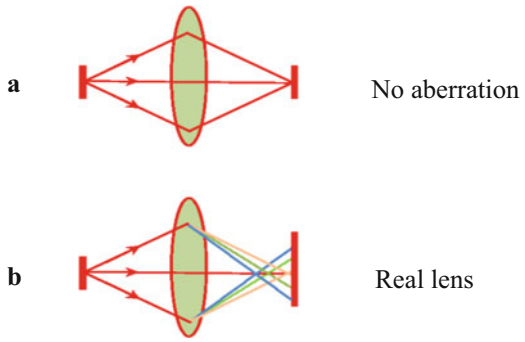

Fig. 7.12 Illustration of the main lens aberrations. (**a**) A perfect lens focuses a point source to a single image point. (**b**) Chromatic aberration causes rays with different energies (indicated by *color*) to be focused differently

Δf_{Sch} is the defocus value, C_{s} is the coefficient of spherical aberration, and λ is the wavelength of the incident electron beam.

In the case of chromatic aberrations, the defocus spread due to chromatic aberration is given by $C_c = \mathrm{d}E/E_{\mathrm{o}}$, where C_c is the chromatic aberration coefficient of the lens, $\mathrm{d}E$ is the energy loss of the electrons, and E_o is the initial beam energy (Fig. 7.12). In order to overcome C_c and achieve an information limit better than $(0.1\ \mathrm{nm})^{-1}$, TEMs are additionally equipped with a monochromator.

7.2.4 Spectroscopic Techniques

In TEM, the most common spectroscopic techniques include energy-dispersive X-ray spectroscopy and electron energy loss spectroscopy. These transform electron microscopy beyond imaging into a far more powerful microscopy, namely, analytical electron microscopy.

7.2.4.1 Energy-Dispersive X-Ray Spectroscopy (EDX/XEDS)

In this technique, the characteristic X-rays are generated when the electron beam strikes the specimen (Fig. 7.13a). These X-rays can be detected by a semiconductor detector and identified as to which characteristic elements they originated from. The X-ray counts as a function of the energy (in keV) form a spectrum, called X-ray energy-dispersive spectrum (Fig. 7.13b). EDX can be used to find the chemical composition of materials, analyze the abundance of specific elements, and show element composition distribution over a much broader raster area. However, in some cases, the energy peaks overlap among different elements, and hence the lightest elements cannot be detected, which sometimes limits the application of EDX. However, EDX can provide fundamental compositional information for a wide variety of materials, including small alloy nanoparticles.

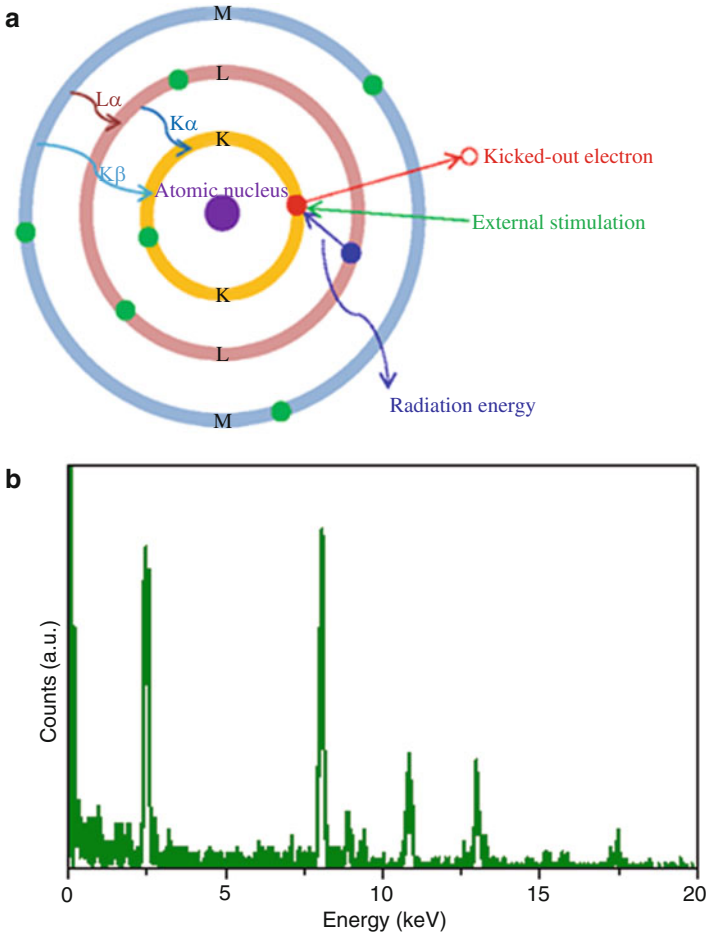

Fig. 7.13 The schematic illustrates the process of X-ray emission in energy-dispersive X-ray analysis (**a**) and a typical EDX spectrum (**b**)

EDX in STEM mode can be used for mapping the composition of a region of interest. In this technique of spectrum imaging, a complete spectrum is collected at every pixel, and the various X-ray peaks could be used for obtaining chemical maps during post-processing [35].

7.2.4.2 Electron Energy Loss Spectroscopy (EELS)

When the electrons pass through the specimen, the transmitted electrons will lose a measurable amount of energy. These electrons as a function of the energy lost form a spectrum. This spectrum is referred to as EELS spectrum. Compared with

EDX, EELS is particularly sensitive to lighter elements, and it is useful for thinner TEM samples. EELS is a more difficult technique but is a useful tool to measure the thickness of specimen, chemical bonding, electronic structure, and atomic composition. EELS involves the energy analysis of inelastically scattered electrons from a nearly monochromatic electron beam due to interaction with electron-transparent specimen. Typically a magnetic prism disperses these electrons according to energy, subsequent to which a spectrometer located at the correct position can collect electrons of a specific energy (Fig. 7.14) [59, 35]. Electron energy loss occurs due to excitations of various internal energy modes – typically electronic (with ΔE in the UV-vis region) and vibrational (IR region) – in the nanoparticle or in molecular adsorbates on the specimen surface. For example, EELS can be used to measure surface plasmon spectra for nanoparticles and vibrational spectra of molecules adsorbed on nanoparticles. The high spatial resolution of EELS can be used to map out surface plasmons across a nanoparticle, which is particularly useful for alloy nanoparticles, where the composition may vary across the particle. High-resolution EELS (HREELS) is a variant of EELS with energy resolution in the 100 meV range. A typical EELS spectrum is shown in Fig. 7.15 [35]. As in the case of EDX, spectrum imaging can be achieved using various features in EELS spectrum when EELS is carried out in the STEM mode.

7.2.5 Energy-Filtered Transmission Electron Microscopy (EFTEM)

EFTEM is an imaging technique utilizing the electron energy loss phenomenon during the electron-specimen interaction. In EFTEM, the images are formed by filtering electrons which have lost specific energy. EFTEM has been successfully and widely employed for obtaining fast elemental maps in TEM mode as it combines the advantages of parallel TEM imaging, i.e., the spatially resolved scattering of a parallel electron beam, with that of EELS. In EFTEM the intensity of any spectral feature in an EELS spectrum can be recorded over a region of interest in the specimen. EFTEM can be used in three different ways. The first one is for contrast enhancement by filtering out inelastically scattered electrons (zero loss filtering). By using zero loss filtering, all the inelastically scattered electrons are filtered out, and the zero loss electrons (elastic) are used for imaging. This improves the contrast in images, particularly for thick specimens and biological specimens where the inelastically scattered electrons lead to significant blurring and poor contrast [35].

On the other hand, by selecting inelastically scattered electrons which have lost a narrow range of energy, EFTEM mapping of various features in EELS spectrum can be achieved. One of the commonly used features is due to plasmon interaction which falls in the range of 1 eV–30 eV. Plasmon imaging is becoming a popular technique, particularly for mapping out low-loss properties of nanomaterials, as the plasmon peak is of high intensity and it is possible to acquire high-quality maps

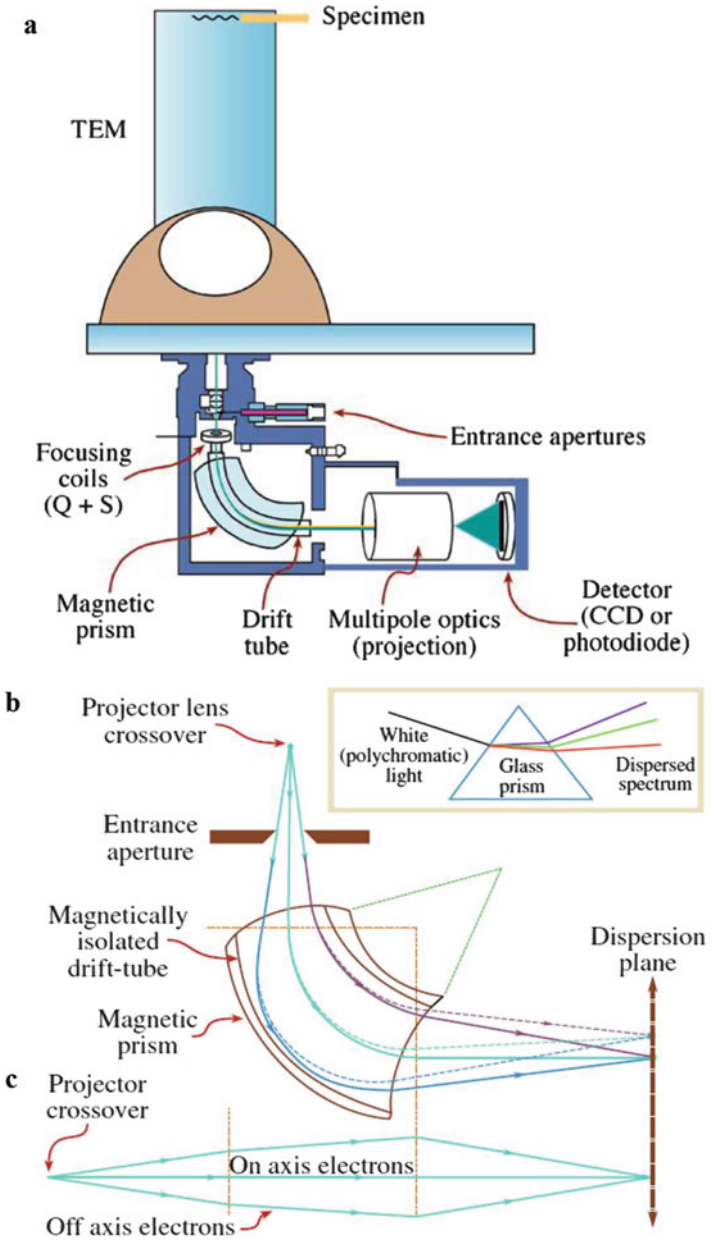

Fig. 7.14 Schematic diagram showing how an EELS is interfaced below the viewing screen of a TEM and the position of the various components (**a**). Illustration of the energy dispersion and the collection of the signals through a spectrometer (**b**) and the lens focusing action in the plane normal to the spectrometer (**c**) (Reprinted with permission from Williams et al. [35]. Copyright 2009 Springer)

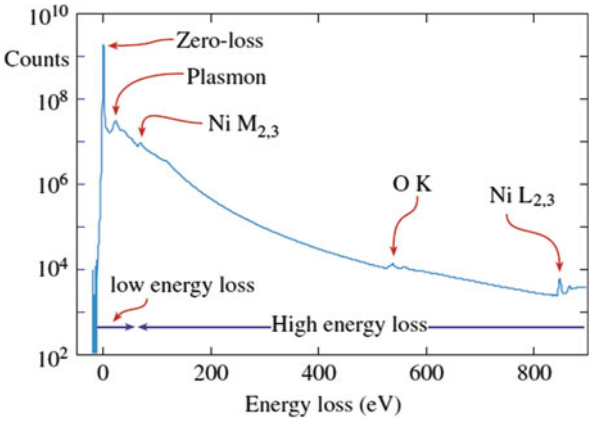

Fig. 7.15 A typical EELS spectrum (Reprinted with permission from Williams et al. [35]. Copyright 2009 Springer)

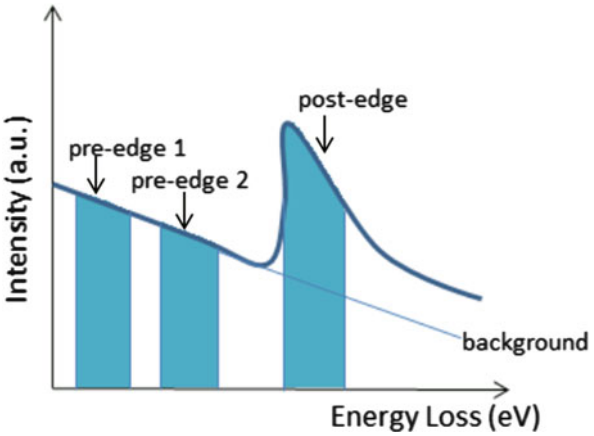

Fig. 7.16 Schematic of three-window method for EFTEM elemental mapping

[60–62]. The other important method in EFTEM imaging is to select inelastically scattered electrons due to inner-shell ionization of elements present in the sample, by which an elemental map can be obtained indicating the elemental distribution in two-dimensional space but averaged over the thickness. Specific features in the electron loss near-edge structure (ELNES) can be used for EFTEM to obtain a chemical bond map where same elements but in different chemical environment could be distinguished [63]. This makes EFTEM a powerful tool in analytical electron microscopy [64].

While filtering, the most common background subtraction method employed is called the three-window method. Two pre-edge windows are used to calculate the background fit and one post-edge window, where the extrapolated background is subtracted from the total intensity, to obtain the edge intensity, as shown in the Fig. 7.16. In contrast to spectrum imaging using EDX or EELS in STEM mode where the beam is scanned over the specimen over a period of time and the spectrum is obtained at every pixel, the fast acquisition of elemental maps

in EFTEM has significant advantage. This is particularly advantageous in beam sensitive specimens. With the use of Cc-corrected microscopes, atomic-resolution EFTEM could be obtained not only in the low-loss region but also at high-loss regions [65, 66]. Therefore, atomic-resolution EFTEM offers another method to determine structural and chemical information with high spatial resolution.

7.2.6 Electron Tomography

Though electron microscopy provides structural, morphological, and compositional information with high spatial resolution, it represents a two-dimensional projection of the specimen under observation [67]. Various three-dimensional details of the crystal such as shape, surface defects, and surface facets are difficult to obtain from the projection image. However it is important to obtain such information to understand the effect of shape, surface facets, defects, etc. on its functionality. In order to overcome this disadvantage, 3D tomography is being used in TEM and STEM. The earliest 3D reconstruction using TEM was published in the 1960s. Subsequently electron tomography was first applied in materials science in the late 1980s. In electron tomography, two-dimensional projection images are recorded every 1° or 2° at a series of tilt angles, typically between −70° and +70°. The reconstruction of the tilt series into a 3D volume of arbitrary size is carried out mostly by three different algorithms: weighted back projection (WBP), algebraic reconstruction technique (ART), and simultaneous iterative reconstruction technique (SIRT).

The resolution of a reconstructed tomogram depends on the number of images in the tilt series as well as the tilt range. Figure 7.17a illustrates the tomography tilt series acquisition and the back projection into a three-dimensional object space, and 17b shows the missing wedge artifact which is due to the limited angle tilt series acquisition [68]. In order to minimize such effects and artifacts, so as to give

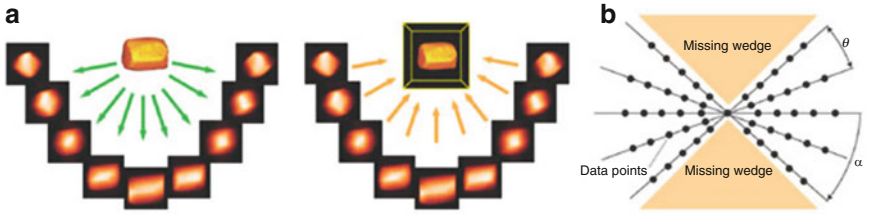

Fig. 7.17 (**a**) Illustration of two-stage tomography process with (*left*) acquisition of an ensemble of images (projections) about a single tilt axis and (*right*) the back projection of these images into 3D object space. (**b**) Representation in Fourier space of the ensemble of projections, indicating the undersampling of high-spatial-frequency information and the missing wedge of information brought about by a restricted tilt range (Reprinted with permission from Midgley et al. [68]. Copyright 2016 Nature Publishing Group)

accurate and reliable statistics in the 3D measurements as well as limit the effect of the "missing wedge," reconstruction of the entire object is obtained using a dual axis approach in which a second tilt series is acquired whose tilt axis is perpendicular to the first. By combining the two tilt series, the missing wedge of data is reduced to a "missing pyramid." This is achieved by acquiring a tomogram in a single tilt series wherein two data sets of the same area are taken, but they are rotated in-plane by about 90° with respect to each other. With the aid of the software, the transformation parameters between the two sets are determined and added, either in Fourier space or in real space leading to a more complete reconstruction. Ultrahigh-tilt holders in which the use of a needle-shaped sample allows 360° rotation eliminates missing wedge artifacts [69].

In TEM, Tomography is extensively used in biology, polymers, and also to determine the three-dimensional structure of the pores in zeolites and amorphous materials [70–72]. In the case of strongly diffracting crystalline specimens, the bright field TEM images do not satisfy the projection requirement for tomography reconstruction, i.e., the recorded signal should be a monotonic function of some physical properties. In this case, STEM tomography based on high-angle annular dark field images, where the intensity is approximately proportional to $Z^{1.4}$ and the projected thickness, is an ideal alternative [55, 68]. Due to this dependence of intensity on Z, it leads to chemically sensitive structural imaging, where the heavier elements can be distinguished from the lighter elements. Thus, depending on the nature of the specimen, employing either TEM or STEM, electron tomography has become a routine in catalyst characterization [73].

However when there are multiple elements in the material with similar atomic numbers, interpretation of chemical information from HAADF-STEM imaging is neither straightforward nor reliable. In this context, spectroscopic electron tomography is used to obtain the three-dimensional chemical mapping: EFTEM, EELS, and EDX can be used in this regard. Using 2D EFTEM imaging and a tomographic approach combines the ability of the traditional electron tomography to obtain information in 3D with nanoscale spatial resolution and the chemical selectivity of the EFTEM imaging [74–76]. Similarly STEM-based EELS tomography consists of acquiring an EELS spectrum image (SI) tilt series [77]. The spectral features are processed to obtain energy-filtered images and reconstructed to obtain chemically sensitive tomographic reconstruction. EDX-STEM is another STEM-based tomography technique for chemically sensitive 3D imaging [78–80]. Along with STEM images, EDX elemental maps are acquired at every tilt during a tilt series, and maps corresponding to each of the elements are reconstructed to obtain the 3D chemical map.

7.2.7 Holography

In holography, the electron beam is spilt into two parts, and one of them is passed through the specimen using a biprism. The other acts as the reference. The beam which is traveled through the specimen, which underwent a phase change, and

the reference beam which traveled through vacuum are allowed to interfere. The interference fringes are the electron holograms. In the absence of a specimen, a uniform interference pattern is produced, but when a specimen is present, the fringes carry the information on the specimen due to the phase change involved. Therefore electron holography allows the phase shift of the electron wave to be recovered. Any phase shift is sensitive to local magnetic and electrostatic potential, and therefore information on specimen, such as electric field, magnetic field, etc., can be obtained from the hologram. Figure 7.18 shows the formation of a hologram in an electron microscope [68].

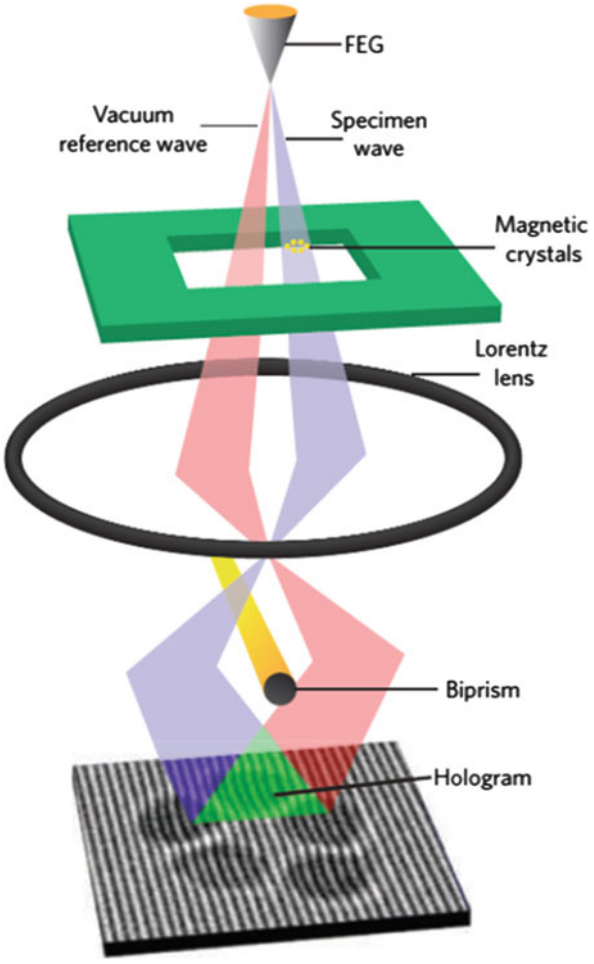

Fig. 7.18 Illustration of the application of a voltage to an electron biprism located close to a conjugate image plane in a field-emission electron gun (FEG) TEM, to overlap a vacuum reference electron wave with the electron wave that has passed through a region of the specimen to form an off-axis electron hologram. Variations in the spacing and direction of the recorded holographic interference fringes contain information about the projected magnetic flux density inside and surrounding the crystals (Reprinted with permission from Midgley et al. [68]. Copyright 2016 Nature Publishing Group)

7.3 Monometallic Nanoparticles: Shape, Size, and Morphology Control

Metal nanoparticles have important applications in various fields such as catalysis, sensing, bioimaging, etc. Various synthesis methods have been developed to fabricate metal nanoparticles of Au, Pt, Pd, Ag, Co, Cu, etc. The properties of these particles strongly depend on their size and shape. Therefore, considerable effort has been directed toward the synthesis of particles with well-controlled size and surface facets.

Physical and chemical methods have been developed to synthesize metal nanoparticles. The physical methods involve laser ablation, evaporation-condensation, etc. [81, 82]. The absence of solvent/surfactant contamination is an advantage in physical synthesis methods in comparison with chemical processes. But chemical synthesis offers a low-cost method to synthesize nanoparticles of a wide range of size and shape with different ways to control the size and shape. Among chemical methods, the most common methods of synthesis of metal nanoparticles include (1) surfactant-assisted method, (2) polyol method, and (3) seed-mediated synthesis. Surfactant-assisted synthesis involves the use of a size-/shape-directing surfactant in aqueous or organic medium. The shape and size of the nanoparticle depend on the binding of the surfactant to the various crystal facets. For example, preferential removal of alkylamine surfactant from {111} planes to that of {100} in the solution synthesis of Au results in ultrathin single crystalline nanowires by oriented attachment along <111> direction [83]. Size- and shape-controlled synthesis of metal nanoparticles by seed-mediated synthesis has been successfully employed in many metallic systems [84]. It is a two-step synthesis method, where the first step involves the preparation of monodisperse seed particles and the second step involves their growth to form nanoparticles of different size and shape in the growth solution. The separation of nucleation and growth phases in this method allows careful control of the resultant size and shape. In polyol method, the synthesis is carried out in poly(ethylene glycol)s; the ethylene glycol acts as the solvent as well as the reducing agent for the formation of metal nanoparticles from its salt [85]. It was also observed that the length of the polyol affects the morphology of the particle by acting as in situ capping agent [86].

There are multiple parameters affecting the resultant nanoparticle morphology in the wet chemical methods. For example, Langille et al. demonstrated the role of Ag^+ ions and halide ions in the formation of different shapes of Au nanoparticles [87]. They concluded that in the seed-mediated synthesis of Au nanoparticles, in the absence of Ag^+ ions, the larger halide ions favor the formation of lower energy surface facets, i.e., more thermodynamically favorable products form with increasing concentrations of bromide and iodide, with the effects of iodide being stronger than those of bromide. In the absence of larger halide ions, increasing concentrations of silver ions were observed to stabilize particles with a greater number of exposed surface atoms per unit surface area, enabling the formation of high-index nanostructures.

Ag nanocubes with sharp corners and edges were synthesized in aqueous medium, with an average edge length of 35–95 nm [88]. The method involves the formation of AgCl octahedra by mixing CF_3COOAg with cetyltrimethylammonium chloride, followed by the nucleation and growth of Ag nanocrystals in the presence of ascorbic acid and $FeCl_3$. The Fe^{3+}/Fe^{2+} redox pair removed multiply twinned seeds through oxidative etching resulting in single crystalline Ag nanocubes, whereas chloride ions played an important role in the formation of the cube shape.

7.3.1 TEM/STEM Characterization of Monometallic Nanoparticles

TEM/STEM and associated techniques remain as important tools in the characterization of metal nanoparticles to investigate their size, shape, and surface facets. Zhang et al. observed the formation of Pd nanostructures ranging from nanocubes enclosed by {100} facets to octahedrons by {111} facets depending on the concentration of HCl, which determines the reduction kinetics [89]. The synthesis involved reduction of H_2PdCl_4 in aqueous solution by ascorbic acid. The increasing amount of HCl resulted in more powerful oxidative etching preferentially occurring at the corners of cubic Pd nanocrystals, promoting the formation and enlargement of Pd {111} facets at the cost of the shrinkage of {100} facets. This eventually results in the formation of thermodynamically favored shape with maximum expression of {111} facets, i.e., the octahedron. Figure 7.19 shows the schematic representing the formation of different shapes and the respective TEM images.

Wang et al. developed a method to quantitatively analyze the reaction kinetics involved in the polyol synthesis of noble-metal nanocrystals and further revealed a quantitative correlation between the initial reduction rate and the twin structure of seeds and nanocrystals, using Pd as an example [90]. They used UV-visible spectroscopy to obtain the concentration of reactants with reaction time. In their study they observed that the type of polyol used and the temperature affected the shape of the particle, and they identified various temperature regimes to obtain different shapes of the nanocrystal. Figure 7.20 shows the TEM images of the Pd crystals obtained using ethylene glycol (EG) and diethylene glycol (DEG) and the effect of temperature.

Platinum nanoparticles of various shapes were obtained by using $Mn_2(CO)_{10}$ to control the shape of Pt nanocrystals [91]. The zerovalent transition metal, Mn, decomposed from metal carbonyl and served as the shape-directing agent, whereas CO acted as the reducing agent. High-quality Pt nanocrystals are synthesized in various morphologies, including octahedra, icosahedra, cubes, truncated cubes, cuboctahedra, spheres, tetrapods, star-shaped octapods, multipods, and hyperbranched structures. During the synthesis, low carbonyl-to-$Pt(acac)_2$ ratio and/or long reaction time resulted in Pt nanocrystals with various shapes such as tetrapods,

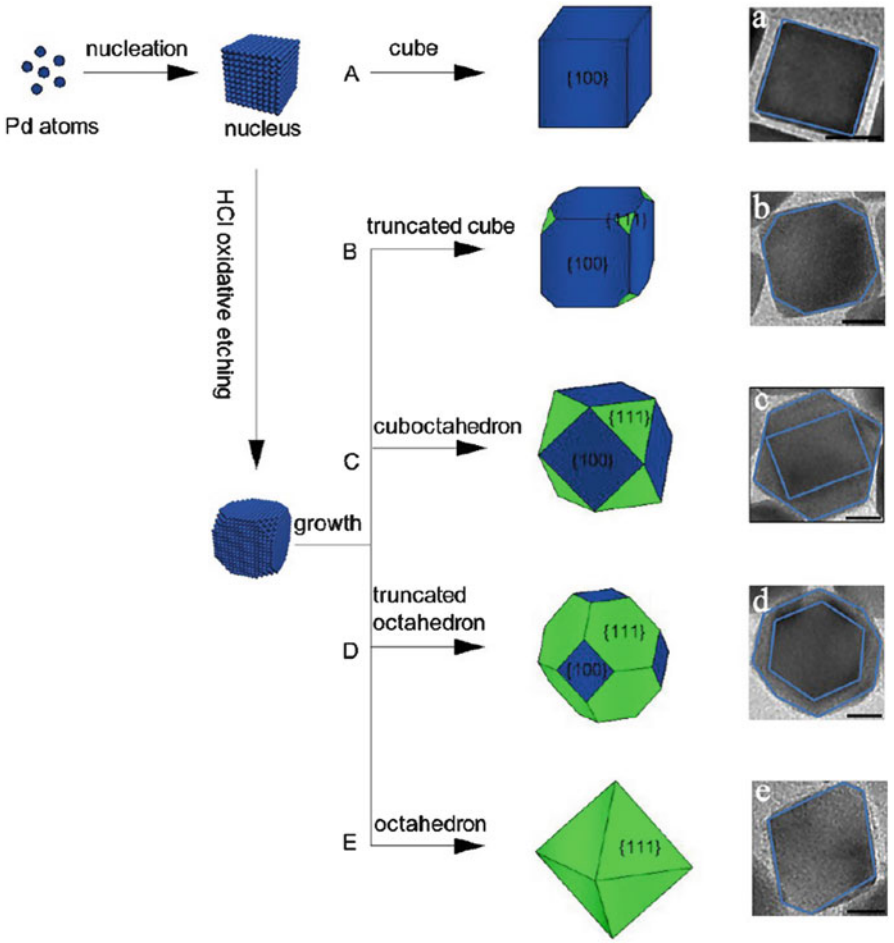

Fig. 7.19 Schematic illustration of shape evolution of the Pd nanocrystal (*left*) and the corresponding TEM images for various morphologies (scale bars, 10 nm) (**a-e**), where slight truncation at the corner of cubic Pd was induced by HCl oxidative etching in the early stage and then continuous atomic addition to facets promotes the enlargement of {111} facets and finally results in the formation of octahedral Pd bounded by {111} facets (Reprinted with permission from Zhang et al. [89]. Copyright 2014 American Chemical Society)

octapods, multipods, and hyper-branched nanocrystals. Figure 7.21 shows TEM images and HRTEM image of Pt octahedra obtained by this method.

The geometric phase analysis (GPA) is a method to measure strain or variation in ideal structure in crystals from high-resolution transmission electron microscopy images. In an HRTEM image, the local amplitude and the geometric phase of lattice fringes can be determined by filtering in Fourier space. The phase images determine the displacement of the lattice fringes and can be used to measure the reciprocal

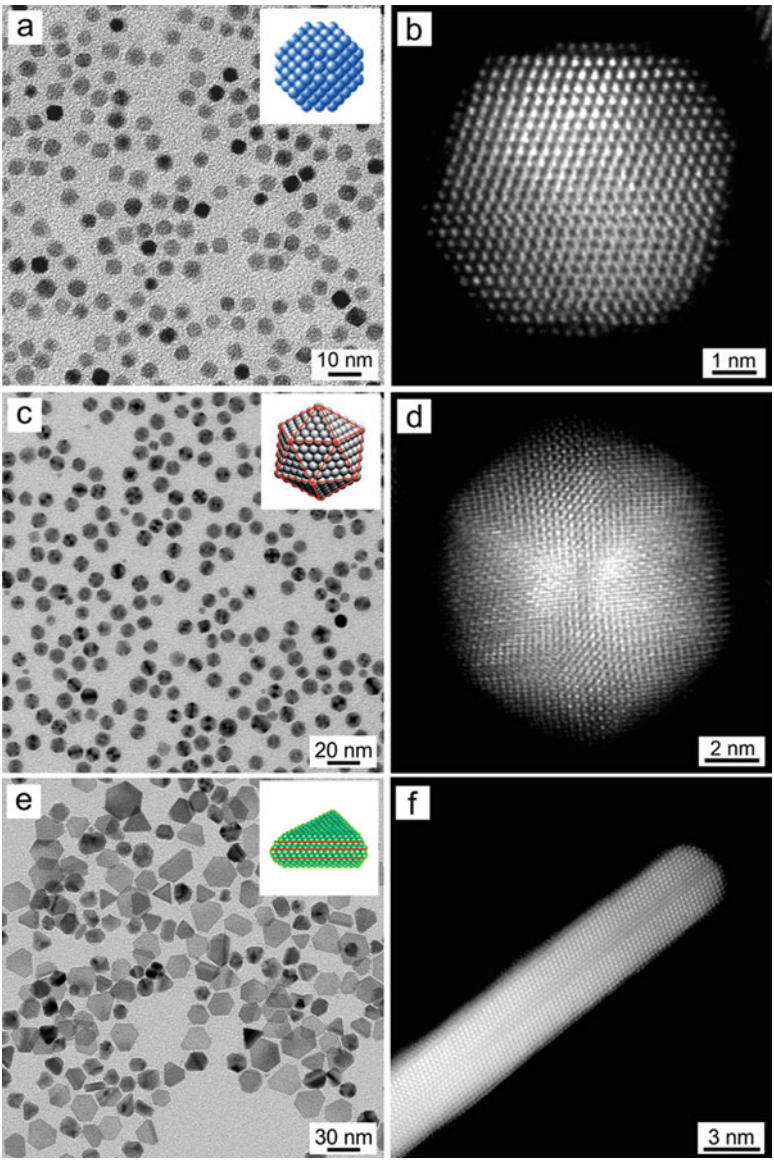

Fig. 7.20 Palladium nanocrystals obtained under different reaction conditions of temperature and polyol nature: (**a**, **b**) truncated octahedral in EG at 140 °C; (**c**, **d**) icosahedra in DEG at 140 °C; (**e**, **f**) nanoplates in DEG at 75 °C. (**a**, **c**, **e**) TEM images of the Pd nanocrystals produced at each condition. The insets show the corresponding atomic models of the nanocrystals with the twin planes or stacking faults being delineated in *red*. (**b**, **d**, **f**) High-resolution HAADF-STEM images of individual nanocrystals, revealing (**b**) single crystalline, (**d**) multiply twinned, and (**f**) stacking fault-lined structures. Note that (**f**) was taken from the side face of a nanoplate (Reprinted with permission from Wang et al. [90]. Copyright 2015 American Chemical Society)

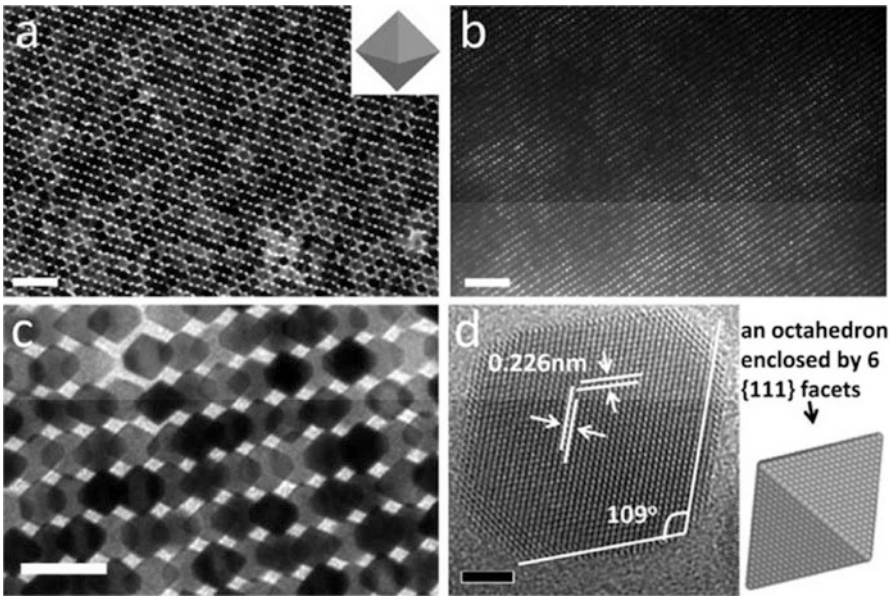

Fig. 7.21 (**a**–**c**) TEM images and (**d**) HRTEM image of Pt octahedra and (**a**) a superlattice and (**b**) a 3D superlattice formed from the Pt octahedra. Scale bars: (**a**, **b**) 50 nm, (**c**) 20 nm, and (**d**) 2 nm (Reprinted with permission from Kang et al. [91]. Copyright 2013 American Chemical Society)

lattice vector. Therefore it could show how uniform is the spacing between the fringes and how it varies from its ideal positions [92]. The phase image can be compared with simulated images to determine the accuracy of the measurement. GPA has been employed in studying nanocrystals, interfaces between crystals, strained multilayers, etc. Figure 7.22 shows the AC-HRTEM image of decahedral Au particle and the strain mapping of the particle using GPA [93].

Surface irregularities in gold decahedra nanoparticles were obtained using off-axis electron holography [94]. Figure 7.23 shows the phase and unwrapped phase images obtained by reconstruction ((a) and (b)). The oriented particle shows a smooth contour from the center to the edge, and no abrupt phase shift was observed. In Fig. 7.23b the phase image was calibrated using the mean inner potential of the FCC Au. The thickness computation line profile is shown in Fig. 7.23d. The phase image (Fig. 7.23c) has been amplified 2.5×, and the routine employed can reach a phase resolution value of $2\pi/1000$.

Nicolette et al. studied the 3D spatial distribution of localized surface plasmon resonance (LSPR) modes of a silver nanocube supported on a dielectric substrate [77]. Nonnegative matrix factorization (NMF) of the data set in the range of 1–4 eV acquired using monochromated STEM EELS was used to obtain EELS-LSPR maps. Compressed sensing tomography algorithm was used for the 3D tomography reconstruction. Figure 7.24 shows the 3D visualization of the LSPR modes of silver nanocubes obtained by this technique [77].

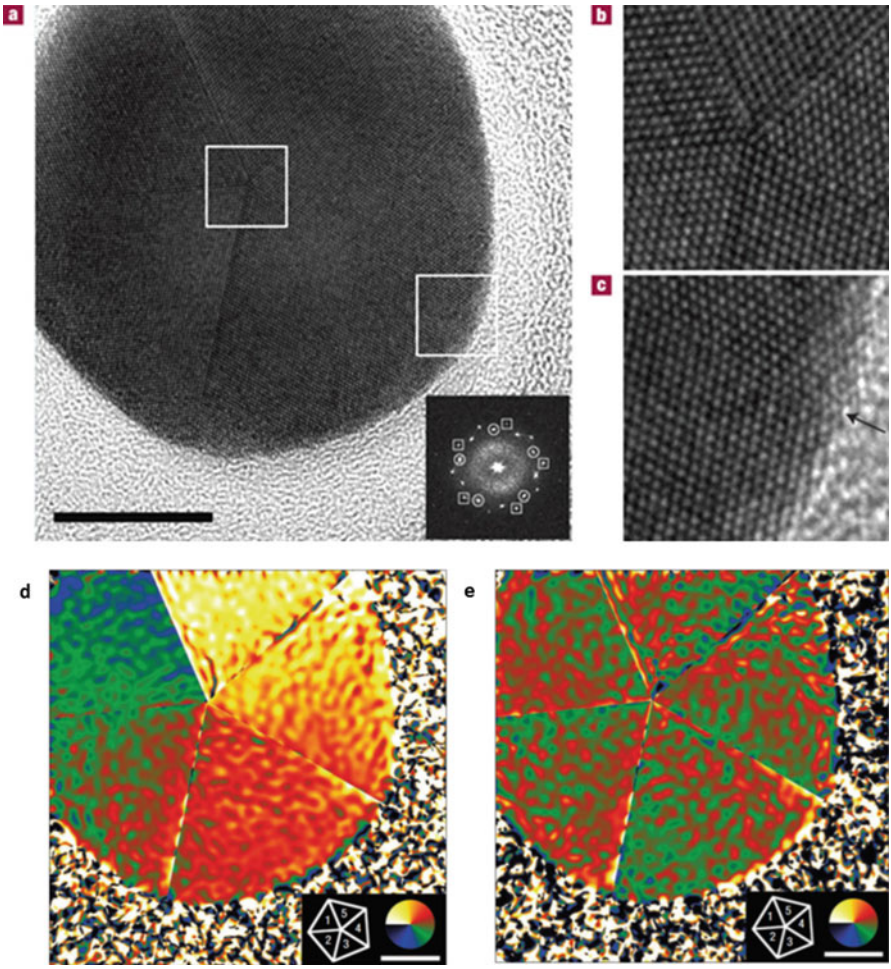

Fig. 7.22 AC-TEM image of a 17-nm-radius defect-free decahedral Au nanoparticle. (**a**) The image shows the fivefold rotational symmetry marked by twin boundaries that originate at the center of the particle. Equivalent 111 and 002 reflections in the diffractogram (inset) are marked by circles and squares, respectively. The scale bar is 10 nm. (**b**) An expanded view of the particle core (marked by the square at the center of a) shows the intersection of the five twin boundaries. (**c**) An enlarged view of the particle edge (region marked by a square on the right side of a) shows the termination of one of the twin interfaces. (**d**) Lattice rotation distribution in the decahedral Au nanoparticle in a. The rotation map gives the internal rigid body rotation of the crystallographic lattice. The scale bar is 5 nm and the color scale indicates −2 to +5 deg. rotation. (**e**) Shear-strain distribution in the decahedral Au nanoparticle in a. The shear-strain map shows the shear gradient across each segment of the decahedral particle. The scale bar is 5 nm and the color scale indicates −5 to +5% shear strain (Reprinted with permission from Johnson et al. [93]. Copyright 2008 Nature Publishing Group)

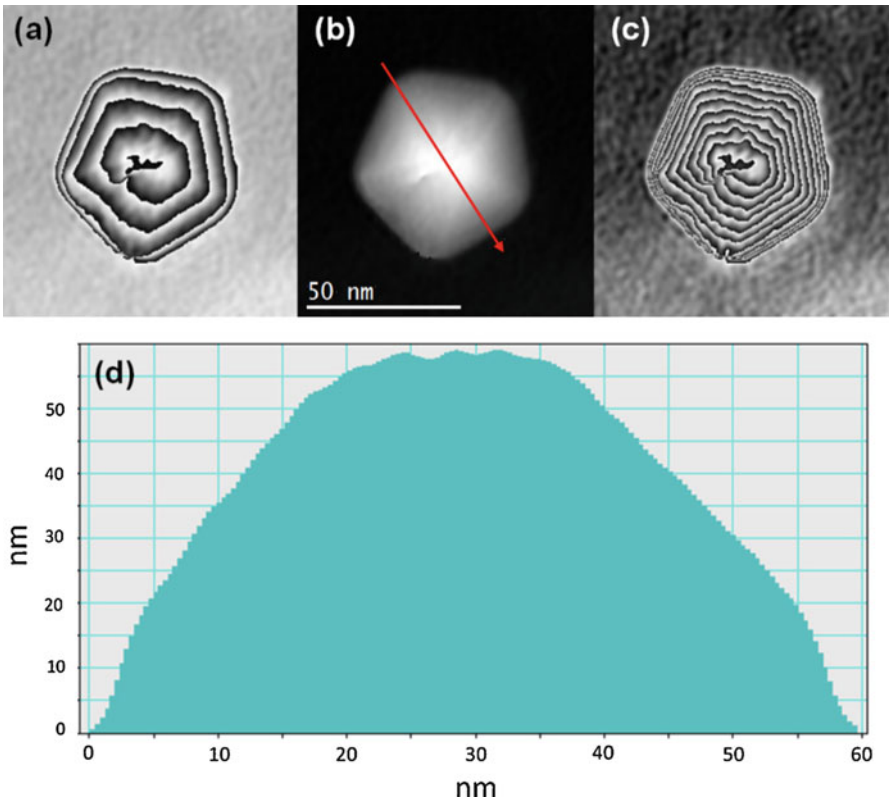

Fig. 7.23 Au decahedral nanoparticle: (**a**) phase-reconstructed image, (**b**) unwrapped phase image, (**c**) 2.5× amplify-phase lines processed, and (**d**) computed thickness obtained using the Au crystalline potential (Reprinted with permission from Cantu-Valle et al. [94]. Copyright 2013 Elsevier)

In recent years, much progress has been achieved in the field of atomic-resolution electron tomography. For example, Goris et al. employed compressive sensing algorithm to reconstruct atomic-scale surface facets in Au nanorods from a limited number of HAADF-STEM images [95].

7.3.2 TEM/STEM Characterization of Supported Metal Nanoparticles

Metal nanoparticles supported on carbon or oxide materials are an important class of materials in catalysis. In the case of an inert support, it provides stability to the metal particle against sintering and also allows dispersion of the nanoparticle uniformly. In addition, catalytically active supports are used, where the support play an important

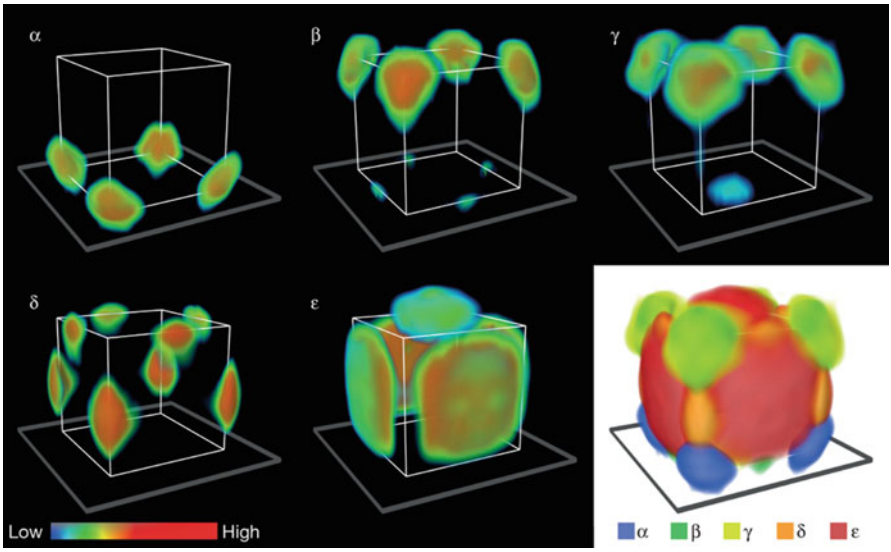

Fig. 7.24 3D visualization of the LSPR components of a silver nanocube. The 3D images (**α**–**ε**) were obtained by tomographic reconstruction of the EELS maps of the respective LSPR components. The visualizations are voxel projections of the reconstructed 3D volumes. The color bar indicates the LSPR intensity. The image in the bottom right of the figure shows a combined 3D rendering of all the components (Reprinted with permission from Nicoletti et al. [77]. Copyright 2013 Nature Publishing Group)

role in catalysis. The catalytic activity depends on the constituent materials, its size and shape, as well the interface. TEM is a useful tool for determining the size, geometry, and nature of the interface. Spectroscopic methods compliment the imaging by providing simultaneous analytical information. In recent years AC-TEM/STEM is increasingly used in the investigation of such catalysts [96].

Han et al. studied the interaction of Au nanoparticles on MgO cubes by AC-STEM [97]. They showed that the interfacial separation distance is sensitive to the orientation of the nanoparticles supported on the MgO(001) surface. In metal nanoparticles on supports, the support stabilizes the nanoparticles on it, and therefore removing the surfactant might increase its functionality without altering the size of the particles. In order to examine the stability after removal of the stabilizing ligand, Lopez-Sanchez et al. carried out STEM analysis to characterize the particle size distributions [98]. HAADF images of the gold particles reveal that they are a mixture of cuboctahedral (Fig. 7.25a), singly twinned (Fig. 7.25b), and multiply twinned (Fig. 7.25c) morphologies, with the twinned variants dominating. HAADF images of gold particles subjected to the water washing treatments (Fig. 7.25d–l) show that they all retain a mixed morphology of particles. The samples washed for longer time periods show more distinctly faceted surfaces, as a consequence of restructuring after losing a significant fraction of their protective PVA ligands.

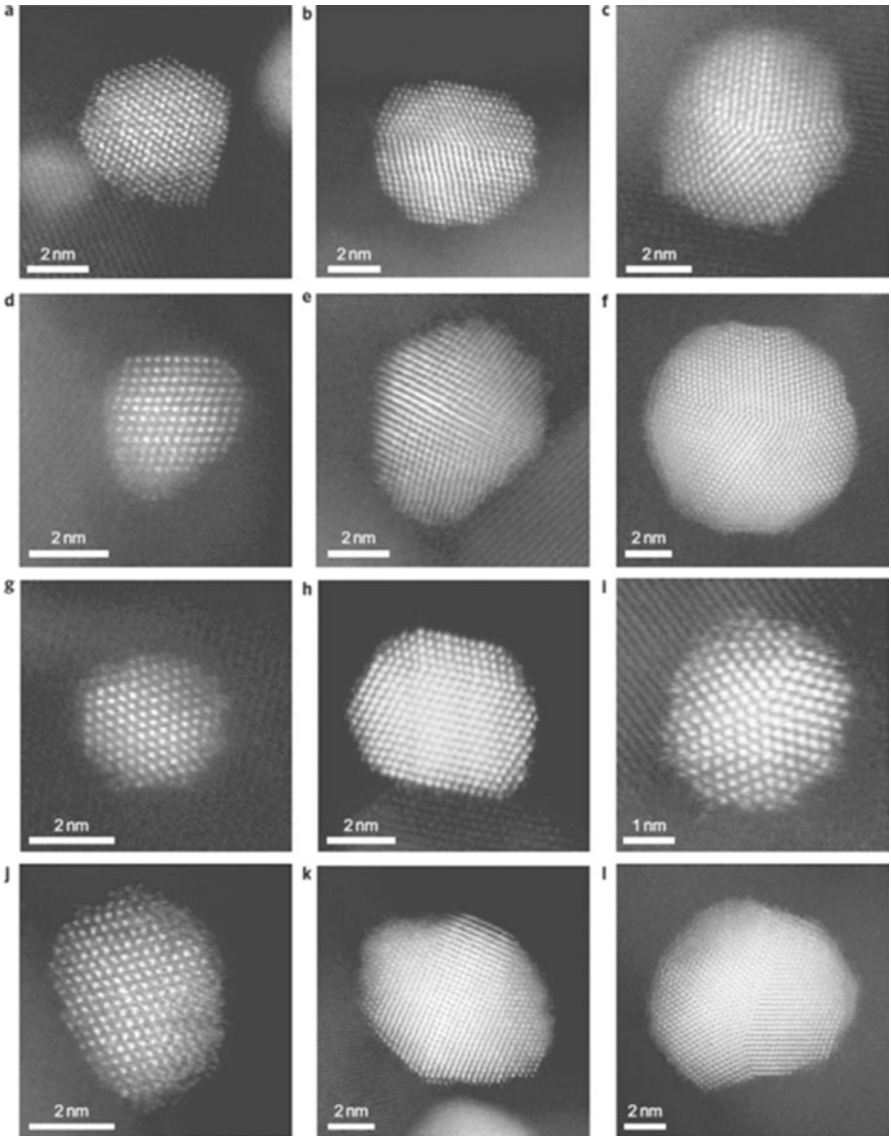

Fig. 7.25 Representative HAADF-STEM images showing that the water extraction procedure developed for removing the stabilizing PVA molecules from the immobilized supported gold nanoparticles does not significantly increase particle size or affect their morphology. (**a**–**c**) HAADF-STEM images of the immobilized sol on TiO_2 dried at 120 °C, showing characteristic cuboctahedral (**a**), singly twinned (**b**), and multiply twinned (**c**) morphologies. (**d**–**l**) Representative HAADF-STEM images of the immobilized sol on TiO_2 refluxed at 90 °C for 30 min (**d**–**f**), refluxed at 90 °C for 60 min (**g**–**i**), and refluxed at 90 °C for 120 min (**j**–**l**). Panels a, d, g, and j show cuboctahedral particles; panels b, c, e, f, h, i, k, and l are characteristic twin morphologies found in singly twinned or decahedral-type particles (Reprinted with permission from Lopez-Sanchez et al. [98]. Copyright 2011 Nature Publishing Group)

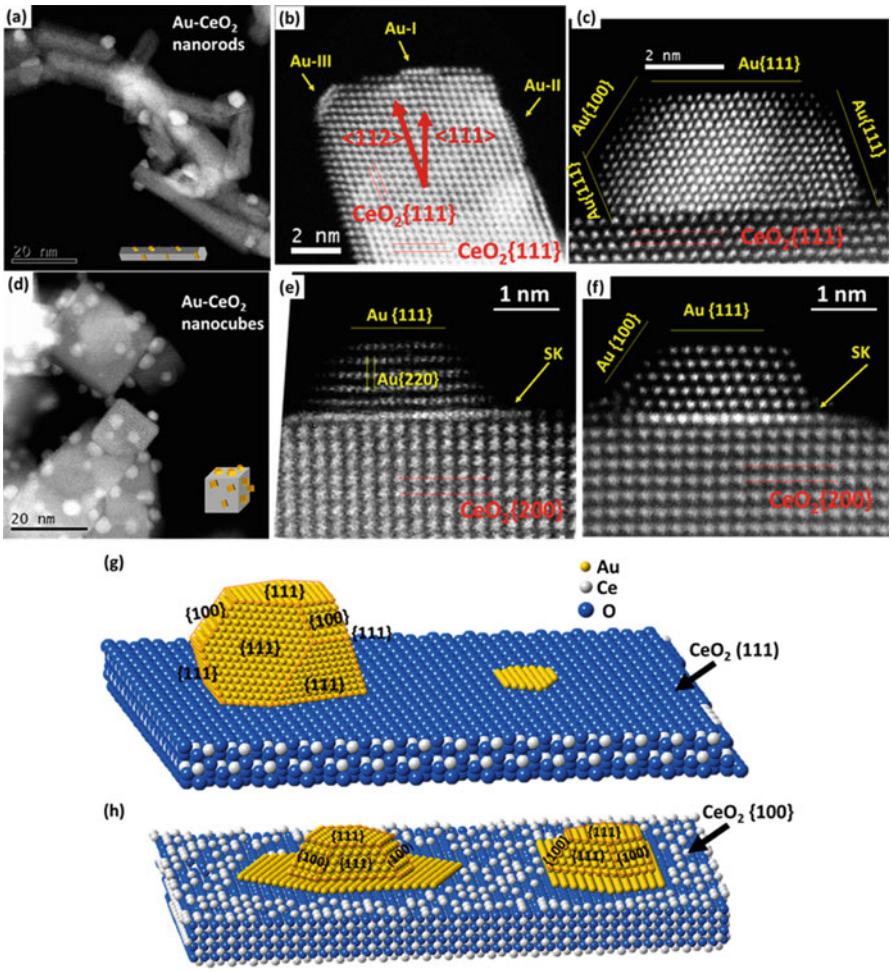

Fig. 7.26 Morphology and atomic structures of Au-CeO_2 nanostructures. (**a**) Low-magnification HAADF image of Au-CeO_2 nanorods. (**b**) Atomic-resolution HAADF image of Au rafts on a CeO_2 nanorod. (**c**) Atomic-resolution HAADF image of an Au nanoparticle on a CeO_2 nanorod. (**d**) Low-magnification HAADF image of Au-CeO_2 nanocubes. (**e**) Atomic-resolution HAADF image of an Au particle with a Stranski-Krastanov (SK) layer supported by a CeO_2 nanocube. (**f**) Atomic-resolution HAADF image of another Au particle with a SK layer supported by a CeO_2 nanocube. (**g**) Schematic view of an Au particle and raft supported by the CeO_2 (111) surface. (**h**) Schematic view of Au particles supported by the CeO_2 (100) surface (Reprinted with permission from Lin et al. [99]. Copyright 2015 American Chemical Society)

Au nanoparticles supported on CeO_2 are another commercially important catalyst. Lin et al. employed AC-STEM to analyze the adhesion and atomic structures of gold nanoparticle catalysts supported on ceria nanocubes and nanorods [99]. Figure 7.26 shows the shape and surface facets of Au on CeO_2 nanocubes and nanorods. It is observed that Au rafts and Au nanoparticles are present, predominantly on (111)

surface of CeO_2 nanorods (Fig. 7.26b, c). In the case of CeO_2 nanocubes, Au(111) was preferentially grown on CeO_2(001) surface (Fig. 7.26e, f). In the case of CeO_2 nanocube, the first Au atomic layers at the Au-CeO_2 interface show an extra-bright contrast due to the extended Au atomic layers. Because of the extended layer feature, the growth of Au on CeO_2 nanocubes is categorized as Stranski-Krastanov (SK) growth.

They observed that under the reducing conditions of water-gas shift reaction, the extended gold atom layers and rafts vanish. In addition, the size and shape of Au nanoparticles supported on CeO_2 nanorods remained unaltered, whereas increase in particle size and change in shape were observed in the case on Au nanoparticles supported on CeO_2 nanocubes. This shows that the morphology and structure of gold strongly depend on the surface structures of ceria supports and the reaction environment.

In some cases, the support used could influence the TEM/STEM imaging of the particles. For example, Si supported on graphene facilitated its better imaging compared to that on amorphous carbon film on conventional TEM grids, and also it allowed the observation of the surfactant layer on the surface [100].

Kundu et al. investigated the morphology and thermal stability of Au-SiO_2 with the help of HAADF-STEM tomography [101]. From the tomogram, it was confirmed that Au nanoparticles are present explicitly on the surface of SiO_2 in the as-synthesized composite, whereas Au diffuses within SiO_2 at high temperatures. In another example HAADF-STEM tomography was employed to investigate the 3D distribution of Au nanoparticles in Ti-SiO_2 matrix. The Au@Ti-SiO_2 system is a promising catalyst material exhibiting room temperature CO oxidation [102]. Figure 7.27a shows the HAADF-STEM image of the Au@Ti-SiO_2 sample. Small Au nanoparticles, observed as bright contrast in the Z-contrast image, are distributed throughout the sample. Intersection of two orthoslices of the reconstruction is shown in Fig. 7.27b, with particles observed within the oxide matrix and also on the surface. Figure 7.27c shows the corresponding 3D volume rendering [102].

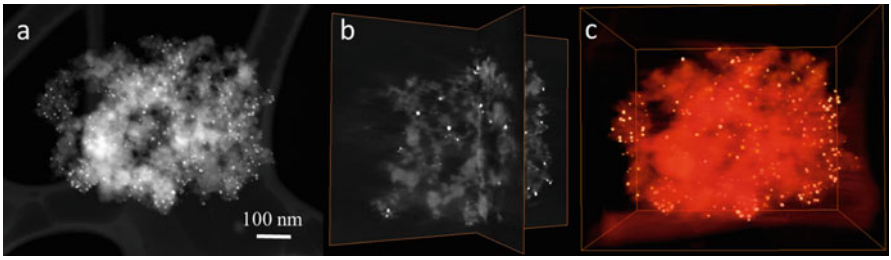

Fig. 7.27 (**a**) HAADF-STEM image of Au@Ti-SiO_2, (**b**) intersection of two orthoslices of the 3D reconstruction, and (**c**) corresponding volume rendering (Reprinted with permission from Soni et al. [102]. Copyright 2017 American Chemical Society)

7.4 TEM/STEM Characterization of Bimetallic Nanoparticles

Bimetallic nanoparticles are employed as industrial catalysts because of the significant additional potential they offer over monometallic counterparts. In addition to catalysis, they are vital for optical, magnetic, and sensing applications. Some of the important reactions involving bimetallic catalyst include methanol oxidation, formic acid oxidation, and oxygen reduction reaction. This potential derives from the synergistic effects of the constituent metals and also from the ability to control those properties through altering structure and chemical ordering. The resulting tunability in properties of bimetallic nanoparticles offers significant advantages over monometallic equivalents that make them highly desirable systems for the development of catalysts tailored to specific reactions. For example, Pt is a better catalyst for oxygen reduction reaction (ORR) when combined with other metals such as Ni, Co, and Fe [103]. Much effort has been directed to size-, shape-, and composition-controlled synthesis of bimetallic nanostructures. Random alloys, intermetallics, and core-shell nanostructures are investigated in this direction. A surfactant-free solvothermal synthesis of shape- and size-selective octahedral PtNi NPs was reported by Cui et al. [104]. The shape-selective NPs show an exceptional ORR activity due to the alloy particle surface composition. At a surface composition of about 40 at. % Pt, 9.5-nm-sized PtNi octahedra reached tenfold Pt mass-based ($\sim$1.45 A/mgPt) activity gain at 900 mV/RHE and 5 mV/s anodic sweep rate over the state-of-the-art commercial carbon-supported Pt electrocatalysts. The structural characterization of these materials with atomic resolution is crucial in designing such catalysts with specific composition and properties. AC-TEM/STEM and the associated spectroscopic tools emerged as an ideal tool to achieve this. HAADF intensities are useful in identifying the interface between the constituent metals in core-shell particles, for example, the interface between Au and Pd in Au@Pd core-shell nanorods was obtained by calculating the HAADF intensities of the atomic columns [105]. Serpell et al. used AC-STEM to identify the core-shell structure of Au@Pd nanoparticles using the atomic number contrast in HAADF-STEM images [106]. Bhattarai et al. employed a seed-mediated growth method to synthesize Au-Pd core-shell nanocubes and triangular nanoparticles consisting of a few Pd layers up to fully grown morphologies [107]. They investigated the shape evolution of the core-shell nanoparticles from single crystal and singly twinned seeds to final concave nanocubes and triangular plates, respectively, by Cs-corrected HAADF-STEM imaging. Figure 7.28 shows the HAADF-STEM images of the core-shell particle obtained with various amounts of Pd precursor. By using AC-STEM in combination with EDX and EELS spectroscopy, Pd-Au-Pd trilayer has been characterized in Au-Pd nanoparticles [108].

Sanchez et al. observed Pt-Pd core-shell nanoparticles using AC-STEM to identify the constituent elements and the crystal facets [109], whereas S. Khanal et al. observed Pt-Pd core-shell nanoparticles of various shapes, viz., decahedral, octahedral, and triangular plates using HAADF-STEM imaging [110].

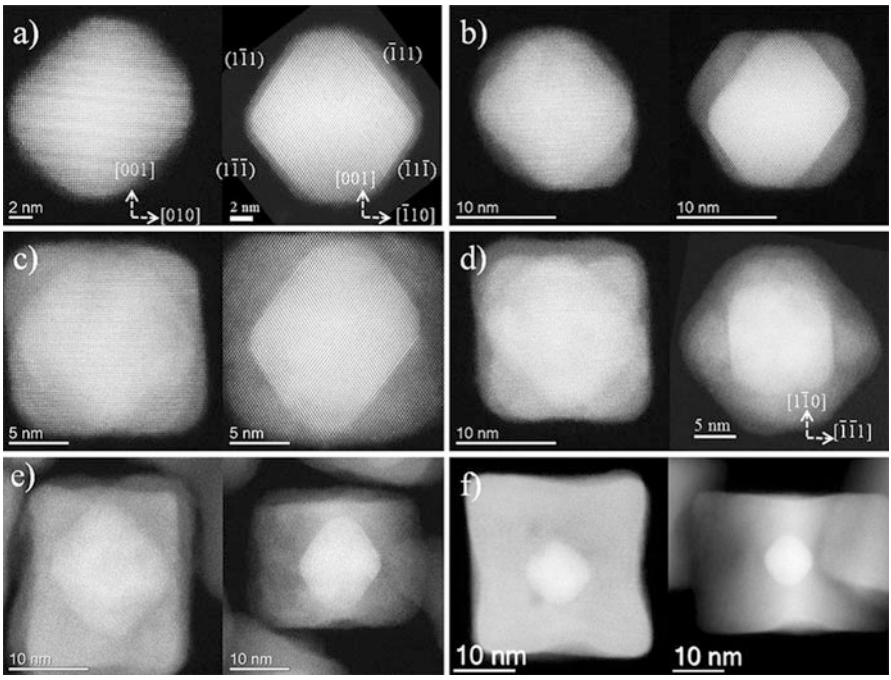

Fig. 7.28 HAADF-STEM images of Au-Pd core-shell with 10 μL (**a**), 20 μL (**b**), 40 μL (**c**), 50 μL (**d**), 75 μL (**e**), and 1 mL (**f**) volume of Pd precursor, respectively, where the growth process can be observed. Frames on the left present nanoparticles in a [100] zone axis, while on the right present nanoparticles in a [110] zone axis, except the right frame in d which is a [112] zone axis. The (111) facets present in [110] zone axis is labeled in right frame of a (Reprinted with permission from Bhattarai et al. [107]. Copyright 2013 Springer)

Obtaining the catalytically active Pt distribution on the surface and thereby decreasing the amount of precious metal in the catalyst have been of great importance in the design of an economically viable Pt-based catalyst. Wang et al. designed Pt-Pd nanoparticles by conformal deposition of platinum as ultrathin shells on facet-controlled palladium icosahedra which exhibited enhanced catalytic performance while reducing its loading (Fig. 7.29) [111]. The platinum overlayers evolve into a corrugated structure under compressive strain on Pd icosahedra. They observed that for Pt-Pd nanocrystals with an average of 2.7 platinum overlayers, their specific and platinum mass activities toward oxygen reduction are enhanced by eight- and sevenfold, respectively, relative to a commercial catalyst.

Another important Pt-based electrocatalyst of commercial interest is PtRu. The presence of Ru in the catalyst has been shown to prevent the catalytic poisoning of Pt by carbon monoxide and thereby improve the efficiency of the catalyst [112]. Hsieh et al. presented an economically viable method for producing well-ordered Ru@Pt NPs, where a bilayer of Pt was present on Ru core. In their study, aberration-corrected STEM imaging was employed to observe ordered structural transition

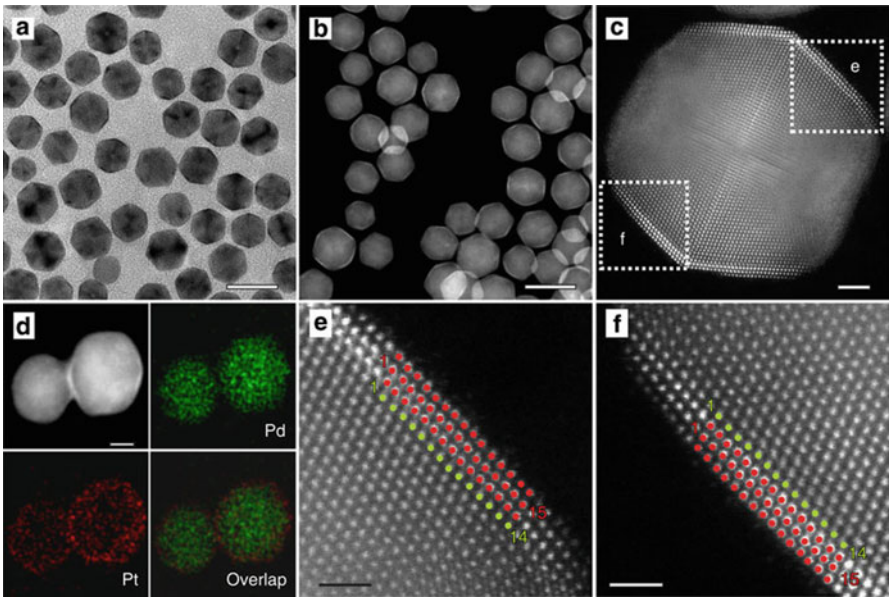

Fig. 7.29 Structural and compositional analyses of the Pd@$Pt_{2.7L}$ icosahedra. (**a**) TEM and (**b**) HAADF-STEM images. Scale bar, 20 nm. (**c**) Atomic-resolution HAADF-STEM image taken from a single particle along a twofold symmetry axis, showing three atomic layers of Pt in the shell (with a brighter contrast) and the Pd atoms in the core. Scale bar, 2 nm. (**d**) HAADF-STEM image of two Pd@$Pt_{2.7L}$ icosahedra and the corresponding energy-dispersive X-ray spectroscopy mapping of Pd and Pt, confirming a core-shell structure. Scale bar, 5 nm. (**e**, **f**) Atomic-resolution HAADF-STEM images taken from the edges marked by boxes in (**c**), revealing the detailed arrangements of Pd and Pt atoms (*green dots*, Pd atoms; *red dots*, Pt atoms). Scale bar, 1 nm (Reprinted with permission from Wang et al. [111])

from ruthenium hcp to platinum fcc stacking sequence at the core-shell interface [113]. Figure 7.30 shows that the lattice spacing of the top two layers is visibly expanded, supporting the presence of Pt shells about two monolayers thick on all facets.

In addition to catalysis, plasmonics is another field of application for bimetallic nanoparticles. Au nanoparticles are the most investigated material in this field. Similar to Au, Cu also exhibits localized surface plasmon resonance. In an attempt to obtain AuCu particle with high-index facets, pentacle gold-copper alloy nanocrystals with fivefold twinning, in which the size can be tuned in the range of 45 to 200 nm, were synthesized in aqueous solution [114]. The growth is found to start from a decahedral core, followed by protrusion of branches along twinning planes. The pentacle nanoalloys obtained display strong localized surface plasmon resonance peaks in the near-infrared region. Figure 7.31 shows the TEM images and EDX elemental maps of pentacle Au-Cu alloy nanocrystal.

Goris et al. employed EDX-STEM tomography to study galvanic replacement of Ag by Au, in Ag nanocube, to obtain Au-Ag nanocages [115]. In their experiment,

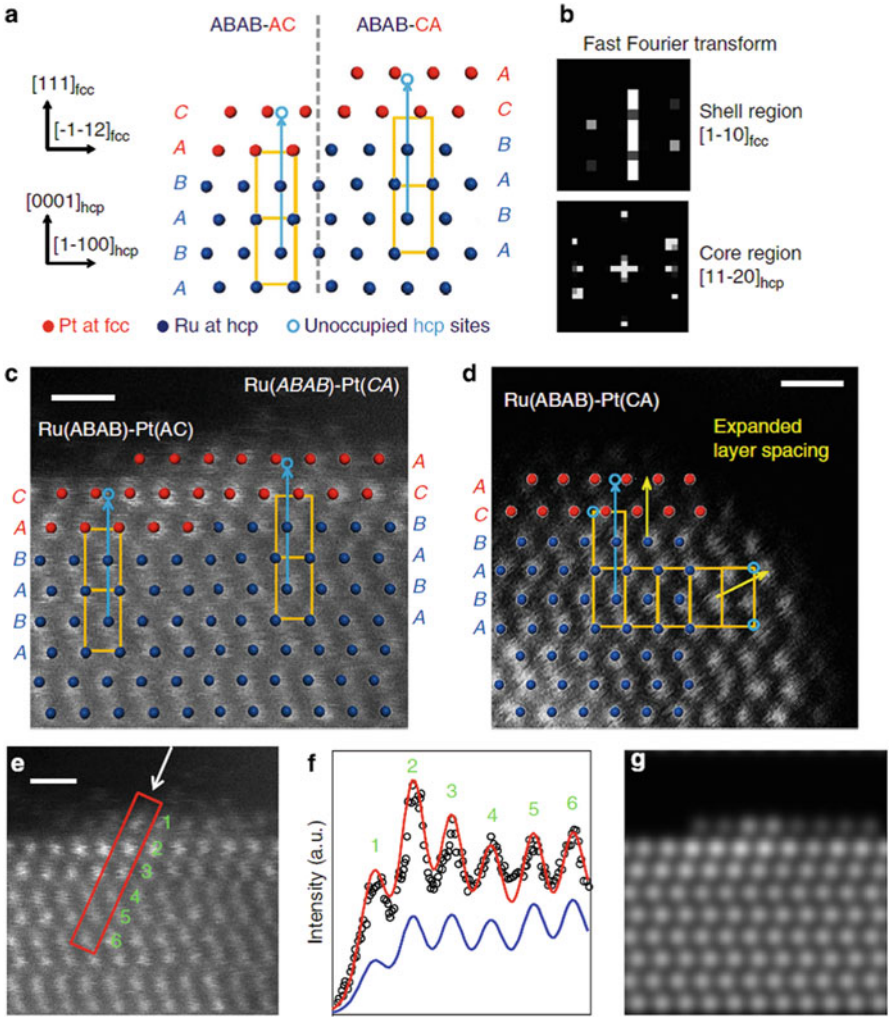

Fig. 7.30 Ordered Ru(hcp)-Pt(fcc) phase transition at core-shell interfaces. (**a**) Orientation of crystallographic planes for the STEM image in c and two DFT (density functional theory)-optimized structural models for close-packed Pt bilayer on an Ru (0001) surface. (**b**) Fast Fourier transform of the image in c. (**c**, **d**) HAADF-STEM images and superimposed DFT-optimized structural models (*red* and *blue* dots). Scale bar, 0.5 nm. The shifts from the hcp to the fcc lattice sites at the top one or two layers are indicated by *yellow* rectangles, *light blue circles*, and *light blue arrows*. The *yellow arrows* in **d** point to the expanded lattice spacing along the surface normal directions. (**e**) The same STEM image as in c for intensity analysis. Scale bar, 0.5 nm. (**f**) Intensity profile along the line indicated by the *arrow* in **e** (*black circles*) with calculated curves using Ru@Pt core-shell (*red line*) and all-Ru (*blue line*) models. (**g**) Calculated STEM image based on the Ru@Pt model (Reprinted with permission from Hsieh et al. [113]. Copyright 2013 Nature Publishing Group)

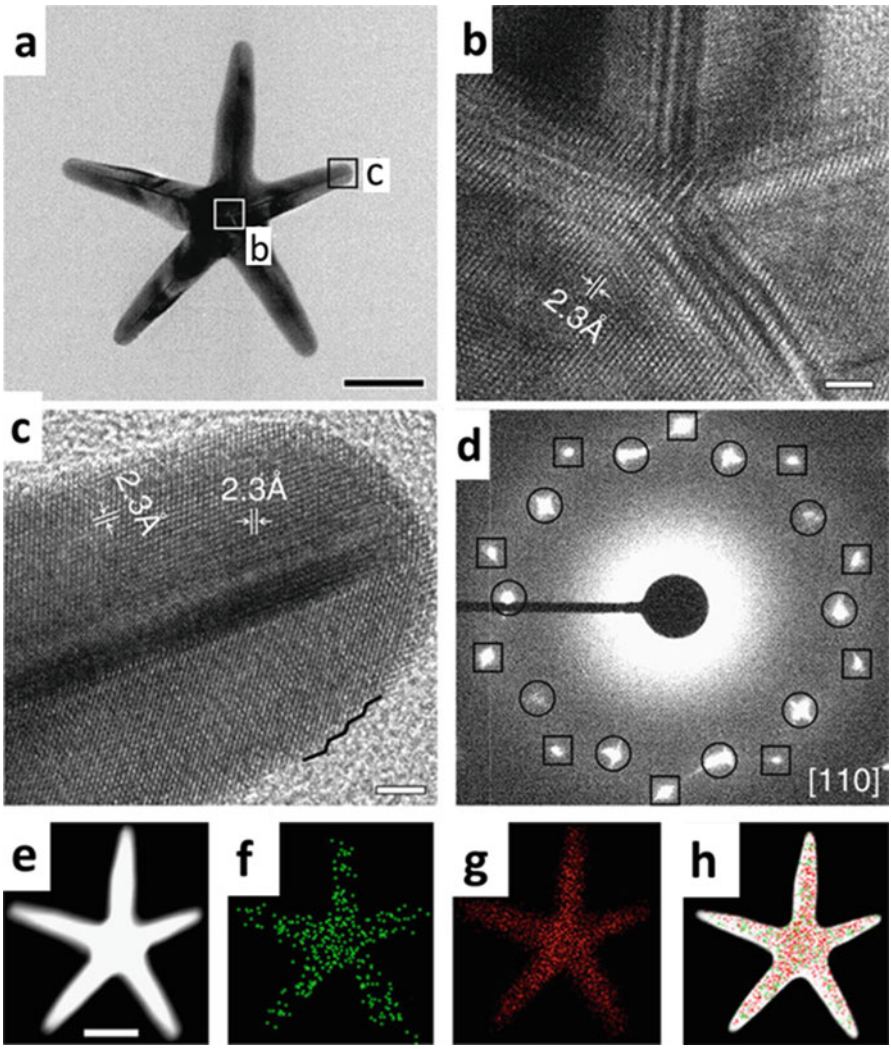

Fig. 7.31 Structure and composition study of pentacle Au-Cu alloy nanocrystals. (**a**) TEM image of an individual pentacle Au-Cu alloy nanocrystal. (**b**, **c**) HRTEM images of the parts marked in a. (**d**) The corresponding selected area electron diffraction pattern with the electron beam directed along the fivefold axis. The circles correspond to electron diffractions from the {111} planes while the boxes correspond to those from the {200} planes. (**e**) STEM image of a typical pentacle nanocrystal. (**f**, **g**) STEM-EDX elemental mapping image of (**f**) Cu and (**g**) Au of an individual pentacle Au-Cu alloy nanocrystal. (**h**) The merged image of e, f, and g. Scale bar, 50 nm (**a**). Scale bar, 2 nm (**b**, **c**). Scale bar, 50 nm in e (Reprinted with permission from He et al. [114]. Copyright Nature Publishing Group)

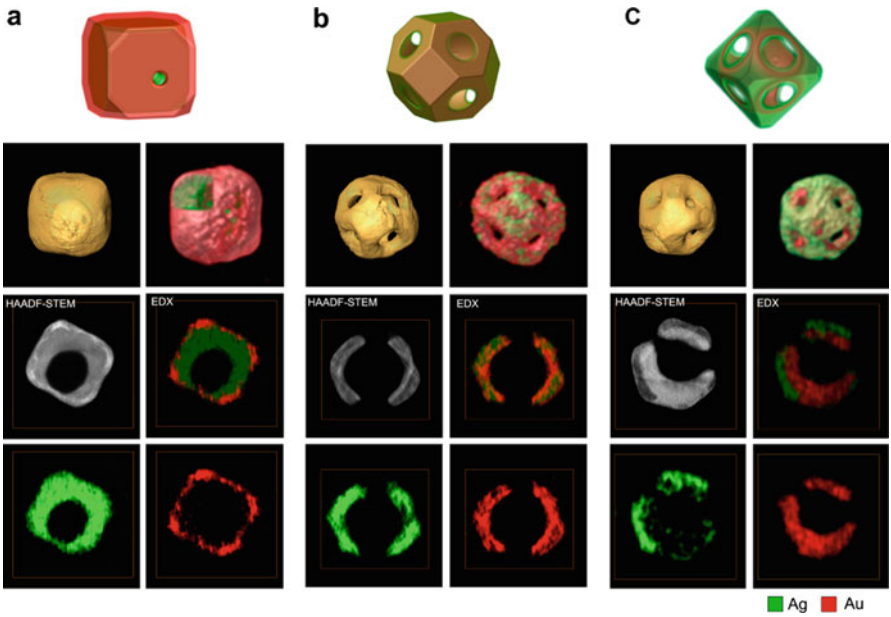

Fig. 7.32 Visualizations of 3D EDX results. For each step in the transformation process with increasing amounts of $HAuCl_4$ (**a**–**c**), volume rendering images viewed along [100] directions are displayed together with 3D rendering of the EDX reconstructions and 3D models (*red* = Au; *green* = Ag). In the visualization of the 3D EDX reconstruction in part a, the Au shell at the top left part of the nanocube is omitted in order to show the presence of Ag at the inner part of the cube. Slices through the different reconstructions are also displayed (Reprinted with permission from Goris et al. [115]. Copyright 2014 American Chemical Society)

single crystalline Ag nanocubes were prepared by using oleylamine as both reducing and capping agent, in an organic solvent, and then the Ag nanocubes colloid obtained was titrated with $HAuCl_4$ solution in toluene at 100 °C to follow the galvanic replacement reaction. Figure 7.32 shows the EDX tomograms at various stages of the transformation. The three-dimensional distribution of Au and Ag is clearly seen in addition to the 3D morphology.

7.5 TEM/STEM Characterization of Trimetallic Nanoparticles

In addition to bimetallic nanoparticles, trimetallic and multimetallic nanoparticles are also synthesized and characterized for various catalytic applications. For example, PtFeNi trimetallic alloy catalyst of chemically ordered $L1_0$-type superlattice structures exhibited enhanced ORR activity and durability [116]. Better ORR activity and improved catalyst stability were achieved for octahedral Pt_2CuNi alloy

nanoparticles with uniform element distribution comparable to that of the state-of-the-art Pt/C [117]. Pd-Ni-Pt core-sandwich-shell NPs have been investigated for electrocatalytic oxidation of methanol and formic acid. Improved performance of the Pd-Ni-Pt particles compared to that of the Pd-Pt control was attributed to the increased compressive strain on the Pt surface [118]. Based on the DFT calculations which predicted that M/CuPd (M = Ag, Au) NPs with 0.8 and 1.2 nm $CuPd_2$ shells have the optimal surface strain and composition for ORR, Guo et al. synthesized monodisperse M/CuPd NPs with 3.1 nm Ag/Au seeds with shell thicknesses controlled at 0.4, 0.75, and 1.1 nm [119]. This was to tune both the shell electronic structure and surface strain to maximize ORR performance. In 0.1 M KOH solution, the $Au/Cu_{40}Pd_{60}$ and $Ag/Cu_{37}Pd_{63}$ catalysts with 0.75 and 1.1 nm shell were observed to be more efficient for ORR than any other M/CuPd catalysts, CuPd NPs, and Ag studied by them. Khanal et al. synthesized AuCu-Pt trimetallic particles with high-index surfaces employing a one pot synthesis [120]. High-index surfaces are non-flat surfaces with high kinks and atomic step density resulting in high reactivity. Therefore they are catalytically more active than the low index surfaces. They obtained AuCu-Pt core-shell penta-twinned structure trimetallic nanoparticles, consisting of a Pt monolayer shell and bimetallic AuCu core. In addition, the introduction of Cu in the core reduces the percentage of precious metal, and the catalytically active Pt present predominantly on the surface will make it a better catalyst. AC-STEM is employed to obtain the structure and composition. Figure 7.33a shows the HAADF-STEM image of the penta-twinned particle. Contrast due to various elements in AuCu core and Pt shell is identified in Fig. 7.33b. FFT (Fig. 7.33c) is used to identify the reflections due to Au, Cu, and Pt.

In another study, Au@Pd@Pt was shown to have enhanced catalytic activity toward methanol oxidation and formic acid oxidation, compared to their bimetallic counterparts [121]. In an attempt to decrease the precious metal in electrocatalysts, Ag-based trimetallic AgPd-Pt has been synthesized and characterized by Khanal et al. [122]. AC-STEM imaging and EDX were used in characterizing the system. Figure 7.34 shows the HAADF-STEM image and EDX elemental maps showing a Pt-rich surface and AgPd core.

7.6 TEM/STEM Characterization of Clusters

Cluster is a finite-sized ensemble of atoms or molecules with sizes from sub-nanometer to few nanometers in diameter, in effect, a bridge between atomic or molecular structure and bulk materials. They have attracted a great deal of attention recently because they exhibit intriguing physical and chemical properties, with a wide range of applications in sensors, medical science, catalysis, magnetic storage, microelectronics, and other areas [123–129]. Nanoclusters can be used as an important scientific tool to tune the properties and improve the utilization of materials, especially in the case of noble metals or rare earth elements. However, the properties of clusters are strongly related to the atomic number-dependent

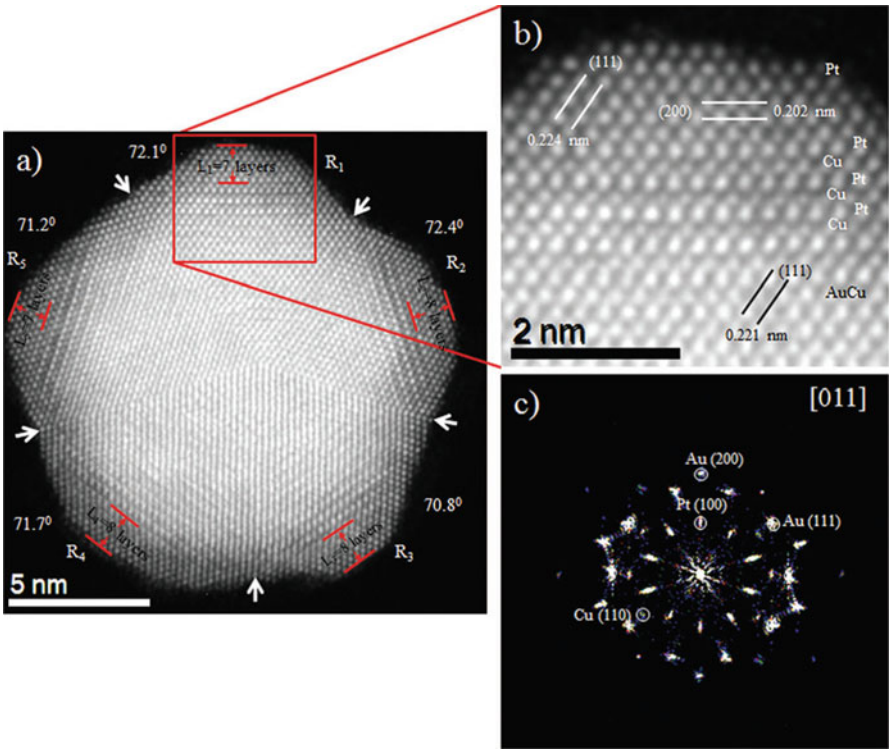

Fig. 7.33 (**a**) Atomic-resolution HAADF-STEM image of a penta-twinned AuCu-Pt core-shell nanoparticle. Each tetrahedron (R1, R2, R3, R4, and R5) is identified by a *white arrow* and the angles measured between the {111} twinning plane are 72.11, 72.41, 70.81, 71.71, and 71.21 as indicated. (**b**) Close-up of the image as indicated by the square showing the crystalline planes and different contrasts of Pt, Cu, and Au lattices is readily observed; (**c**) corresponding fast Fourier transform (FFT) shows the [011] zone axis (Reprinted with permission from Khanal et al. [120]. Copyright 2014 Royal Chemical Society)

structure. To date, many theoretical works have been implemented to predict the three-dimensional atomic structure and magic number (the number of atoms in a cluster of critical size with the higher stability) of various clusters, which is helpful to understand the driving forces or energy favoring particular structures [130–133]. Building the structure-property correlations will help material scientists to design novel nanomaterials with different properties. As mentioned in Sect. 7.2, AC-TEM/STEM with sub-angstrom resolution is a powerful tool to obtain the two-dimensional (2D) structural information of nanoparticles. Recently, by combining the 2D image, density functional theory calculations, and image simulations, the three-dimensional (3D) configurations of clusters can be obtained. In this section, we will discuss the atomic-scale TEM/STEM characterization of atomic clusters, protected clusters, and supported clusters.

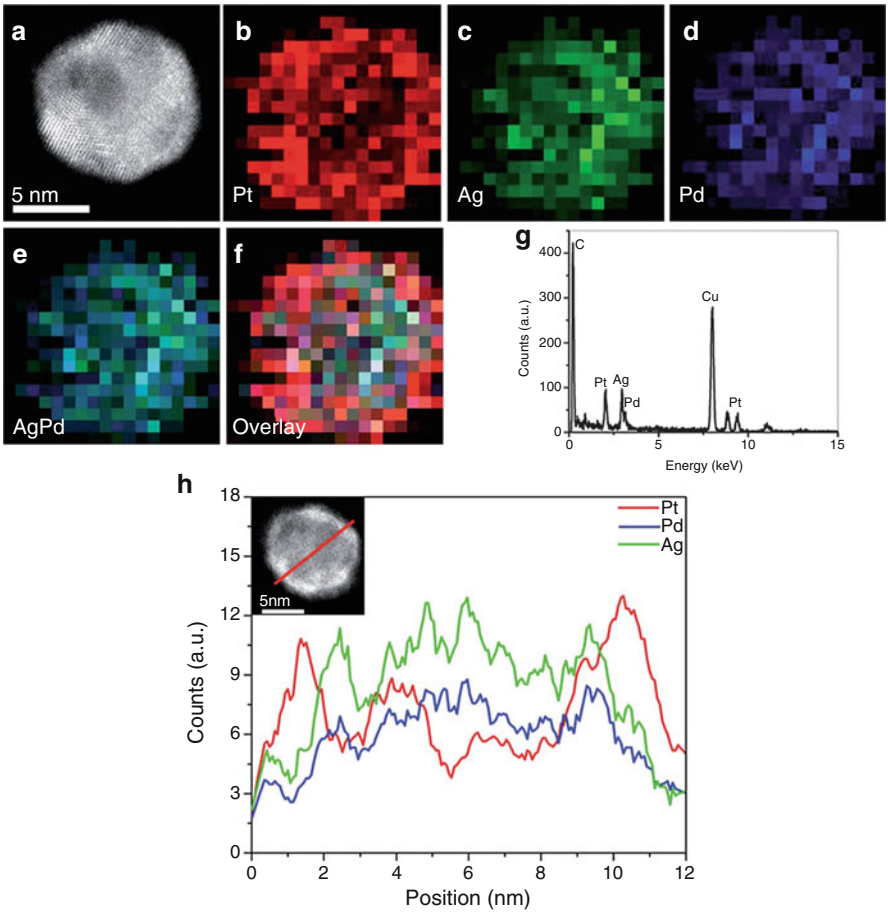

Fig. 7.34 (**a**) HAADF-STEM image of AgPd-Pt multiply twinned nanoparticles; (**b**–**f**) EDX elemental maps of nanoparticles – Pt (L,M), Ag (L), Pd (L), AgPd alloy, and overlay; (**g**) EDX spectrum of corresponding AgPd-Pt multiply twinned nanoparticles; (**h**) Ag, Pd, and Pt elemental profiles along the *red line* across the icosahedral structure (inset of h) (Reprinted with permission from Khanal et al. [122]. Copyright 2013 Royal Chemical Society)

7.6.1 Atomic Clusters

Owing to the unique geometry and electronic structures, metal clusters have emerged as an important nanomaterial that finds applications in catalysis, electronics, molecular sensing, and biology [134]. Experimental and theoretical results have confirmed that the properties are crucially related to the shape and atomic number of metal clusters. Accompanied with the development of aberration-corrected TEM/STEM, many direct atomic-scale observations of metal clusters have been implemented to clarify the atomistic mechanism of shape- and number-dependent

properties in all kinds of clusters, such as platinum (Pt), gold (Au), palladium (Pd), etc. [21, 27, 135, 136]. With the obtained projected images, combined with DFT calculations and image simulations, the three-dimensional structures of clusters can be unraveled [26, 27].

7.6.1.1 STEM Characterization of Metal Clusters

Pt clusters have been widely used as catalysts in the chemical, oil, and automotive industry [137–141]. The Pt clusters on amorphous carbon electrodes in fuel cells are ideal samples for HAADF-STEM characterization due to the difference in Z-contrast between carbon ($Z = 6$) and Pt ($Z = 78$). The catalytic activities depend crucially on the cluster size and degrade if the cluster sizes increase due to coalescence [142, 143]. Figure 7.35 shows a HAADF-STEM image of the Pt clusters obtained with AC-STEM [135]. The lack of regular spacing of the atoms suggests that a Pt cluster has formed. The intensity of each column is different, indicating the different number of atoms stacked at one column.

Au clusters are important catalysts in many chemical reactions. The Au clusters supported on amorphous carbon films show similar contrast with Pt/C. Figure 7.36 shows a sequence of atomic-scale HAADF-STEM images for an ultra-small Au cluster with less than 30 atoms that are performed in the gas phase and soft landed on an amorphous carbon substrate [27]. Under the irradiation of electron beam, the Au cluster shows a geometry transformation from near-square shape to an elongated shape and finally breaks down to smaller fragments or single atoms after a long exposure time due to the accumulation of electron dose. The single bright dots near the Au cluster represent single individual-free gold atoms. This shows that the HAADF-STEM is a powerful tool to identify the structure of nanomaterials, even for the case of single metal atoms. Figure 7.37 shows the HAADF-STEM investigations of Au_{20} clusters [136]. Figure 7.37a–d shows a time-lapse series

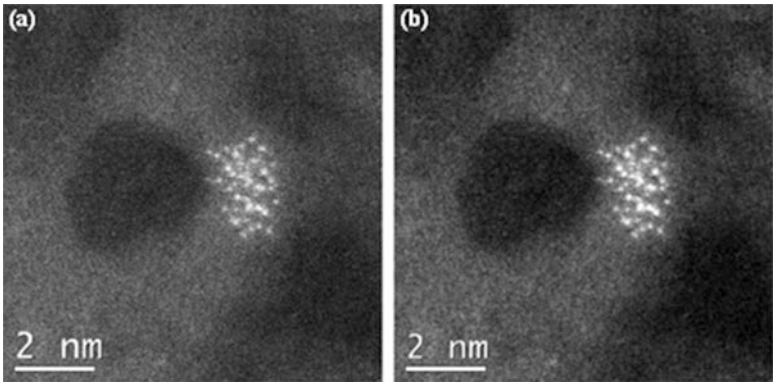

Fig. 7.35 (**a**) Raw HAADF-STEM images of a Pt cluster acquired with a 26.5 mrad aperture. (**b**) HAADF-STEM image from (**a**) after a 3 × 3 low-pass kernel smoothing (Reprinted with permission from Blom et al. [135]. Copyright 2006 Cambridge University Press)

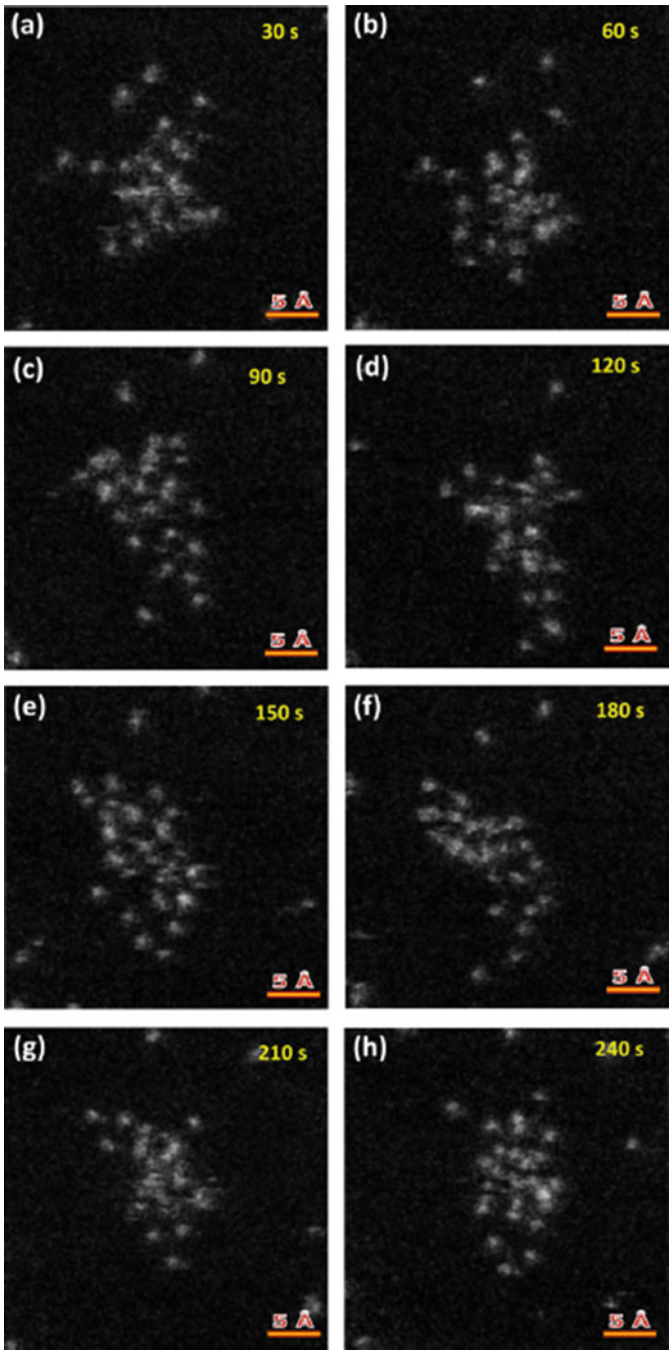

Fig. 7.36 A sequence of HAADF-STEM images for an ultra-small Au cluster with less than 30 atoms on carbon film support (Reprinted with permission from Li et al. [27]. Copyright 2015 AIP Publishing LLC)

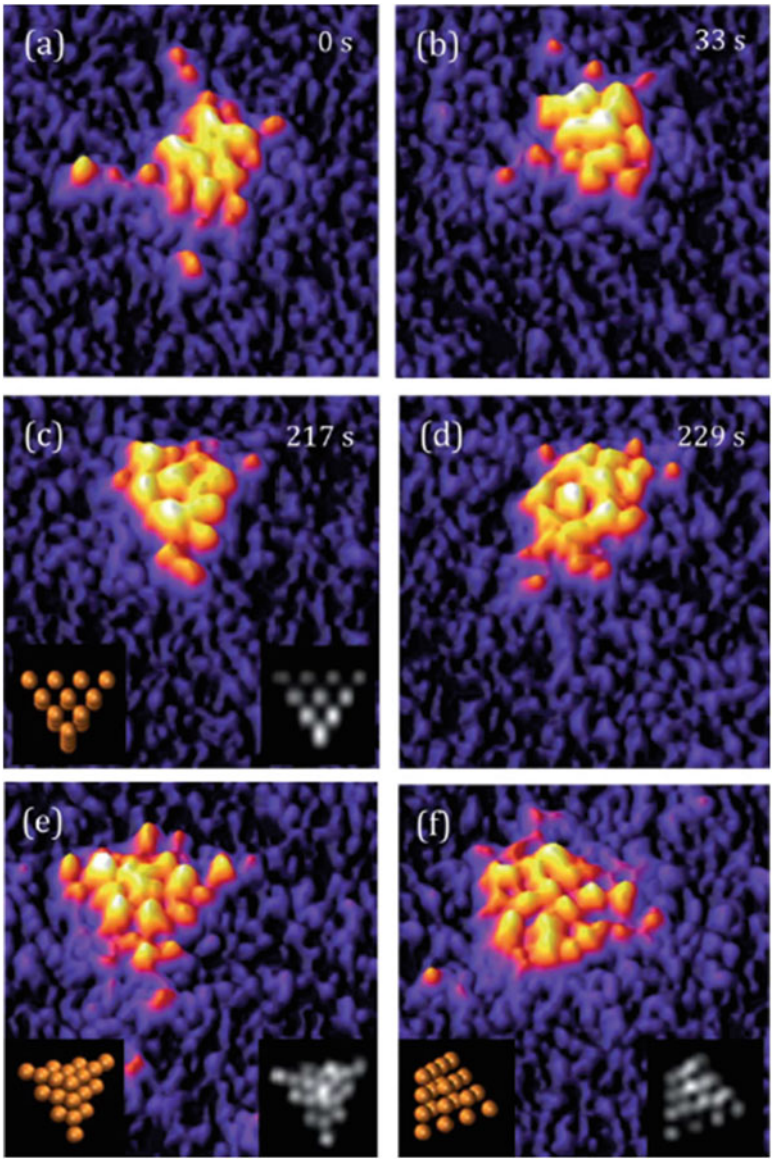

Fig. 7.37 HAADF-STEM investigation of Au_{20} clusters (3D intensity plots). (**a**–**d**) Individual frames from a time-lapse series of HAADF-STEM images of one Au_{20} cluster; (**e** and **f**) images of other Au_{20} clusters. The image size is 2.8 × 2.8 nm for each of (**a**)–(**f**). The insets on the right of (**c**), (**e**), and (**f**) are simulations performed using a Au_{20} FCC tetrahedron model (with orientations shown in the corresponding insets on the *left*) (Reprinted with permission from Wang et al. [136]. Copyright 2012 Royal Chemical Society)

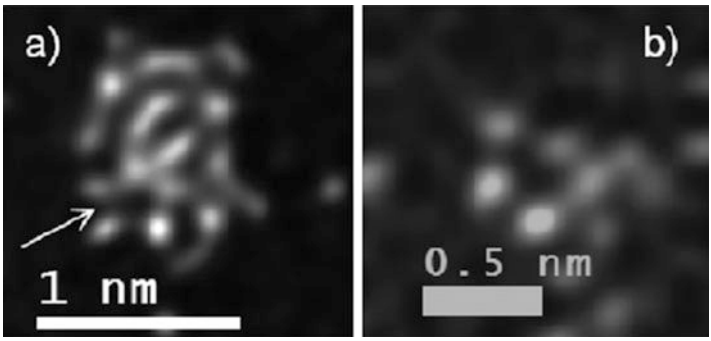

Fig. 7.38 HAADF-STEM images showing pentagonal arrays in Au_n clusters ($n < 20$) (Reprinted with permission from Mayoral et al. [144]. Copyright 2010 Royal Chemical Society)

of HAADF-STEM images. Under irradiation of electron beam, the Au_{20} cluster rotates on the carbon support and also shows an elongated shape after 229 s (Fig. 7.37d). Figure 7.37e–f shows other Au_{20} clusters with different projected orientations. Disordered variants on the high symmetry structures are commonly observed. Figure 7.38 shows atomic-scale HAADF-STEM image of the Au cluster (composed by < 20 atoms) with pentagonal atomic arrays in the structure using an AC-STEM [144]. The direct experimental observation of these kinds of atomic structure and their fluctuation is critical to our understanding of cluster structures and their structure-dependent properties.

7.6.1.2 The Interpretation of Three-Dimensional Structure of Metal Clusters

In order to obtain more structural information, uncovering the 3D structure of clusters is critical to understand structure evolution [145–147]. Based on the 2D-projected HAADF-STEM images of clusters, using an AC-STEM coupled with simple imaging simulation, Li et al. obtained the 3D shape, orientation, and atomic arrangement of gold nanoclusters containing 309 ± 6 atoms on an amorphous carbon substrate, as shown in Fig. 7.39 [21].

Recently by combining HAADF-STEM imaging, DFT calculations, and image simulations, it was possible to determine the 3D structure of Au cluster on amorphous carbon film (Fig. 7.40) [27].

7.6.2 Protected Clusters

As mentioned before, ultra-small nanostructures have a strong trend to combine with each other and reduce their properties. To overcome this, two methods are mainly developed to protect the monodisperse clusters. One method is by inducing

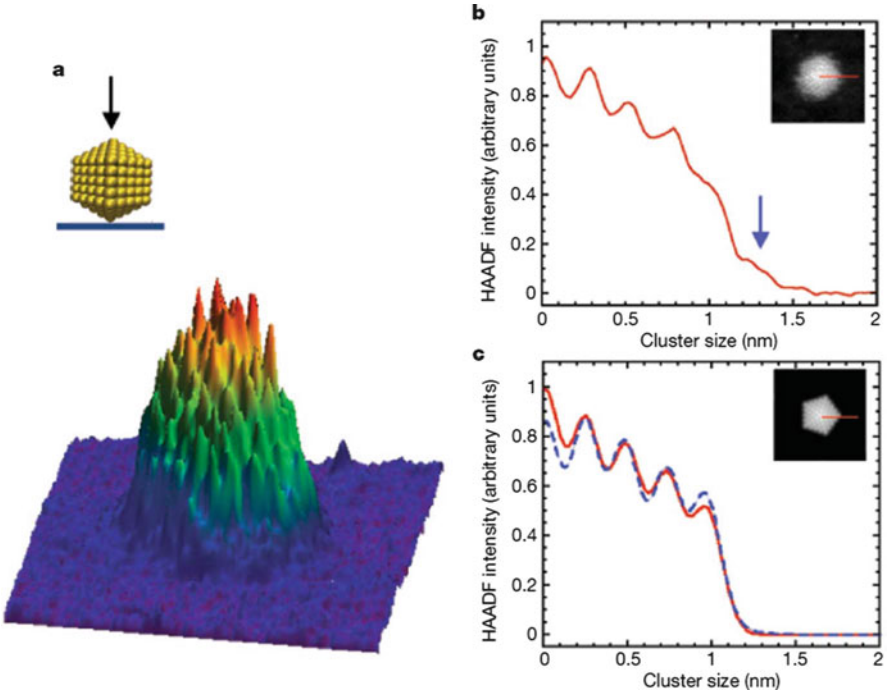

Fig. 7.39 Three-dimensional atomic structure of a gold cluster ($N = 309 \pm 6$). (**a**) Three-dimensional atom density profile of $\sim Au_{309}$, derived from experimental HAADF-STEM image. A hard sphere model for an Ino-decahedral structure is shown with the electron beam (*arrow*) parallel to the fivefold axis. (**b**) Experimental intensity line profile taken from the central atom column of the cluster to one of the corners (indicated in inset with *red line*). (**c**) Simulated HAADF-STEM image (*inset*), obtained with a simple kinematical approach, of an Au_{309} cluster with Ino-decahedral geometry. An intensity profile (*solid curve*) across one ridge (indicated in inset with *red line*) is compared with the result from a full dynamical multislice calculation (*dashed line*) (Reprinted with permission from Li et al. [21]. Copyright 2008 Nature Publishing Group)

capping agents on the surface of the metal clusters [148–150]. Another approach is to confine the metal clusters into nanosized pores or supercages, such as the pore or cages in zeolite and carbon nanotubes [151–153]. In this section, we will introduce the atomic-scale structural characterization of both structures.

7.6.2.1 Metal Clusters Stabilized with Capping Agents

In the synthesis of metal clusters, capping agents can be introduced in the form of free ligands or ligands on metal precursors to form a chemical-protected metal cluster. However, it is still a challenge to uncover the detailed binding structure of the covered metal clusters. Recently, Palmer et al. realized the real-space observation of monolayer hexanethiolate-protected Au_{38} clusters using aberration-

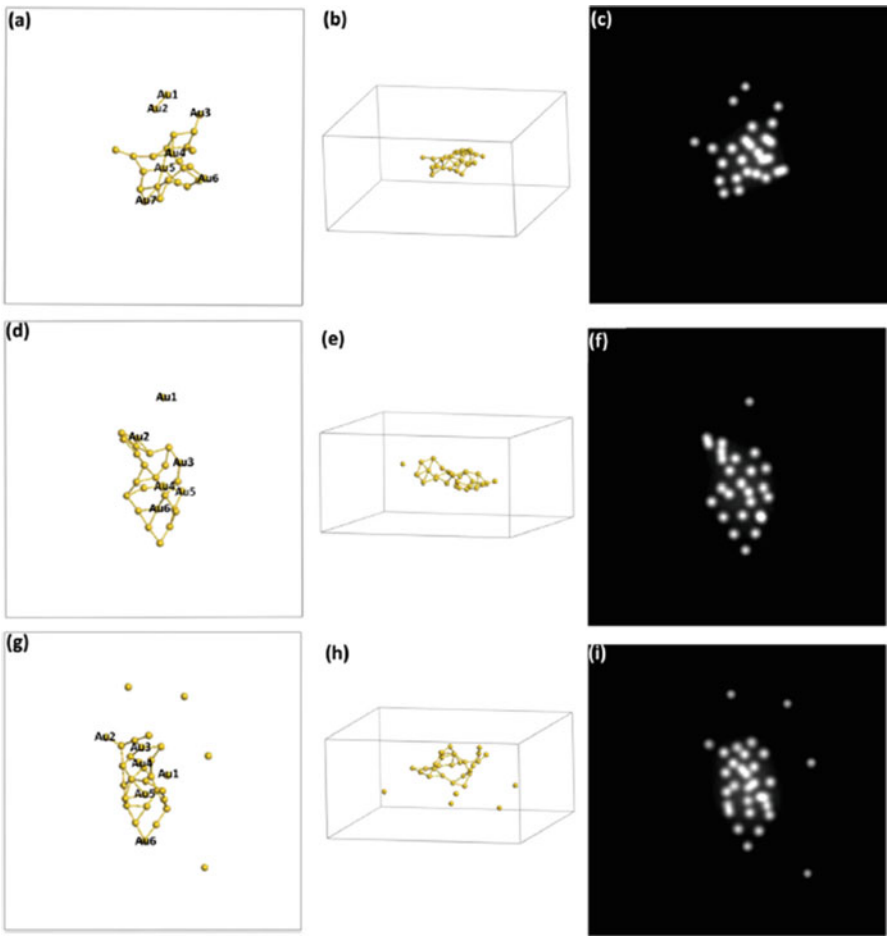

Fig. 7.40 Relaxed 3D geometries viewed from different directions (**a**, **b**; **d**, **e**; **g**, **h**) and the simulated HAADF-STEM images (**c**, **f, i**) of Au clusters. The atomistic models are constructed based upon the experimental images, and a fully structural relaxation is conducted. The HAADF-STEM image simulation (**c**, **f**, **i**) is performed using the relaxed atomic models (Reprinted with permission from Li et al. [27]. Copyright 2015 AIP Publishing LLC)

corrected scanning transmission electron microscopy, as shown in Fig. 7.41 [154]. Based on the series of experimental atomic-scale HAADF-STEM images, the authors make a statistical analysis of the shape population for the monolayer-protected Au_{38} clusters and confirm that a large proportion of Au_{38} clusters show a prolate projected shape, consistent with calculated results. The most important thing is that, in this work, the authors demonstrate that aberration-corrected HAADF-STEM imaging can be successfully applied to resolve the shape of capping agents protecting ultra-small metal clusters. In recent years, many novel organic-protected metal clusters have been developed which show excellent optical, electrical, and

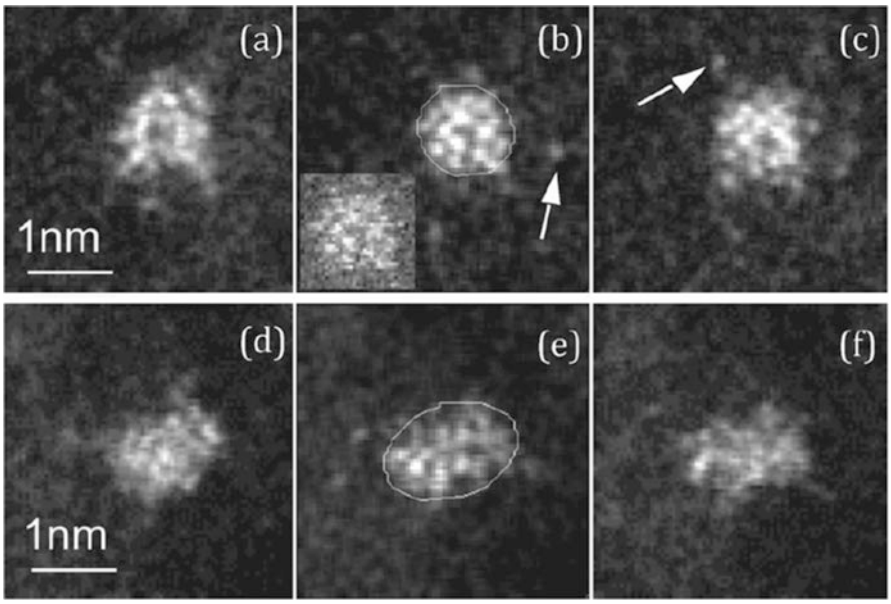

Fig. 7.41 Representative series of HAADF-STEM images (0.2 s per frame) of MP-Au_{38} clusters under optimized imaging conditions. Panels (**a**–**c**) show cluster A, with an approximately circular projected shape; panels (**d**–**f**) show cluster B, with an approximately elliptical projected shape. The insert in (**b**) displays the corresponding raw image. In some cases single Au atoms can be seen around the clusters, as indicated by the *arrows* in (**b**, **c**). Also shown in (**b**, **e**) are the best-fit ellipses used to obtain the aspect ratios (Reprinted with permission from Wang et al. [154]. Copyright 2011 John Wiley and Sons)

catalytic properties. Obtaining the binding structure of protected clusters will help to understand the influence of capping agents on the geometry and properties of metal clusters.

7.6.2.2 Metal Clusters Confined Within Nanopores

To enhance the catalytic activity and recycling stability, zeolite matrix or nanotubes have been employed to restrain the aggregation of metal clusters. The metal clusters can be confined in the channels by ion exchange and wetness impregnation. Figure 7.42 shows atomic-scale HAADF-STEM images and corresponding schematic crystallographic projections of ultra-small palladium (Pd) clusters encapsulated within nanosized silicalite-1 (MFI) zeolite [155]. Most of the Pd clusters show a rodlike morphology in the intersectional void spaces between the straight and sinusoidal channels of the MFI structure. Using AC-STEM, the atomic-scale images of encapsulated Ir_6 and Rh clusters in zeolite were unraveled by Gates et al. [156, 157].

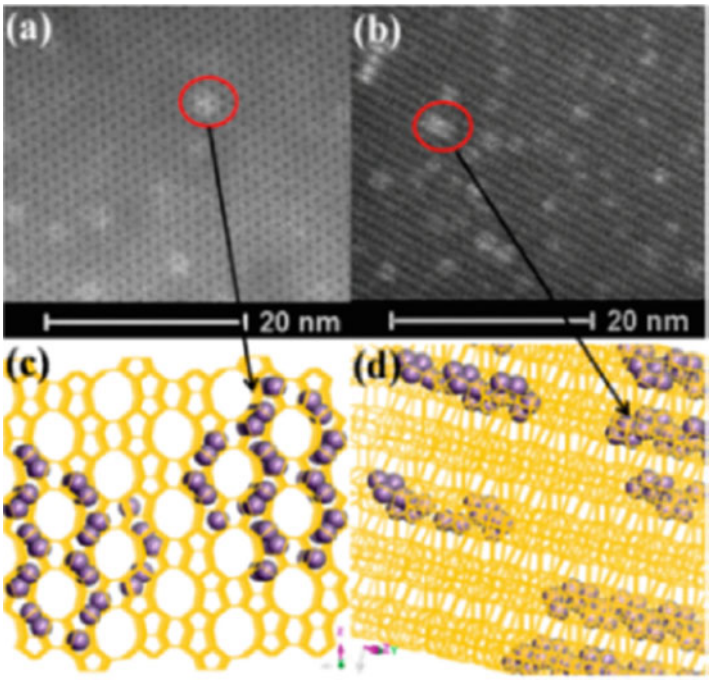

Fig. 7.42 HAADF-STEM images (**a**, **b**) and corresponding schematic crystallographic projections (**c**, **d**) of ultra-small palladium (Pd) clusters encapsulated within nanosized silicalite-1 zeolite (Reprinted with permission from Wang et al. [155]. Copyright 2016 American Chemical Society)

7.6.3 Supported Metal Clusters

Supported metal clusters are of great importance in heterogeneous catalysis [158–160]. Compared with the homogeneous cluster catalysts, the supported clusters show higher performance in the chemical reactions and are easy to separate and recycle. Different types of support materials including oxides (MgO, Al_2O_3, TiO_2, ZrO_2, CeO_2, and so on) and carbon materials (graphene, nanoporous carbon, carbon nanotube, graphite oxide, and so on) have been used for metal clusters for a variety of application [161–167].

7.6.3.1 Oxide-Supported Metal Clusters

To observe the supported metal clusters, MgO and Al_2O_3 are the most commonly used oxide supports because of the smaller atomic numbers of magnesium and aluminum compared with catalytic metal clusters [168, 169]. Figure 7.43 shows the atomic-scale insights into the structural effect of the Al_2O_3-supported Au catalyst using AC-STEM [169]. Based on the images, the reaction site candidates, such as

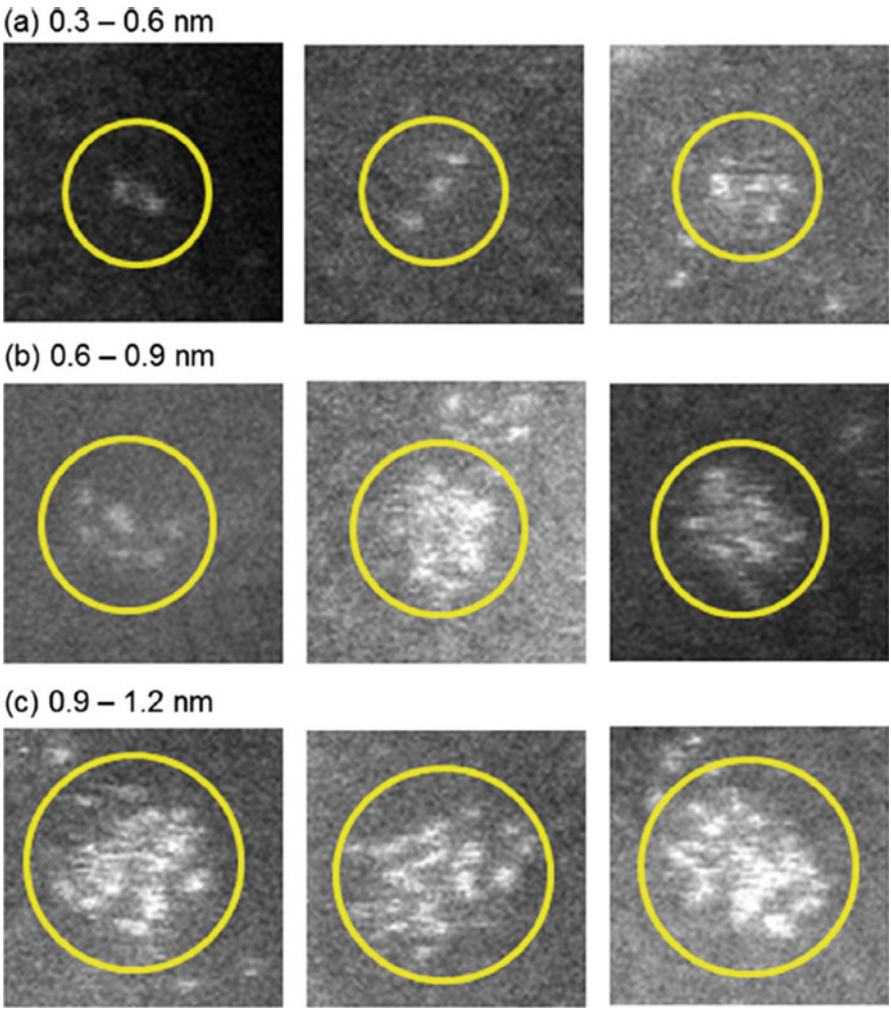

Fig. 7.43 STEM images of Au clusters sized (**a**) 0.3–0.6 nm, (**b**) 0.6–0.9 nm, and (**c**) 0.6–0.9 nm. The white spots are derived from Au atoms. Au clusters are indicated by *yellow circles* (Reprinted with permission from Ohyama et al. [169]. Copyright 2016 Elsevier)

corner, edge, and surface of Au clusters, have been discussed. The results suggested that the corner atoms are key sites for the catalytic activity. Other oxide-supported metal clusters have also been characterized recently, such as the atomic-scale characterization of TiO_2-supported Ir clusters, as shown in Fig. 7.44 [170].

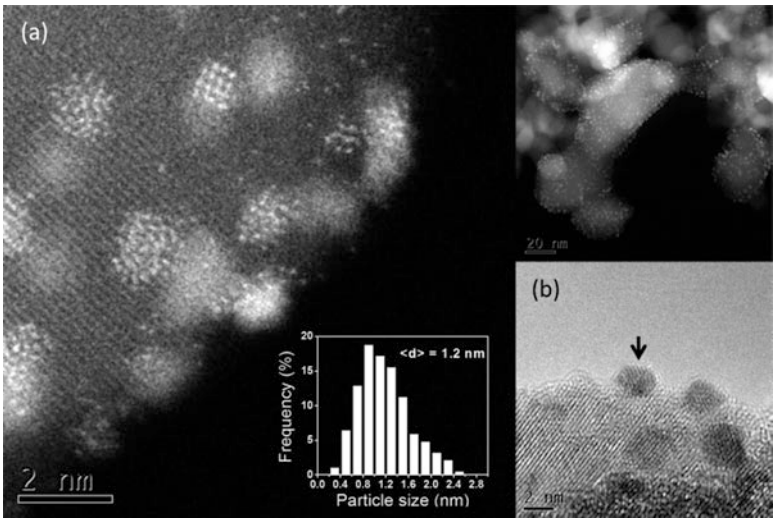

Fig. 7.44 HAADF-STEM image of TiO_2-supported Ir clusters with particle size histogram in the inset (Reprinted with permission from Hernández-Cristóbal et al. [170]. Copyright 2015 American Chemical Society)

7.6.3.2 Metal Clusters Supported on Carbon

Metal clusters supported on carbon materials are another system suitable for the atomic-scale STEM characterization because of the large Z-contrast between the carbon support and the metal clusters. Figure 7.45 shows the atomic-scale HAADF-STEM images of rhenium (Re) clusters of a few atoms and single Re atoms on graphene nanosheets [171]. The atomic structure of the Re clusters can be distinguished very well because of the thin substrate and large Z-contrast between carbon (n = 6) and Re (n = 75). Based on the clear images, combined with DFT calculation and STEM image simulation, the 3D geometry of Re clusters on graphene supports can be obtained clearly. Imaoka et al. observed the 3D structures of a Pt_{19} cluster on graphene [172]. It is worthy to note that a low operation voltage of microscopy (∼80 kV) is needed to characterize the system of carbon-supported metal clusters to prevent the electron beam-induced damage to carbon materials.

7.6.3.3 Supported Bimetallic Clusters

The catalytic performances of supported metal clusters depend not only on their size, shape, and interactions with the support but also on their composition [173, 174]. Utilizing the Z-contrast image, it is possible to distinguish the different compositions in a cluster. Figure 7.46 shows atomic-scale HAADF-STEM images of rhodium-iridium cluster on MgO (110) support [175]. The images show rhodium and iridium atoms in brighter contrast than the magnesium and oxygen columns of the MgO surface. Based on the results of quantification of experiment, combining

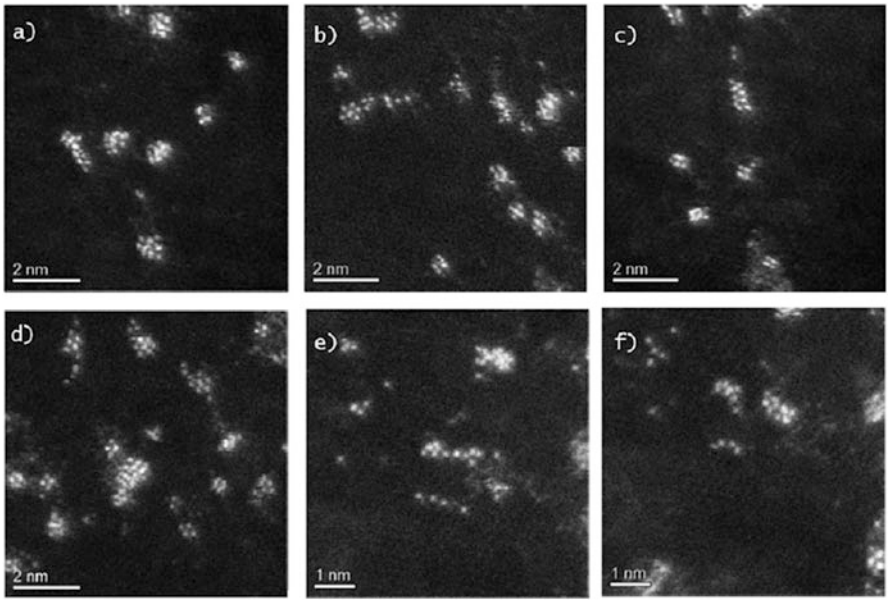

Fig. 7.45 HAADF-STEM images of Re clusters and single Re atoms on graphene nanosheets (Reprinted with permission from Miramontes et al. [171]. Copyright 2015 Royal Chemical Society)

with dynamic multislice image simulation, Ortalan et al. showed a full structure determination of the supported bimetallic clusters.

7.7 In Situ Electron Microscopy

In addition to the abovementioned abilities of TEM/STEM and associated spectroscopic techniques in the characterization of metal nanoparticles and clusters, in situ TEM enables to perform the real-time observation of a specimen's response to external stimuli, such as heat, mechanical forces, etc. In situ electron microscopy dates back to the 1960s when serious problems in materials science, for example, the fatigue of metals for applications in aviation, had to be solved. The need to design spacious experimental setups in the specimen chamber of the electron microscope resulted in the development of high-voltage instruments operating at or above 1 MV and with large gap between the objective pole pieces. The lateral resolution of these machines was hardly below 1 nm, but it was possible to introduce specimen stages with dimensions of several centimeters. Dedicated stages allowed to heat specimens up to high temperatures in the microscope. In such a way, phase transformations were observable, though not on a very small scale. Imaging was in most cases carried out in diffraction contrast (bright or dark field imaging of specimens under Bragg conditions) whereas electron diffraction gave information about the crystallography during transformations of the material. In recent years,

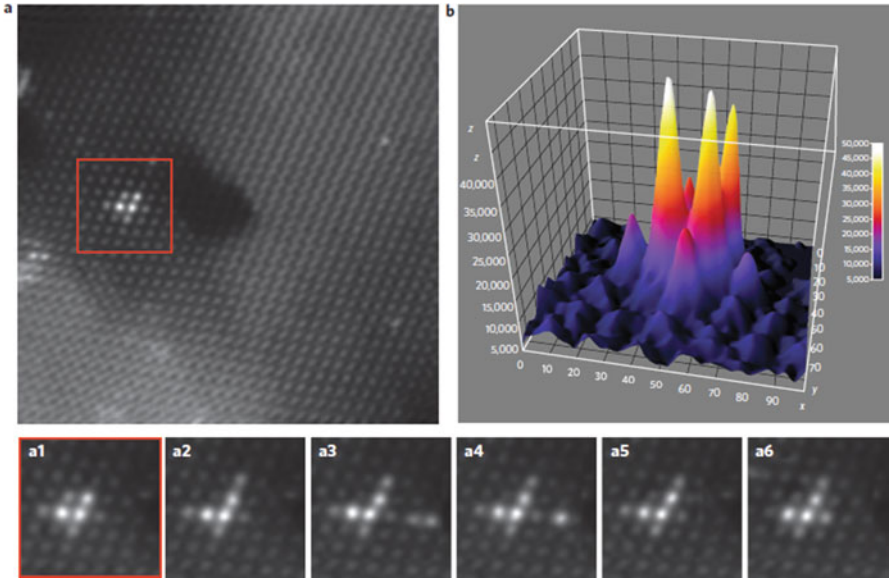

Fig. 7.46 Sequentially taken HAADF-STEM images (**a**, **a1**–**a6**) and intensity surface plot (**b**) of a rhodium-iridium cluster on MgO (110) support. Intensity measurement and quantification were performed using original images (Reprinted with permission from Ortalan et al. [175]. Copyright 2010 Nature Publishing Group)

an increasing number of laboratories have been applying in situ heating (and ultimately gas reaction) techniques in electron microscopy studies of catalysts and other nanophase materials. With the advent of aberration-corrected electron microscopes that provide sub-angstrom image resolution, it is of great interest to study the behavior of materials at elevated temperatures while maintaining the resolution capabilities of the microscope. Recent developments in MEMS-based chips for in situ heating and mechanical testing have resulted in considerable efforts toward such studies on nanomaterials. Thus, development of aberration-corrected optics and MEMS-based chips with small thermal mass facilitates in situ heating experiments with atomic resolution. This enables obtaining a wealth of information of dynamic process that tends to occur as a consequence of elevation of temperature and on the changes occurring at the atomic level. The heating capabilities are possible up to a temperature of 1200 °C while simultaneously maintaining the single-atom imaging capability. This enables improvements in the ability to study, e.g., growth and behavior of bimetallic nanoparticles and the dynamic behavior of interface/alloy/core-shell/multimetallic structures at elevated temperatures [176].

Sintering mechanisms such as coalescence and Ostwald ripening were observed with atomic resolution using in situ TEM. Asoro et al. observed the sintering of Pt nanoparticles at ambient temperature due to the electron beam irradiation [177]. Physical transformations such as hollow structure formation via Kirkendall effect and surface diffusion-assisted methods have also been studied using in situ heating in TEM [178, 179].

Development of dedicated liquid cells materialized the goal to view chemical and physical processes, for example, nucleation and growth of nanomaterials from solution and electrochemical processes in solution with external applied potential [180]. Investigating the structure and properties of materials in their real working environment could provide great insight for their applications. Liquid cells were fabricated using silicon nitride windows, and many modifications were achieved for specific applications such as electrochemical studies, heating, CVD, etc. [181]. High-resolution electron microscopy observation of Pt nanoparticle growth using graphene liquid cells (GLC) was reported by Yuk et al. [182]. The liquid cell was made by encapsulating platinum precursor solution between two laminated graphene layers suspended over holes in a conventional TEM grid. They recorded TEM images at various stages of the growth of Pt nanocrystal where it was observed that the nanocrystals undergo coalescence along the <111> direction giving rise to a single crystalline fcc structure, twinned fcc structure, and also shape evolution in the crystal.

One important field of in situ TEM is catalysis: to observe the catalysts during their operation. Many of the heterogeneous catalysis involve a solid catalyst and gaseous reactants and/or products. There are two main approaches for in situ observation of such catalysts under its working condition. One is the design of in situ gas cells, and the other is the modification of the TEM column to accommodate the gases. In situ gas cells specially designed for this are employed by many research groups. Atomic-resolution in situ TEM studies on barium-promoted ruthenium catalyst for ammonia synthesis were reported in 2001 where they employed an in situ cell for the experiment [183]. Zhang et al. investigated Pd/TiO_2 system in an in situ gas cell experiment where it was observed that the TiO_2 migrated from the support to the surface of Pd particle and underwent further crystallization [184]. During this process of crystallization of overlayers, reconstruction of the underlying Pd nanocrystal facets was observed as a result of surface energy minimization. The reduced oxide was observed to be of one or two atomic layers thick which were dependent on the reactive gas atmosphere obtained by varying H_2 and O_2 partial pressures in a MEMS-based closed TEM gas cell. In addition, reshaping of the metallic surface facets was observed during the process, which is shown in Fig. 7.47. In another study, they have observed the restructuring of Pd-CeO_2 core-shell structures on silicon-functionalized alumina in atmospheric gas cell [185].

The development of environmental transmission electron microscopy (ETEM) has led to the expansion of research in the field of in situ TEM studies of catalysts. In ETEM, a local high pressure is present around the sample while the rest of the region is under high vacuum, which is achieved by differential pumping technology [186]. Aberration-corrected environmental transmission electron microscopy (ETEM) of Au nanoparticles supported on CeO_2 proved that catalytically active gold nanoparticles (AuNPs) move reversibly and stepwise by approximately 0.09 nm on a cerium oxide (CeO_2) support surface at room temperature and in a reaction environment [187]. In their experimental study, Kuwauchi et al. observed that the lateral displacements and rotations occur back and forth between equivalent sites, indicating that AuNPs are loosely bound to oxygen-terminated CeO_2 and may

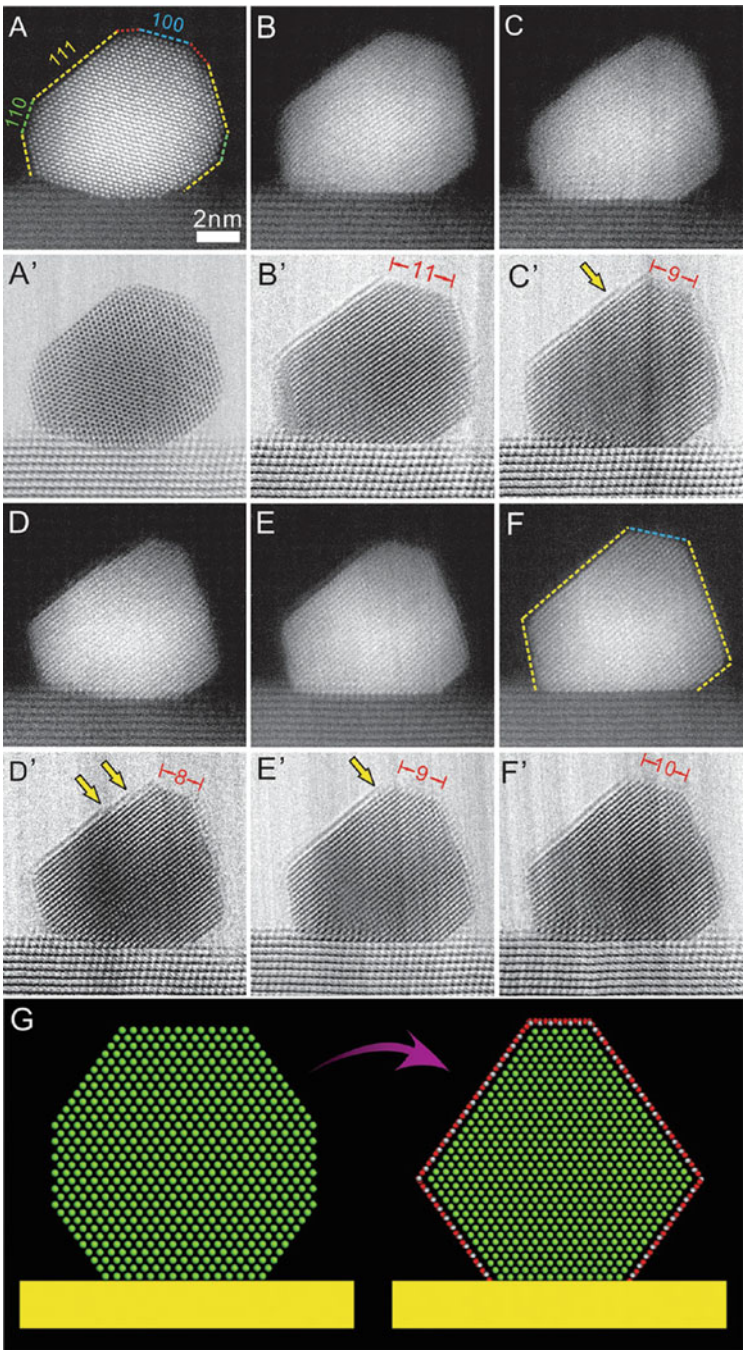

Fig. 7.47 Dynamic shape change of a single Pd nanocrystal supported on TiO_2 during overlayer formation. (**a**–**f**) HAADF and (**a′**–**f′**) corresponding BF-STEM images of Pd/TiO_2 under

migrate on the surface with low activation energy. Their observation suggested that the interfaces between an AuNP and a support which acts as the active site are not structurally rigid.

The technology that is now available for atomic-resolution ETEM includes a Cs corrector and a device to reduce the blur in images that is caused by the coexistence of the chromatic aberration of the objective lens and the energy spread of electrons at the electron source. Monochromators for the electron gun have been used to reduce the energy spread. The possibility of structural analysis in reaction environment is depicted in Fig. 7.48 [188]. Figure 7.48 shows that the combination of Cs corrector and monochromator enables the observation of Au/CeO_2 in 100 Pa of 1 vol% CO/air even at 80 kV. The observation is compared to the image recorded at 200 kV without the Cs corrector to depict the improvement in imaging achieved by the installation of Cs corrector in ETEM facilitating high resolution at low accelerating voltages. Similarly, Boyes et al. modified the electron microscope column to incorporate differential pumping technology [189]. They developed the first double aberration-corrected E(S)TEM which enables single atom imaging during catalytic reaction at high temperature and under catalytic reaction in flowing gas atmosphere.

Li et al. reported an experimental study to understand how heterogeneous catalysts change size, shape, and structure during chemical reactions, by a correlated use of synchrotron X-ray absorption spectroscopy and scanning transmission electron microscopy in operando conditions [190]. The schematic of the experimental setup is shown in Fig. 7.49. In their study, quantitative analysis of the complex structural dynamics of supported Pt catalysts was carried out during catalytic ethylene hydrogenation reaction. They employed a microfabricated catalytic reactor compatible with both the probes. The study showed that the catalysts undergo dynamic restructuring during the reaction over a wide range of length scales, from single atom to larger clusters. The main observation was the fragmentation of the metal clusters in the sub-nm range, preceded by reduction of oxidized metal species present in the fresh sample, followed by the coalescence of the clusters into larger particles.

Dynamic transmission electron microscopy (DTEM) techniques enable the real-time observation of materials processes as they occur in situ within the microscope with the additional feature of high temporal resolution. DTEM aims to capture an image of a reaction or structural change with a single pulse of electrons (~15–1000 ns in duration) and is tuned to investigate irreversible reactions. DTEM uses a short pulse laser to create an electron pulse of the required duration through

Fig. 7.47 (continued) H_2 (4.9 vol %)/O_2 (2 vol %)/Ar 1 atm at 400 °C (**a**), 400 °C for 25 min (**b**), 400 °C for 30 min (**c**), 500 °C for 3 min (**d**), 500 °C for 22 min (**e**), and 500 °C final stable state (**f**). Corresponding surface energy ratios $\gamma_{100}/\gamma_{111}$ are 1.08, 1.24, 1.26, 1.27, 1.31, and 1.27 for A–F, respectively. (**g**) Schematic showing the round-to-faceted shape transformation of the particle. Pd is *green*, O is *red*, and Ti is *gray* (Reprinted with permission from Zhang et al. [184]. Copyright 2016 American Chemical Society)

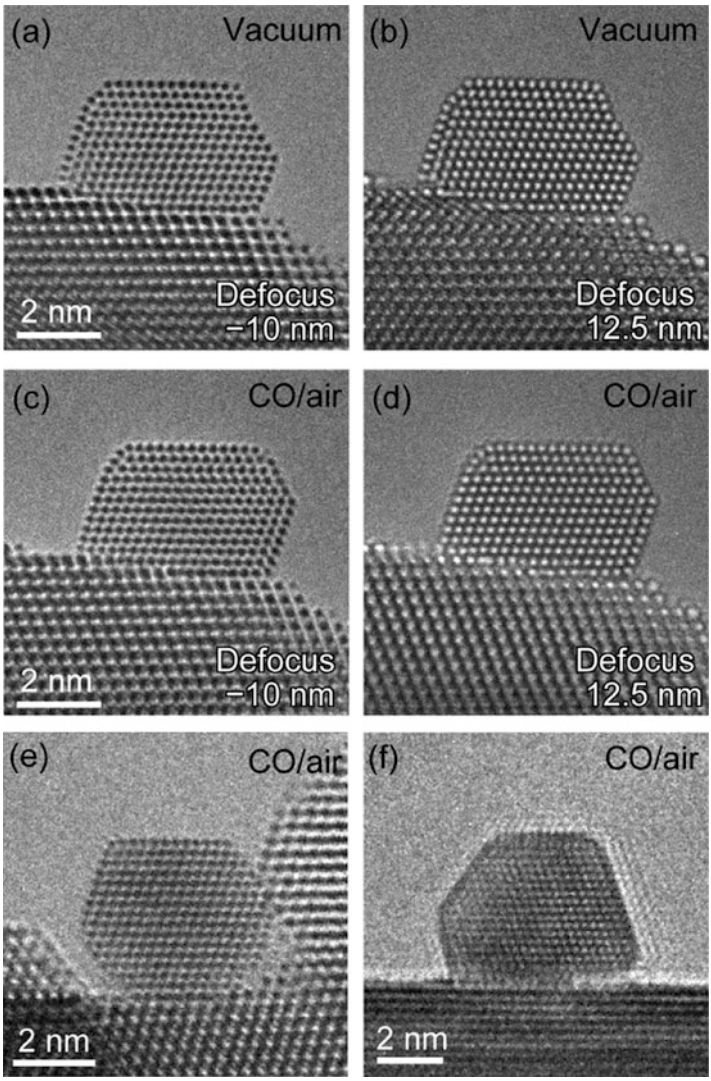

Fig. 7.48 Real catalyst (Au/CeO_2) observed by ETEM with different imaging conditions. (**a**, **b**) are in vacuum; (**c**, **d**) are in 100 Pa of 1 vol% CO/air at room temperature, recorded at 300 kV. (**e**) is at 80 kV with Cs corrector and monochromator, and (**f**) is taken in ETEM at 200 kV without Cs corrector (Reprinted with permission from Takeda et al. [188]. Copyright 2015 Elsevier)

photoemission which contains enough electrons to form a high-resolution image. Martin et al. reported the first dynamic atomic-resolution environmental scanning transmission electron microscope (ESTEM) study of the nanoparticle sintering of a model system of Cu nanoparticles supported on Si_3N_4, C, and Al_2O_3, to understand the mechanism of sintering [191]. They observed that over the course

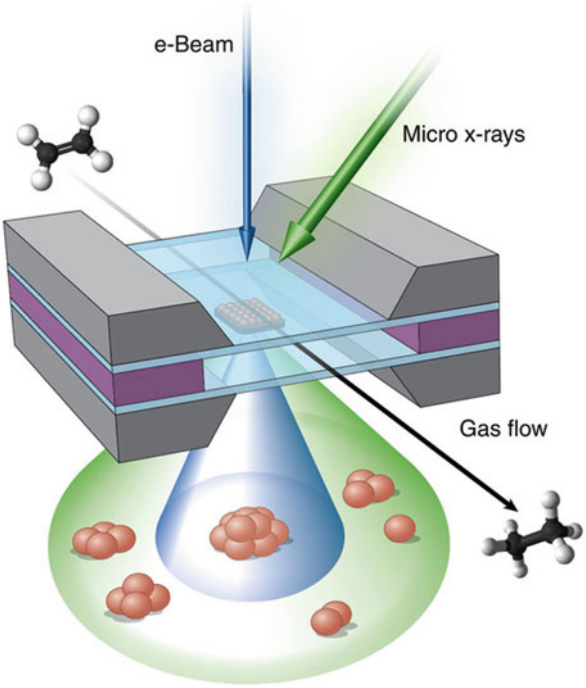

Fig. 7.49 The catalyst is confined between two silicon nitride windows with the reacting gas mixture flowing through the system. *Arrows* show the direction of the electron beam and incident X-ray beam. In the X-ray absorption experiment, all types of Pt species are probed (shown by a *green cone*). In the STEM experiment, only particles larger than ∼1 nm are detectable (shown by a *dark blue cone*) (Reprinted with permission from Li et al. [190])

of the experiment the smaller particles begin to disappear and by the end of the experiment, at 210 min, they are extinct. Also the larger particles grow in size, and the smaller particles shrink while all particles remain immobile relative to each other, confirming the sintering mechanism to be Ostwald ripening (OR). The temperature range of the investigation was 400–550 °C. In addition to the sintering mechanism, they investigated the influence of H_2, temperature, and the support on the Ostwald ripening rate. Significant enhancement in the Ostwald ripening rate of model Cu nanoparticles was observed in the presence of 3 Pa hydrogen, and the effect was independent of the substrates studied.

7.8 Conclusions

In this chapter we describe the electron microscopy techniques employed for the characterization of metal nanoparticles and clusters. The conventional techniques including TEM imaging and diffraction as well as the working principle of STEM imaging are provided. In addition advanced techniques such as holography, tomography, and spectroscopic tomography are also explained. Application of these advanced electron microscopy techniques in the characterization of monometallic nanoparticles and bi-/trimetallic nanoparticles is summarized. Aberration-corrected

STEM acts as an ideal combination to study the bi-/trimetallic nanoparticles as shown with examples from recent literature. The Z-contrast due to different atomic number component elements is a direct evidence to the core-shell structures in many cases. Spectroscopic techniques, EDX and EELS, served as the complimentary techniques by elemental mapping. STEM tomography helped to overcome the drawbacks due to 2D projection imaging, whereas spectroscopic tomographic techniques, EDX tomography and EELS tomography, helped in providing not only morphology but also the elemental composition in three dimensions. Also, aberration-corrected TEM/STEM serves as a tool to study the metal-support interaction in supported metal nanoparticles which is explained with examples. The advances in the field of high-resolution electron microscopy have been of tremendous use for the characterization of metal clusters. The examples from literature show that AC-STEM was frequently employed in comparison to that of AC-TEM in the case of metal clusters. It was particularly useful in imaging clusters of higher atomic number elements on oxides and other supports made of lighter atomic species such as Al_2O_3, MgO, and C. In recent years, the development in the field of in situ holders and dedicated in situ microscopes resulted in the real-time observation of various physical transformations and reactions using an electron microscope. The development in high-temperature MEMS heating holders enables observing materials transformations such as sintering and alloying with atomic resolution. The development of liquid cell leads to the observation of nucleation and growth, self-assembly of colloidal nanoparticles, etc. in real time. The use of gas cells to observe the material under its reaction condition, for example, the catalysts, is also provided. The development of environmental electron microscopes has led to the observation of catalysts under more realistic conditions which was a significant advancement in the field of catalytic research. During in situ TEM experiments, beam-induced effects need to be identified and isolated from the changes due to the experiment to precisely analyze the results in these studies. Thus, advanced electron microscopy and associated techniques have shown to be a powerful tool in the morphological, structural, and compositional characterization of metal nanoparticles and clusters with atomic resolution.

References

1. M. Faraday, The Bakerian lecture: experimental relations of gold (and other metals) to light. Philos. Trans. R. Soc. London **147**, 145 (1857)
2. J. Polte, Fundamental growth principles of colloidal metal nanoparticles – A new perspective. CrystEngComm **17**, 6809 (2015)
3. M. Haruta, T. Kobayashi, H. Sano, N. Yamada, Novel gold catalysts for the oxidation of carbon monoxide at a temperature far below 0°C. Chem. Lett. **16**, 405 (1987)
4. M. Haruta, N. Yamada, T. Kobayashi, S. Iijima, Gold catalysts prepared by coprecipitation for low-temperature oxidation of hydrogen and of carbon monoxide. J. Catal. **115**, 301 (1989)

5. M. Haruta, S. Tsubota, T. Kobayashi, H. Kageyama, M.J. Genet, B. Delmon, Low-temperature oxidation of CO over gold supported on TiO_2, α-Fe_2O_3, and Co_3O_4. J. Catal. **144**, 175 (1993)
6. M. Haruta, Catalysis of gold nanoparticles deposited on metal oxides. CATTECH **6**, 102 (2002)
7. T.V. Choudhary, D.W. Goodman, Oxidation catalysis by supported gold nano-clusters. Top. Catal. **21**, 25 (2002)
8. G. Schmid, B. Corain, Nanoparticulated gold: syntheses, structures, electronics, and reactivities. Eur. J. Inorg. Chem. **2003**, 3081 (2003)
9. K.G. Stamplecoskie, P.V. Kamat, Synergistic effects in the coupling of Plasmon resonance of metal nanoparticles with excited gold clusters. J. Phys. Chem. Lett. **6**, 1870 (2015)
10. C.J. DeSantis, R.G. Weiner, A. Radmilovic, M.M. Bower, S.E. Skrabalak, Seeding bimetallic nanostructures as a new class of plasmonic colloids. J. Phys. Chem. Lett. **4**, 3072 (2013)
11. A. Zaleska-Medynska, M. Marchelek, M. Diak, E. Grabowska, Noble metal-based bimetallic nanoparticles: The effect of the structure on the optical, catalytic and photocatalytic properties. Adv. Colloid Interf. Sci. **229**, 80 (2016)
12. J.H. Sinfelt, Catalysis by alloys and bimetallic clusters. Acc. Chem. Res. **10**, 15 (1977)
13. D. Wang, Y. Li, Bimetallic nanocrystals: Liquid-phase synthesis and catalytic applications. Adv. Mater. **23**, 1044 (2011)
14. J.H. Sinfelt, Ruthenium-copper: A model bimetallic system for studies of surface chemistry and catalysis. Int. Rev. Phys. Chem. **7**, 281 (1988)
15. F. Calvo, Thermodynamics of nanoalloys. Phys. Chem. Chem. Phys. **17**, 27922 (2015)
16. Z.-Y. Zhou, N. Tian, J.-T. Li, I. Broadwell, S.-G. Sun, Nanomaterials of high surface energy with exceptional properties in catalysis and energy storage. Chem. Soc. Rev. **40**, 4167 (2011)
17. F.L. Deepak, A. Mayoral, R.E. Arenal, *Advanced Transmission Electron Microscopy: Applications to Nanomaterials* (Springer, Cham, 2015)
18. C.-J. Liu, U. Burghaus, F. Besenbacher, Z.L. Wang, Preparation and characterization of nanomaterials for sustainable energy production. ACS Nano **4**, 5517 (2010)
19. C.-L. Jia, K.W. Urban, M. Alexe, D. Hesse, I. Vrejoiu, Direct observation of continuous electric dipole rotation in flux-closure domains in ferroelectric Pb (Zr, Ti) O_3. Science **331**, 1420 (2011)
20. Y. Peng, P.D. Nellist, S.J. Pennycook, HAADF-STEM imaging with sub-angstrom probes: A full Bloch wave analysis. J. Electron. Microsc **53**, 257 (2004)
21. Z. Li, N. Young, M. Di Vece, S. Palomba, R. Palmer, A. Bleloch, B. Curley, R. Johnston, J. Jiang, J. Yuan, Three-dimensional atomic-scale structure of size-selected gold nanoclusters. Nature **451**, 46 (2008)
22. J. Biskupek, J.R. Jinschek, U. Wiedwald, M. Bendele, L. Han, P. Ziemann, U. Kaiser, Identification of magnetic properties of few nm sized FePt crystalline particles by characterizing the intrinsic atom order using aberration corrected S/TEM. Ultramicroscopy **110**, 820 (2010)
23. C. Cui, L. Gan, M. Heggen, S. Rudi, P. Strasser, Compositional segregation in shaped Pt alloy nanoparticles and their structural behaviour during electrocatalysis. Nat. Mater. **12**, 765 (2013)
24. A. Mayoral, F.L. Deepak, R. Esparza, G. Casillas, C. Magen, E. Perez-Tijerina, M. Jose-Yacaman, On the structure of bimetallic noble metal nanoparticles as revealed by aberration corrected scanning transmission electron microscopy (STEM). Micron **43**, 557 (2012)
25. L. Kesavan, R. Tiruvalam, M.H. Ab Rahim, M.I. bin Saiman, D.I. Enache, R.L. Jenkins, N. Dimitratos, J.A. Lopez-Sanchez, S.H. Taylor, D.W. Knight, Solvent-free oxidation of primary carbon-hydrogen bonds in toluene using Au-Pd alloy nanoparticles. Science **331**, 195 (2011)
26. S. Bals, S. Van Aert, C. Romero, K. Lauwaet, M.J. Van Bael, B. Schoeters, B. Partoens, E. Yücelen, P. Lievens, G. Van Tendeloo, Atomic scale dynamics of ultrasmall germanium clusters. Nat. Commun. **3**, 897 (2012)
27. J. Li, D. Yin, C. Chen, Q. Li, L. Lin, R. Sun, S. Huang, Z. Wang, Atomic-scale observation of dynamical fluctuation and three-dimensional structure of gold clusters. J. Appl. Phys. **117**, 085303 (2015)

28. Z. Wang, M. Saito, K.P. McKenna, L. Gu, S. Tsukimoto, A.L. Shluger, Y. Ikuhara, Atom-resolved imaging of ordered defect superstructures at individual grain boundaries. Nature **479**, 380 (2011)
29. R. Sun, Z. Wang, M. Saito, N. Shibata, Y. Ikuhara, Atomistic mechanisms of nonstoichiometry-induced twin boundary structural transformation in titanium dioxide. Nat. Commun. **6**, 7120 (2015)
30. A. Azizi, B. Jiang, Z. Lin, A.L. Elias, M. Terrones, N. Alem, Individual Mo Dopant atoms in WS_2 monolayers: atomic structure and induced strain. Microsc. Microanal. **21**, 435 (2015)
31. J. Deng, H. Li, J. Xiao, Y. Tu, D. Deng, H. Yang, H. Tian, J. Li, P. Ren, X. Bao, Triggering the electrocatalytic hydrogen evolution activity of the inert two-dimensional MoS_2 surface via single-atom metal doping. Energy Environ. Sci. **8**, 1594 (2015)
32. R. Ishikawa, A.R. Lupini, S.D. Findlay, T. Taniguchi, S.J. Pennycook, Three-dimensional location of a single dopant with atomic precision by aberration-corrected scanning transmission electron microscopy. Nano Lett. **14**, 1903 (2014)
33. S. Raghavan, J.Y. Zhang, O.F. Shoron, S. Stemmer, Probing the metal-insulator transition in $BaTiO_3$ by electrostatic doping. Phys. Rev. Lett. **117**, 037602 (2016)
34. H. Chang, M. Saito, T. Nagai, Y. Liang, Y. Kawazoe, Z. Wang, H. Wu, K. Kimoto, Y. Ikuhara, Single adatom dynamics at monatomic steps of free-standing few-layer reduced graphene. Sci Rep **4**, 6037 (2014)
35. D.B. Williams, C.B. Carter, *Transmission Electron Microscopy: A Textbook for Materials Science* (Springer, New York, 2009)
36. N. Yoshimura, Introduction of the electron microscope, in *Historical Evolution Toward Achieving Ultrahigh Vacuum in JEOL Electron Microscopes* (Springer, Tokyo, 2014), p. 1
37. J.M. Zuo, J.C. Spence, Lens aberrations and aberration correction, in *Advanced Transmission Electron Microscopy* (Springer, New York, 2017), p. 165
38. M. Haider, S. Uhlemann, E. Schwan, H. Rose, B. Kabius, K. Urban, Electron microscopy image enhanced. Nature **392**, 768 (1998)
39. P. Tiemeijer, M. Bischoff, B. Freitag, C. Kisielowski, Using a monochromator to improve the resolution in TEM to below 0.5 Å. Part II: Application to focal series reconstruction. Ultramicroscopy **118**, 35 (2012)
40. A. Morawiec, J.-J. Fundenberger, E. Bouzy, J.-S. Lecomte, EP–a program for determination of crystallite orientations from TEM Kikuchi and CBED diffraction patterns. J. Appl. Crystallogr. **35**, 287 (2002)
41. N. Browning, M. Chisholm, S. Pennycook, Atomic-resolution chemical analysis using a scanning transmission electron microscope. Nature **444**, 235 (2006)
42. L. Reimer, H. Kohl, *Transmission Electron Microscopy: Physics of Image Formation and Microanalysis* (Springer-Verlag Berlin Heidelberg, 1997)
43. J. Li, J. Shen, Z. Li, X. Li, Z. Sun, Z. Hu, S. Huang, Wet chemical route to the synthesis of kesterite Cu_2ZnSnS_4 nanocrystals and their applications in lithium ion batteries. Mater. Lett. **92**, 330 (2013)
44. J. Gjønnes, *Convergent Beam Electron Diffraction Basic Principles* (Springer, Dordrecht, 1997), p. 65
45. J.C.H. Spence, *High-Resolution Electron Microscopy* (Oxford University Press, Oxford, 2013)
46. C.-L. Jia, M. Lentzen, K. Urban, High-resolution transmission electron microscopy using negative spherical aberration. Microsc. Microanal. **10**, 174 (2004)
47. K.W. Urban, C.-L. Jia, L. Houben, M. Lentzen, S.-B. Mi, K. Tillmann, Negative spherical aberration ultrahigh-resolution imaging in corrected transmission electron microscopy. Philos. Trans. A Math. Phys. Eng. Sci. **367**, 3735 (2009)
48. C. Jia, L. Houben, A. Thust, J. Barthel, On the benefit of the negative-spherical-aberration imaging technique for quantitative HRTEM. Ultramicroscopy **110**, 500 (2010)
49. R. Huang, Y.H. Ikuhara, T. Mizoguchi, S.D. Findlay, A. Kuwabara, C.A. Fisher, H. Moriwake, H. Oki, T. Hirayama, Y. Ikuhara, Oxygen-vacancy ordering at surfaces of lithium manganese (III, IV) oxide spinel nanoparticles. Angew. Chem. Int. Ed. (English) **50**, 3053 (2011)

50. Y. Shao-Horn, L. Croguennec, C. Delmas, E.C. Nelson, M.A. O'Keefe, Atomic resolution of lithium ions in $LiCoO_2$. Nat. Mater. **2**, 464 (2003)
51. R. Ishikawa, E. Okunishi, H. Sawada, Y. Kondo, F. Hosokawa, E. Abe, Direct imaging of hydrogen-atom columns in a crystal by annular bright-field electron microscopy. Nat. Mater. **10**, 278 (2011)
52. L.-M. Lacroix, R. Arenal, G. Viau, Dynamic HAADF-STEM observation of a single-atom chain as the transient state of gold ultrathin nanowire breakdown. J. Am. Chem. Soc. **136**, 13075 (2014)
53. C. Chen, S. Lv, J. Li, Z. Wang, X. Liang, Y. Li, D. Viehland, K. Nakajima, Y. Ikuhara, Two-dimensional electron gas at the Ti-diffused $BiFeO_3/SrTiO_3$ interface. Appl. Phys. Lett. **107**, 031601 (2015)
54. C. Amos, M. Roldan, M. Varela, J. Goodenough, P. Ferreira, Understanding the surface structure of $LiMn_2O_4$ spinel cathodes with aberration-corrected HAADF STEM and EELS. Microsc. Microanal. **21**, 1375 (2015)
55. S. Pennycook, D. Jesson, High-resolution Z-contrast imaging of crystals. Ultramicroscopy **37**, 14 (1991)
56. J. Wall, J. Langmore, M. Isaacson, A. Crewe, Scanning transmission electron microscopy at high resolution. Proc. Natl. Acad. Sci. U. S. A. **71**, 1 (1974)
57. L.D. Francis, J. Rivas, M. José-Yacamán, Understanding the structure of nanocatalysts with high resolution scanning/transmission electron microscopy. IOP Conf. Mater. Sci. Eng **55**, 012005 (2014)
58. S. Pennycook, L. Boatner, Chemically sensitive structure-imaging with a scanning transmission electron microscope. Nature **336**, 565 (1988)
59. R.F. Egerton, *Electron Energy-Loss Spectroscopy in the Electron Microscope* (Springer, US, 2011)
60. B. Schaffer, W. Grogger, G. Kothleitner, F. Hofer, Comparison of EFTEM and STEM EELS plasmon imaging of gold nanoparticles in a monochromated TEM. Ultramicroscopy **110**, 1087 (2010)
61. J. Nelayah, L. Gu, W. Sigle, C.T. Koch, I. Pastoriza-Santos, L.M. Liz-Marzán, P.A. van Aken, Direct imaging of surface plasmon resonances on single triangular silver nanoprisms at optical wavelength using low-loss EFTEM imaging. Opt. Lett. **34**, 1003 (2009)
62. C. Diaz-Egea, R. Abargues, J.P. Martínez-Pastor, W. Sigle, P.A. van Aken, S.I. Molina, High spatial resolution mapping of individual and collective localized surface plasmon resonance modes of silver nanoparticle aggregates: Correlation to optical measurements. Nanoscale Res. Lett. **10**, 310 (2015)
63. P. Bayle-Guillemaud, G. Radtke, M. Sennour, Electron spectroscopy imaging to study ELNES at a nanoscale. J. Microsc. **210**, 66 (2002)
64. W. Grogger, M. Varela, R. Ristau, B. Schaffer, F. Hofer, K.M. Krishnan, Energy-filtering transmission electron microscopy on the nanometer length scale. J. Electron Spectrosc. Relat. Phenom. **143**, 139 (2005)
65. B.D. Forbes, L. Houben, J. Mayer, R.E. Dunin-Borkowski, L.J. Allen, Elemental mapping in achromatic atomic-resolution energy-filtered transmission electron microscopy. Ultramicroscopy **147**, 98 (2014)
66. K.W. Urban, J. Mayer, J.R. Jinschek, M.J. Neish, N.R. Lugg, L.J. Allen, Achromatic elemental mapping beyond the nanoscale in the transmission electron microscope. Phys. Rev. Lett. **110**, 185507 (2013)
67. B. Zhang, D.S. Su, Electron tomography: three-dimensional imaging of real crystal structures at atomic resolution. Angew. Chem. Int. Ed. (English) **52**, 8504 (2013)
68. P.A. Midgley, R.E. Dunin-Borkowski, Electron tomography and holography in materials science. Nat. Mater. **8**, 271 (2009)
69. M. Duchamp, A. Ramar, A. Kovács, T. Kasama, F.-J. Haug, S.B. Newcomb, C. Ballif, R.E. Dunin-Borkowski, Conventional and 360 degree electron tomography of a micro-crystalline silicon solar cell. J. Phys. Conf. Ser. **326**, 012057 (2011)

70. J. Garcia-Martinez, C. Xiao, K.A. Cychosz, K. Li, W. Wan, X. Zou, M. Thommes, Evidence of Intracrystalline mesostructured porosity in zeolites by advanced gas sorption, electron tomography and rotation electron diffraction. ChemCatChem **6**, 3110 (2014)
71. M. Bárcena, A.J. Koster, Electron tomography in life science. Semin. Cell Dev. Biol. **220**, 920 (2009)
72. H. Jinnai, R.J. Spontak, Transmission electron microtomography in polymer research. Polymer **50**, 1067 (2009)
73. D.S. Su, B. Zhang, R. Schlögl, Electron microscopy of solid catalysts—Transforming from a challenge to a toolbox. Chem. Rev. **115**, 2818 (2015)
74. N.Y. Jin-Phillipp, C.T. Koch, P.A. van Aken, 3D elemental mapping in nanomaterials by core-loss EFTEM tomography. Microsc. Microanal. **16**, 1842 (2010)
75. P.A. Midgley, M. Weyland, 3D electron microscopy in the physical sciences: the development of Z-contrast and EFTEM tomography. Ultramicroscopy **96**, 413 (*2003*)
76. M. Weyland, P.A. Midgley, Extending energy-filtered transmission electron microscopy (EFTEM) into three dimensions using electron tomography. Microsc. Microanal. **9**, 542 (2003)
77. O. Nicoletti, F. de la Pena, R.K. Leary, D.J. Holland, C. Ducati, P.A. Midgley, Three-dimensional imaging of localized surface plasmon resonances of metal nanoparticles. Nature **502**, 80 (2013)
78. L.K. Arda Genc, G. Meng, H. Cheng, P. Plachinda, L. Pullan, B. Freitag, C. Wang, XEDS STEM tomography for 3D chemical characterization of nanoscale particles. Ultramicroscopy **131**, 24 (2013)
79. P. Burdet, Z. Saghi, A.N.A.N. Filippin, A. Borrás, P.A. Midgley, A novel 3D absorption correction method for quantitative EDX-STEM tomography. Ultramicroscopy **160**, 118 (2016)
80. K. Lepinaya, F. Loruta, R. Pantela, T. Epicierb, Chemical 3D tomography of 28 nm high K metal gate transistor: STEM XEDS experimental method and results. Micron **47**, 43 (2013)
81. S. Iravani, H. Korbekandi, S.V. Mirmohammadi, B. Zolfaghari, Synthesis of silver nanoparticles: Chemical, physical and biological methods. Res. Pharm. Sci. **9**, 385 (2014)
82. A. Brandi, S. Caporali, S. Cicchi, L. Lascialfari, M. Muniz-Miranda, S. Orazzini, M. Severi, F.L. Deepak, E. Giorgetti, in *Stable Ruthenium Colloids by Laser Ablation*. IEEE 15th International Conference on Nanotechnology (IEEE-NANO), 2015, p. 992
83. A. Halder, N. Ravishankar, Ultrafine single-crystalline gold nanowire arrays by oriented attachment. Adv. Mater. **19**, 1854 (2007)
84. A. Gole, C.J. Murphy, Seed-mediated synthesis of gold Nanorods: Role of the size and nature of the seed. Chem. Mater. **16**, 3633 (2004)
85. B.K. Park, S. Jeong, D. Kim, J. Moon, S. Lim, J.S. Kim, Synthesis and size control of monodisperse copper nanoparticles by polyol method. J. Colloid Interface Sci. **311**, 417 (2007)
86. K.J. Carroll, J.U. Reveles, M.D. Shultz, S.N. Khanna, E.E. Carpenter, Preparation of elemental Cu and Ni nanoparticles by the Polyol method: An experimental and theoretical approach. J. Phys. Chem. C **115**, 2656 (2011)
87. M.R. Langille, M.L. Personick, J. Zhang, C.A. Mirkin, Defining rules for the shape evolution of gold nanoparticles. J. Am. Chem. Soc. **134**, 14542 (2012)
88. S. Zhou, J. Li, K.D. Gilroy, J. Tao, C. Zhu, X. Yang, X. Sun, Y. Xia, Facile synthesis of silver Nanocubes with sharp corners and edges in an aqueous solution. ACS Nano **10**, 9861 (2016)
89. J. Zhang, C. Feng, Y. Deng, L. Liu, Y. Wu, B. Shen, C. Zhong, W. Hu, Shape-controlled synthesis of palladium single-crystalline nanoparticles: The effect of HCl oxidative etching and facet-dependent catalytic properties. Chem. Mater. **26**, 1213 (2014)
90. Y. Wang, H.-C. Peng, J. Liu, C.Z. Huang, Y. Xia, Use of reduction rate as a quantitative knob for controlling the twin structure and shape of palladium nanocrystals. Nano Lett. **15**, 1445 (2015)
91. Y. Kang, J.B. Pyo, X. Ye, R.E. Diaz, T.R. Gordon, E.A. Stach, C.B. Murray, Shape-controlled synthesis of Pt nanocrystals: The role of metal carbonyls. ACS Nano **7**, 645 (2013)

92. M.J. Hÿch, L. Potez, Geometric phase analysis of high-resolution electron microscopy images of antiphase domains: Example Cu_3Au. Philos. Mag. A **76**, 1119 (1997)
93. C.L. Johnson, E. Snoeck, M. Ezcurdia, B. Rodriguez-Gonzalez, I. Pastoriza-Santos, L.M. Liz-Marzan, M.J. Hytch, Effects of elastic anisotropy on strain distributions in decahedral gold nanoparticles. Nat. Mater. **7**, 120 (2008)
94. J. Cantu-Valle, F. Ruiz-Zepeda, E. Voelkl, M. Kawasaki, U. Santiago, M. José-Yacaman, A. Ponce, Determination of the surface morphology of gold-decahedra nanoparticles using an off-axis electron holography dual-lens imaging system. Micron **54–55**, 82 (2013)
95. B. Goris, S. Bals, W. Van den Broek, E. Carbó-Argibay, S. Gómez-Graña, L.M. Liz-Marzán, G. Van Tendeloo, Atomic-scale determination of surface facets in gold nanorods. Nat. Mater. **11**, 930 (2012)
96. M. José-Yacamán, A. Ponce, S. Mejía-Rosales, F.L. Deepak, Advanced methods of electron microscopy in catalysis research, in *Advances in Imaging and Electron Physics*, ed. by W.H. Peter (Elsevier, Amsterdam, 2013), p. 279
97. Y. Han, R. Ferrando, Z.Y. Li, Atomic details of interfacial interaction in gold nanoparticles supported on MgO(001). J. Phys. Chem. Lett. **5**, 131 (2014)
98. J.A. Lopez-Sanchez, N. Dimitratos, C. Hammond, G.L. Brett, L. Kesavan, S. White, P. Miedziak, R. Tiruvalam, R.L. Jenkins, A.F. Carley, D. Knight, C.J. Kiely, G.J. Hutchings, Facile removal of stabilizer-ligands from supported gold nanoparticles. Nat. Chem. **3**, 551 (2011)
99. Y. Lin, Z. Wu, J. Wen, K. Ding, X. Yang, K.R. Poeppelmeier, L.D. Marks, Adhesion and atomic structures of gold on ceria nanostructures: The role of surface structure and oxidation state of ceria supports. Nano Lett. **15**, 5375 (2015)
100. M.G. Panthani, C.M. Hessel, D. Reid, G. Casillas, M. José-Yacamán, B.A. Korgel, Graphene-supported high-resolution TEM and STEM imaging of silicon nanocrystals and their capping ligands. J. Phys. Chem. C **116**, 22463 (2012)
101. P. Kundu, H. Heidari, S. Bals, N. Ravishankar, G. Van Tendeloo, Formation and thermal stability of gold–silica nanohybrids: Insight into the mechanism and morphology by electron tomography. Angew. Chem. Int. Ed. (English) **53**, 3970 (2014)
102. Y. Soni, E.A. Anumol, N. Chandrani, F.L. Deepak, C.P. Vinod, A convenient route for Au@Ti-SiO_2 nanocatalyst synthesis and its application for room temperature CO oxidation. J. Phys. Chem. C **121**, 4946 (2017)
103. A. Ruditskiy, H.-C. Peng, Y. Xia, Shape-controlled metal nanocrystals for heterogeneous catalysis. Annu. Rev. Chem. Biomol. Eng. **7**, 327 (2016)
104. C. Cui, L. Gan, H.-H. Li, S.-H. Yu, M. Heggen, P. Strasser, Octahedral PtNi nanoparticle catalysts: Exceptional oxygen reduction activity by tuning the alloy particle surface composition. Nano Lett. **12**, 5885 (2012)
105. R.L. Chantry, I. Atanasov, W. Siriwatcharapiboon, B.P. Khanal, E.R. Zubarev, S.L. Horswell, R.L. Johnston, Z.Y. Li, An atomistic view of the interfacial structures of AuRh and AuPd nanorods. Nanoscale **5**, 7452 (2013)
106. C.J. Serpell, J. Cookson, D. Ozkaya, P.D. Beer, Core@shell bimetallic nanoparticle synthesis via anion coordination. Nat. Chem. **3**, 478 (2011)
107. N. Bhattarai, G. Casillas, S. Khanal, J.J.V. Salazar, A. Ponce, M. Jose-Yacaman, Origin and shape evolution of core–shell nanoparticles in Au–Pd: From few atoms to high Miller index facets. J. Nanopart. Res. **15**, 1660 (2013)
108. F.L. Deepak, G. Casillas-Garcia, R. Esparza, H. Barron, M. Jose-Yacaman, New insights into the structure of Pd–Au nanoparticles as revealed by aberration-corrected STEM. J. Cryst. Growth **325**, 60 (2011)
109. S.I. Sanchez, M.W. Small, J.-m. Zuo, R.G. Nuzzo, Structural characterization of Pt−Pd and Pd−Pt core−shell nanoclusters at atomic resolution. J. Am. Chem. Soc. **131**, 8683 (2009)
110. S. Khanal, G. Casillas, J.J. Velazquez-Salazar, A. Ponce, M. Jose-Yacaman, Atomic resolution imaging of polyhedral PtPd core–shell nanoparticles by Cs-corrected STEM. J. Phys. Chem. C **116**, 23596 (2012)

111. X. Wang, S.-I. Choi, L.T. Rolling, M. Luo, C. Ma, L. Zhang, M. Chi, J. Liu, Z. Xie, J.A. Herron, M. Mavrikakis, Y. Xia, Palladium–platinum core-shell icosahedra with substantially enhanced activity and durability towards oxygen reduction. Nat. Commun. **6**, 7594 (2015)
112. E.A. Anumol, A. Halder, C. Nethravathi, B. Viswanath, N. Ravishankar, Nanoporous alloy aggregates: Synthesis and electrocatalytic activity. J. Mater. Chem. **21**, 8721 (2011)
113. Y.-C. Hsieh, Y. Zhang, D. Su, V. Volkov, R. Si, L. Wu, Y. Zhu, W. An, P. Ping Liu, P. He, S. Ye, R.R. Adzic, J.X. Wang, Ordered bilayer ruthenium–platinum core-shell nanoparticles as carbon monoxide-tolerant fuel cell catalysts. Nat. Commun. **4**, 2466 (2013)
114. R. He, Y.-C. Wang, X. Wang, Z. Wang, G. Liu, W. Zhou, L. Wen, Q. Li, X. Wang, X. Chen, J. Zeng, J.G. Hou, Facile synthesis of pentacle gold–copper alloy nanocrystals and their plasmonic and catalytic properties. Nat. Commun. **5**, 4327 (2014)
115. B. Goris, L. Polavarapu, S. Bals, G. Van Tendeloo, L.M. Liz-Marzán, Monitoring galvanic replacement through three-dimensional morphological and chemical mapping. Nano Lett. **14**, 3220 (2014)
116. H. Kuroki, T. Tamaki, M. Matsumoto, M. Arao, K. Kubobuchi, H. Imai, T. Yamaguchi, Platinum–iron–nickel trimetallic catalyst with superlattice structure for enhanced oxygen reduction activity and durability. Ind. Eng. Chem. Res. **55**, 11458 (2016)
117. C. Zhang, W. Sandorf, Z. Peng, Octahedral Pt_2CuNi uniform alloy nanoparticle catalyst with high activity and promising stability for oxygen reduction reaction. ACS Catal. **5**, 2296 (2015)
118. B.T. Sneed, A.P. Young, D. Jalalpoor, M.C. Golden, S. Mao, Y. Jiang, Y. Wang, C.-K. Tsung, Shaped Pd–Ni–Pt core-sandwich-shell nanoparticles: Influence of Ni sandwich layers on catalytic electrooxidations. ACS Nano **8**, 7239 (2014)
119. S. Guo, X. Zhang, W. Zhu, K. He, D. Su, A. Mendoza-Garcia, S.F. Ho, G. Lu, S. Sun, Nanocatalyst superior to Pt for oxygen reduction reactions: The case of core/shell Ag(Au)/CuPd nanoparticles. J. Am. Chem. Soc. **136**, 15026 (2014)
120. S. Khanal, N. Bhattarai, D. McMaster, D. Bahena, J.J. Velazquez-Salazar, M. Jose-Yacaman, Highly monodisperse multiple twinned AuCu-Pt trimetallic nanoparticles with high index surfaces. Phys. Chem. Chem. Phys. **16**, 16278 (2014)
121. L. Wang, Y. Yamauchi, Strategic synthesis of trimetallic Au@Pd@Pt core−shell nanoparticles from poly(vinylpyrrolidone)-based aqueous solution toward highly active Electrocatalysts. Chem. Mater. **23**, 2457 (2011)
122. S. Khanal, N. Bhattarai, J.J. Velazquez-Salazar, D. Bahena, G. Soldano, A. Ponce, M.M. Mariscal, S. Mejia-Rosales, M. Jose-Yacaman, Trimetallic nanostructures: The case of AgPd-Pt multiply twinned nanoparticles. Nanoscale **5**, 12456 (2013)
123. Y. Liu, K. Ai, X. Cheng, L. Huo, L. Lu, Gold-nanocluster-based fluorescent sensors for highly sensitive and selective detection of cyanide in water. Adv. Funct. Mater. **20**, 951 (2010)
124. H. Xu, K.S. Suslick, Water-soluble fluorescent silver nanoclusters. Adv. Mater. **22**, 1078 (2010)
125. T.S. van Zanten, A. Cambi, M. Koopman, B. Joosten, C.G. Figdor, M.F. Garcia-Parajo, Hotspots of GPI-anchored proteins and integrin nanoclusters function as nucleation sites for cell adhesion. Proc. Natl. Acad. Sci. U.S.A. **106**, 18557 (2009)
126. G. Li, H. Abroshan, Y. Chen, R. Jin, H.J. Kim, Experimental and mechanistic understanding of aldehyde hydrogenation using Au_{25} nanoclusters with Lewis acids: Unique sites for catalytic reactions. J. Am. Chem. Soc. **137**, 14295 (2015)
127. Ž. Šljivančanin, A. Pasquarello, Supported Fe nanoclusters: Evolution of magnetic properties with cluster size. Phys. Rev. Lett. **90**, 247202 (2003)
128. J.-L. Li, J.-F. Jia, X.-J. Liang, X. Liu, J.-Z. Wang, Q.-K. Xue, Z.-Q. Li, S.T. John, Z. Zhang, S. Zhang, Spontaneous assembly of perfectly ordered identical-size nanocluster arrays. Phys. Rev. Lett. **88**, 066101 (2002)
129. B. Corain, G. Schmid, N. Toshima, *Metal Nanoclusters in Catalysis and Materials Science: The Issue of Size Control* (Elsevier, Neherlands, 2011)
130. J. Wang, G. Wang, J. Zhao, Density-functional study of Au_n (n = 2–2 0) clusters: Lowest-energy structures and electronic properties. Phys. Rev. B **66**, 035418 (2002)

131. H. Grönbeck, W. Andreoni, Gold and platinum microclusters and their anions: Comparison of structural and electronic properties. Chem. Phys. **262**, 1 (2000)
132. N. Durante, A. Fortunelli, M. Broyer, M. Stener, Optical properties of Au nanoclusters from TD-DFT calculations. J. Phys. Chem. C **115**, 6277 (2011)
133. E. Wahlström, N. Lopez, R. Schaub, P. Thostrup, A. Rønnau, C. Africh, E. Lægsgaard, J.K. Nørskov, F. Besenbacher, Bonding of gold nanoclusters to oxygen vacancies on rutile TiO_2 (110). Phys. Rev. Lett. **90**, 026101 (2003)
134. L. de Jongh, *Physics and Chemistry of Metal Cluster Compounds: Model Systems for Small Metal Particles* (Springer, Netherlands, 2013)
135. D.A. Blom, L.F. Allard, S. Mishina, M.A. O'keefe, Early results from an aberration-corrected JEOL 2200FS STEM/TEM at Oak Ridge National Laboratory. Microsc. Microanal. **12**, 483 (2006)
136. Z. Wang, R. Palmer, Direct atomic imaging and dynamical fluctuations of the tetrahedral Au_{20} cluster. Nanoscale **4**, 4947 (2012)
137. Y. Li, J.H.-C. Liu, C.A. Witham, W. Huang, M.A. Marcus, S.C. Fakra, P. Alayoglu, Z. Zhu, C.M. Thompson, A. Arjun, A Pt-cluster-based heterogeneous catalyst for homogeneous catalytic reactions: X-ray absorption spectroscopy and reaction kinetic studies of their activity and stability against leaching. J. Am. Chem. Soc. **133**, 13527 (2011)
138. P.-P. Fang, S. Duan, X.-D. Lin, J.R. Anema, J.-F. Li, O. Buriez, Y. Ding, F.-R. Fan, D.-Y. Wu, B. Ren, Tailoring Au-core Pd-shell Pt-cluster nanoparticles for enhanced electrocatalytic activity. Chem. Sci. **2**, 531 (2011)
139. N. Sakai, T. Tatsuma, One-step synthesis of glutathione-protected metal (Au, Ag, Cu, Pd, and Pt) cluster powders. J. Mater. Chem. A **1**, 5915 (2013)
140. S.I. Sanchez, L.F. Allard, W. Sinkler, S.A. Bradley, Characterization of sub-nanometer Pt cluster formation on γ-$A1_2O_3$ via ex situ reductions using MEMS-based heating technology. Microsc. Microanal. **20**(S3), 1656 (2014)
141. P. Daggolu, A. Joseph, D. Kumar, R. Cursetji, Small Pt cluster size diesel oxidation catalyst for cold start CO oxidation. SAE Technical Paper, 2015-26-0088, 2015
142. W. Qian, R. Hao, J. Zhou, M. Eastman, B.A. Manhat, Q. Sun, A.M. Goforth, J. Jiao, Exfoliated graphene-supported Pt and Pt-based alloys as electrocatalysts for direct methanol fuel cells. Carbon **52**, 595 (2013)
143. R. Wang, J. Liu, P. Liu, X. Bi, X. Yan, W. Wang, X. Ge, M. Chen, Y. Ding, Dispersing Pt atoms onto nanoporous gold for high performance direct formic acid fuel cells. Chem. Sci. **5**, 403 (2014)
144. A. Mayoral, D.A. Blom, M.M. Mariscal, C. Guiterrez-Wing, J. Aspiazu, M. Jose-Yacaman, Gold clusters showing pentagonal atomic arrays revealed by aberration-corrected scanning transmission electron microscopy. Chem. Commun. **46**, 8758 (2010)
145. H. Li, Y. Pei, X.C. Zeng, Two-dimensional to three-dimensional structural transition of gold cluster Au_{10} during soft landing on TiO_2 surface and its effect on CO oxidation. J. Chem. Phys. **133**, 134707 (2010)
146. L.-M. Wang, R. Pal, W. Huang, X.C. Zeng, L.-S. Wang, Observation of earlier two-to-three dimensional structural transition in gold cluster anions by isoelectronic substitution: MAu_n^-(n = 8–11; M = Ag, cu). J. Chem. Phys. **132**, 114306 (2010)
147. M.P. Johansson, I. Warnke, A. Le, F. Furche, At what size do neutral gold clusters turn three-dimensional? J. Phys. Chem. C **118**, 29370 (2014)
148. H. Yang, J. Lei, B. Wu, Y. Wang, M. Zhou, A. Xia, L. Zheng, N. Zheng, Crystal structure of a luminescent thiolated Ag nanocluster with an octahedral Ag_6^{4+} core. Chem. Commun. **49**, 300 (2013)
149. H. Häkkinen, M. Walter, H. Grönbeck, Divide and protect: Capping gold nanoclusters with molecular gold-thiolate rings. The J. Phys. Chem. B **110**, 9927 (2006)
150. L. Li, L. Dou, H. Zhang, Layered double hydroxide supported gold nanoclusters by glutathione-capped Au nanoclusters precursor method for highly efficient aerobic oxidation of alcohols. Nanoscale **6**, 3753 (2014)

151. J. Cai, H. Ma, J. Zhang, Q. Song, Z. Du, Y. Huang, J. Xu, Gold nanoclusters confined in a supercage of Y zeolite for aerobic oxidation of HMF under mild conditions. Chem. Eur. J. **19**, 14215 (2013)
152. L.X. Zhang, J.L. Shi, J. Yu, Z.L. Hua, X.G. Zhao, M.L. Ruan, A new in-situ reduction route for the synthesis of Pt nanoclusters in the channels of mesoporous silica SBA-15. Adv. Mater. **14**, 1510 (2002)
153. T. Zoberbier, T.W. Chamberlain, J. Biskupek, N. Kuganathan, S. Eyhusen, E. Bichoutskaia, U. Kaiser, A.N. Khlobystov, Interactions and reactions of transition metal clusters with the interior of single-walled carbon nanotubes imaged at the atomic scale. J. Am. Chem. Soc. **134**, 3073 (2012)
154. Z.W. Wang, O. Toikkanen, B.M. Quinn, R.E. Palmer, Real-space observation of Prolate monolayer-protected Au_{38} clusters using aberration-corrected scanning transmission electron microscopy. Small **7**, 1542 (2011)
155. N. Wang, Q. Sun, R. Bai, X. Li, G. Guo, J. Yu, In situ confinement of ultra-small Pd clusters within nanosized silicalite-1 zeolite for high-efficient hydrogen generation catalysis. J. Am. Chem. Soc. **138**, 7484 (2016)
156. C. Aydin, J. Lu, M. Shirai, N.D. Browning, B.C. Gates, Ir_6 clusters compartmentalized in the supercages of zeolite NaY: Direct imaging of a catalyst with aberration-corrected scanning transmission electron microscopy. ACS Catal. **1**, 1613 (2011)
157. D. Yang, P. Xu, N.D. Browning, B.C. Gates, Tracking Rh atoms in zeolite HY: First steps of metal cluster formation and influence of metal nuclearity on catalysis of ethylene hydrogenation and ethylene dimerization. J. Phys. Chem. Lett. **7**, 2537 (2016)
158. D.C. Meier, D.W. Goodman, The influence of metal cluster size on adsorption energies: CO adsorbed on au clusters supported on TiO_2. J. Am. Chem. Soc. **126**, 1892 (2004)
159. B. Yoon, H. Häkkinen, U. Landman, A.S. Wörz, J.-M. Antonietti, S. Abbet, K. Judai, U. Heiz, Charging effects on bonding and catalyzed oxidation of CO on Au_8 clusters on MgO. Science **307**, 403 (2005)
160. X. Han, F. Cheng, T. Zhang, J. Yang, Y. Hu, J. Chen, Hydrogenated uniform Pt clusters supported on porous $CaMnO_3$ as a bifunctional electrocatalyst for enhanced oxygen reduction and evolution. Adv. Mater. **26**, 2047 (2014)
161. M. Stamatakis, M.A. Christiansen, D.G. Vlachos, G. Mpourmpakis, Multiscale modeling reveals poisoning mechanisms of MgO-supported au clusters in CO oxidation. Nano Lett. **12**, 3621 (2012)
162. J.H. Kwak, L. Kovarik, J.N. Szanyi, CO_2 reduction on supported Ru/Al_2O_3 catalysts: Cluster size dependence of product selectivity. ACS Catal. **3**, 2449 (2013)
163. S. Bonanni, K. Aït-Mansour, W. Harbich, H. Brune, Reaction-induced cluster ripening and initial size-dependent reaction rates for CO oxidation on Pt_n/TiO_2 (110)-(1× 1). J. Am. Chem. Soc. **136**, 8702 (2014)
164. J. Li, Z. Wang, C. Chen, S. Huang, Atomic-scale observation of migration and coalescence of au nanoclusters on YSZ surface by aberration-corrected STEM. Sci Rep **4**, 5521 (2014)
165. T. Gerber, J. Knudsen, P.J. Feibelman, E. Granas, P. Stratmann, K. Schulte, J.N. Andersen, T. Michely, CO-induced Smoluchowski ripening of Pt cluster arrays on the graphene/Ir (111) Moiré. ACS Nano **7**, 2020 (2013)
166. F. Hasché, T.P. Fellinger, M. Oezaslan, J.P. Paraknowitsch, M. Antonietti, P. Strasser, Mesoporous nitrogen doped carbon supported platinum PEM fuel cell electrocatalyst made from ionic liquids. ChemCatChem **4**, 479 (2012)
167. N.D. Browning, C. Aydin, J. Lu, A. Kulkarni, N.L. Okamoto, V. Ortalan, B.W. Reed, A. Uzun, B.C. Gates, Quantitative Z-contrast imaging of supported metal complexes and clusters—A gateway to understanding catalysis on the atomic scale. ChemCatChem **5**, 2673 (2013)
168. C. Aydin, A. Kulkarni, M. Chi, N.D. Browning, B.C. Gates, Three-dimensional structural analysis of MgO-supported osmium clusters by electron microscopy with single-atom sensitivity. Angew. Chem. Int. Ed. (English) **52**, 5262 (2013)
169. J. Ohyama, A. Esaki, T. Koketsu, Y. Yamamoto, S. Arai, A. Satsuma, Atomic-scale insight into the structural effect of a supported Au catalyst based on a size-distribution analysis using Cs-STEM and morphological image-processing. J. Catal. **335**, 24 (2016)

170. O. Hernández-Cristóbal, J.S. Arenas-Alatorre, G. Díaz, D. Bahena, M.J. Yacamán, High resolution HAADF characterization of Ir/TiO_2 catalyst reduced at 500 °C: Intensity profile analysis. J. Phys. Chem. C **119**, 11672 (2015)
171. O. Miramontes, F. Bonafé, U. Santiago, E. Larios-Rodriguez, J.J. Velázquez-Salazar, M.M. Mariscal, M.J. Yacaman, Ultra-small rhenium clusters supported on graphene. Phys. Chem. Chem. Phys. **17**, 7898 (2015)
172. T. Imaoka, H. Kitazawa, W.J. Chun, K. Yamamoto, Finding the most catalytically active platinum clusters with low atomicity. Angew. Chem. Int. Ed. (English) **54**, 9810 (2015)
173. Y. Wang, X.-K. Wan, L. Ren, H. Su, G. Li, S. Malola, S. Lin, Z. Tang, H. Häkkinen, B.K. Teo, Atomically precise Alkynyl-protected metal nanoclusters as a model catalyst: Observation of promoting effect of surface ligands on catalysis by metal nanoparticles. J. Am. Chem. Soc. **138**, 3278 (2016)
174. J. Yan, H. Su, H. Yang, C. Hu, S. Malola, S. Lin, B.K. Teo, H. Häkkinen, N. Zheng, Asymmetric synthesis of chiral bimetallic $[Ag_{28}Cu_{12}(SR)_{24}]^{4-}$Nanoclusters via ion pairing. J. Am. Chem. Soc. **138**, 12751 (2016)
175. V. Ortalan, A. Uzun, B.C. Gates, N.D. Browning, Towards full-structure determination of bimetallic nanoparticles with an aberration-corrected electron microscope. Nat. Nanotechnol. **5**, 843 (2010)
176. P.J. Ferreira, K. Mitsuishi, E.A. Stach, In situ transmission electron microscopy. MRS Bull. **33**, 83 (2008)
177. M.A. Asoro, D. Kovar, Y. Shao-Horn, L.F. Allard, P.J. Ferreira, Coalescence and sintering of Pt nanoparticles: In situ observation by aberration-corrected HAADF STEM. Nanotechnology **21**, 025701 (2010)
178. E.A. Anumol, C. Nethravathi, N. Ravishankar, Mechanistic insights into a non-classical diffusion pathway for the formation of hollow Intermetallics: A route to multicomponent hollow structures. Part. Part. Syst. Charact. **30**, 590 (2013)
179. E.A. Lewis, T.J.A. Slater, E. Prestat, A. Macedo, P. O'Brien, P.H.C. Camargo, S.J. Haigh, Real-time imaging and elemental mapping of AgAu nanoparticle transformations. Nanoscale **6**, 13598 (2014)
180. N. de Jonge, F.M. Ross, Electron microscopy of specimens in liquid. Nat. Nanotechnol. **6**, 695 (2011)
181. X. Chen, C. Li, H. Cao, Recent developments of the in situ wet cell technology for transmission electron microscopies. Nanoscale **7**, 4811 (2015)
182. J.M. Yuk, J. Park, P. Ercius, K. Kim, D.J. Hellebusch, M.F. Crommie, J.Y. Lee, A. Zettl, A.P. Alivisatos, High-resolution EM of colloidal nanocrystal growth using graphene liquid cells. Science **336**, 61 (2012)
183. T.W. Hansen, J.B. Wagner, P.L. Hansen, S. Dahl, H. Topsøe, C.J.H. Jacobsen, Atomic-resolution in situ transmission electron microscopy of a promoter of a heterogeneous catalyst. Science **294**, 1508 (2001)
184. S. Zhang, P.N. Plessow, J.J. Willis, S. Dai, M. Xu, G.W. Graham, M. Cargnello, F. Abild-Pedersen, X. Pan, Dynamical observation and detailed description of catalysts under strong metal–support interaction. Nano Lett. **16**, 4528 (2016)
185. S. Zhang, C. Chen, M. Cargnello, P. Fornasiero, R.J. Gorte, G.W. Graham, X. Pan, Dynamic structural evolution of supported palladium–ceria core–shell catalysts revealed by in situ electron microscopy. Nat. Commun. **6**, 7778 (2015)
186. J.R. Jinschek, Advances in the environmental transmission electron microscope (ETEM) for nanoscale in situ studies of gas-solid interactions. Chem. Commun. **50**, 2696 (2014)
187. Y. Kuwauchi, S. Takeda, H. Yoshida, K. Sun, M. Haruta, H. Kohno, Stepwise displacement of catalytically active gold nanoparticles on cerium oxide. Nano Lett. **13**, 3073 (2013)
188. S. Takeda, Y. Kuwauchi, H. Yoshida, Environmental transmission electron microscopy for catalyst materials using a spherical aberration corrector. Ultramicroscopy **151**, 178 (2015)
189. E.D. Boyes, P.L. Gai, Visualizing reacting single atoms in chemical reactions: Advancing the frontiers of materials research. MRS Bull. **40**, 600 (2015)

190. Y. Li, D. Zakharov, S. Zhao, R. Tappero, U. Jung, A. Elsen, P. Baumann, R.G. Nuzzo, E.A. Stach, A.I. Frenkel, Complex structural dynamics of nanocatalysts revealed in operando conditions by correlated imaging and spectroscopy probes. Nat. Commun. **6**, 7583 (2015)
191. T.E. Martin, P.L. Gai, E.D. Boyes, Dynamic imaging of Ostwald ripening by environmental scanning transmission electron microscopy. ChemCatChem **7**, 3705 (2015)